Developing Integrated Optofluidic Platforms for Cellular Phenotyping

by

Nien-Tsu Huang

A dissertation submitted in partial fulfillment
of the requirements for the degree of
Doctor of Philosophy
(Mechanical Engineering)
in the University of Michigan
2013

Doctoral Committee:

Professor Katsuo Kurabayashi, Chair
Assistant Professor Jianping Fu
Assistant Professor Allen Liu
Professor Shuichi Takayama

To my family,

Table of Contents

List of Figures

List of Tables

List of Appendices

Abstract

This research demonstrates two optofluidic platforms to address three major problems of current fluorescence-based optical detection methods for cellular phenotyping: (1) limited number of fluorescent probes, (2) laborious and time-consuming assay preparation and manipulation steps, and (3) compromised sensing performance in a point-of-care setting. The first optofluidic platform is called the "microfluidic multispectral flow cytometry (MMFC) device". The function of the MMFC device is to discriminate multiple cell types based on their fluorescent proteins or surface biomarkers at single cell level with a simplified optical setup. It represents a unique class of optofluidic system incorporating a MEMS-based tunable nanoimprinted grating microdevice, a single excitation laser, and a single PMT detector. The system enables us to achieve *in-situ* continuous spectral profile detection for bioparticles flowing in a microfluidic channel with high specificity and high speed. The second optofluidic platform is called the "microfluidic immunophenotyping assay (MIPA) device". The function of the MIPA device is to achieve on-chip cell trapping, cell stimulation and *in-situ* secreted cytokine detection in one single chip with a shorten assay time and less sample requirements. Compared to previous studies using heterogeneous immunoassay techniques and requiring a longer assay time due to multiple surface immobilization processes and washing steps, our immunophenotyping assay with the MIPA device holds significant promise to open ways for rapid immune status determination in real clinical settings.

Chapter 1

Introduction

1.1 Research Background

A large number of processes, functions, and traits at the cell level serve as important indicators of diseases. For example, a cell under a diseased condition experiences alterations and shows heterogeneity in its gene expression [1, 2], drug resistance [3, 4], protein/metabolite production [5-7], proliferation [8], and optical properties [9, 10]. The terminology of "cellular phenotyping" refers to a scientific process to quantify these disease indicators and other phenotypes affected by the genetic information and environment of a cell. In cellular phenotyping, *individual* cells are isolated from tissue and treated as models for complex human biology. This approach offers a practical alternative to the use of human patients in studying the genetic and long-term environmental influences on the human body (Figure 1-1). Current studies reveal that knowledge of the gene alone does not provide any direct insight into downstream biological effects [11, 12]. The question of how genetic factors, coupled with variability in environmental effects (for example, smoking, diet, and atmospheric quality), will affect our bodies and determine the fate of our health still remains unanswered. Establishing links between genetic variants and environmental factors in biological

processes is crucial to overcome these challenges and establish personalized medicine [2]. Cellular phenotyping is the key to reveal such links as well.

Optical technologies are powerful tools to measure spatial and temporal variations of cellular phenotypes in a non-destructive manner with high sensitivity and high throughput. Optofluidics, a rapidly emerging research field, has successfully demonstrated the synergetic integration of optical systems with microfluidics [13-16]. Full monolithic integration of miniature optical and fluidic components together on a common microfluidic platform ultimately offers significant advantages, including (a) enhanced sensing performance coupled with increased precision control and fluidic manipulation of cells, (b) portability and usability (and disposability in some cases) that permit point-of-care (POC) operations under limited resources without large and expensive instruments and specifically trained operators, and (c) instrumentation cost savings that lead to reduced barriers against wider use. Rapid, low-cost optofluidic detection of abnormalities in particular cellular phenotypes may open ways for effectively screening and preventing cancer, human immunodeficiency virus (HIV) infection, and other deadly diseases. As the notable shift in emphasis occurs from solely genotype-focused studies to genotype-phenotype relationship investigations in current life sciences research, it is important to examine the relevance of optofluidics to cellular phenotyping.

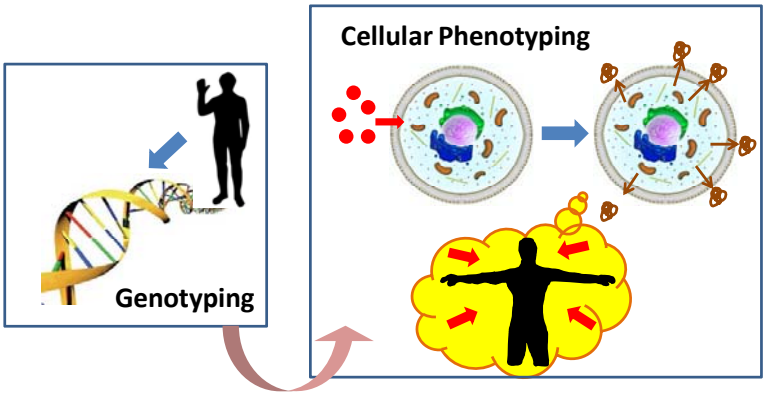

Figure 1-1 Concept of genotyping and cellular phenotyping related to human health care. Genotyping determines the genetic program of human body that potentially triggers the onset of diseases. Cellular phenotyping provides important insights into the influence of both genetic programming and environment on human body and disease development by using an individual cell as a human biology model. Reprinted from [17] with permission from Royal Society of Chemistry.

1.2 Definition of Cellular Phenotype

Cellular phenotypes are generally divided into three categories: (1) nuclear-based phenotypes, (2) cytoplasmic phenotypes, and (3) functional phenotypes. Nuclear-level phenotypes include levels of gene expression, epigenetic modifications and protein binding to DNA and/or chromatin [12]. Cytoplasmic phenotypes are quantities of molecules (e.g., protein) that stem from genetic codes or certain metabolites or by-products that result from cell signaling or biochemical cascades [12]. Functional phenotypes are defined with respect to cellular behavior in growth and proliferation and cellular immune response (e.g. cytokine secretion) or resistance to external stimulants, such as drugs and cytotoxic chemical substances. It should be noted that this categorization is not necessarily distinct as these phenotypes are often related with each other.

1.3 Optical Detection for Cellular Phenotyping

In recent years, there are several optofluidic technologies specifically targeted on cellular phenotyping, including Surface Plasmon Resonance (SPR), Surface Enhanced Raman Scattering (SERS), interferometry and fluorescence detection. Among these optical detection schemes, the most common used method is fluorescence detection. Fluorescence is the photoemission phenomenon of specific molecules when they absorb photons or other electromagnetic energy [18, 19]. These molecules, usually called fluorophore or fluorescent dye, are used as indicators for particular bio-molecule visualization, environmental condition monitoring or cellular stimulation study. Fluorescence detection is the widely employed for chemical or biological analysis. The technique benefits from well-established, highly sensitive, selective fluorescent labeling biomarkers and has ready access to a wide spectrum of commercially available fluorescent instruments, such as optical microscopes, multi-well plate readers, and flow cytometers. The general fluorescent-based detection system usually consists of excitation light sources, such as lasers, light-emitting diodes (LEDs) or mercury lamps, sample holders, such as glass slides, multiwall plates or cuvettes, where a fluorescence-emitting process takes place, and detectors, such as charge-coupled devices (CCDs), photomultiplier tubes (PMTs), or spectrometers, to collect the emission signal and translate it into a microscopic image or electrical output.

One problem of using fluorescence detection method is the autofluorescence of plastic materials (e.g. PDMS, PMMA, and polycarbonate) [20] or biomolecules, which gives rise to background noises and reduces the signal-to-noise ratio. Therefore, it is important to carefully select appropriate device materials and purified sample. Besides,

typical fluorescent probes have fairly a broad emission spectrum with full width at half maximum (FWHM) =50~100nm, which limits the total number of parameters reported with a fixed detection wavelength bandwidth. Moreover, the fluorescent labeling method usually requires complicated reagent manipulation processes (e.g., vortex, centrifuge and filter) and a prolonged incubation time, which may affect the phenotype of target cells. Finally, the photo-bleaching effect of fluorescent probe makes long term cell-based assay monitoring difficult.

There are many commercially available fluorescent probes specifically for cellular phenotyping detection. For example, fluorescent protein, such as green fluorescent protein (GFP), has been widely used as a probe to visualize, track and quantify protein translocation or its amount in living cells [21]. Other fluorescent probes target intracellular messengers of signal transduction, such as calcium ion (Ca^{2+}), pH, Oxygen and CO_2. The change of these parameters allow researchers to understand how cells regulate different biological processes, including gene expression, metabolism, and apoptosis [22]. Another cellular phenotype that current fluorescent probes report on is cell immunity. It evaluates the condition of immune cells in response to outside invasion, such as bacteria or virus. The immunofluorescence (IF) labeling technique has been widely used for monitoring the cellular immune status. Typically, the IF labeling technique can detect endogenous expression proteins or other antigens with targeted fluorescent antibodies. For cell immunity application, people utilize the specificity of fluorescent-labeled antibodies to target cells secreting a specific antigen or protein and then quantify the antigen secretion by monitoring the fluorescent image of antibodies under a wide-field microscope. Flow cytometry and enzyme-linked immunosorbent spot

(ELISpot) assay are the two most common technologies for single immune cell analysis [23, 24]. However, complicated sample preparation step and long process time limit their utility in emergent clinical diagnosis.

Fluorescence-based cellular phenotyping detection benefits from microfluidics that provides sample-efficient, high-throughput, and precise cellular environment control [25, 26]. The optofluidic approach of merging optics with microfluidic further provides unique advantages that off-chip optics cannot accomplish. This approach provides better optical focusing, easier optical alignments, higher multiplexity and multiple functionalities for chemical or biological analysis by integrating optical components into fluidics. For example, Balslev et al. [27] developed a monolithic hybrid optofluidic system to achieve on-chip sample mixing and detection. Tung et al. [28] embedded four optical fibers into microfluidic flow cytometry to achieve simultaneous two-color excitation/emission detection. Seo and Lee [29] developed a compound 2D microlens for focusing LED excitation light onto a microchannel region. Other groups integrated a light source [30] and a chip-size wavelength detector [31] towards realizing all-in-one system integration. The optofluidic integration enables development of a miniaturized and easy-to-use optofluidic platform for POC diagnosis. Such a system permits simplified optical alignment with cost-efficient and minimum optical components. However, a POC optofluidic system usually shows compromised sensing performance as compared to a highly sophisticated off-chip fluorescence microscopy system.

1.4 Motivation for Research

Based on above discussion, we summarize three major problems of current fluorescence-based optical detection methods for cellular phenotyping: (1) limited number of fluorescent probes, (2) laborious and time-consuming assay preparation and manipulation steps, and (3) compromised sensing performance in a POC setting. The motivation of this research is trying to address these limitations. In this thesis, I developed two optofluidic platforms for cellular phenotyping. The first optofluidic platform is called the "microfluidic multispectral flow cytometry (MMFC) device". The function of the MMFC device is to discriminate multiple cell types based on their fluorescent proteins or surface biomarkers at single cell level with a simplified optical setup. Another optofluidic platform is called the "microfluidic immunophenotyping assay (MIPA) device". The function of the MIPA device is to achieve on-chip cell trapping, cell stimulation and *in-situ* secreted cytokine detection in one single chip with a shorten assay time and less sample requirements. The detailed research motivation of each platform is described in the following sections.

1.4.1 Microfluidic Multispectral Flow Cytometry (MMFC)

Due to recent advancements in fluorescent probe technology, fluorescently color-coded cells, biomolecules, and microspheres have been widely used for multi-parameter detection in disease screening [32], molecular imaging [33], DNA sequencing [34], microarray applications [35, 36], cellular function studies [37], and multiplexed bead-based assays [38]. The ability to identify multiple fluorescence emissions with high

specificity is needed to gain sufficient multiplicity in biological analytical methods. Color decoding achieved by analyzing the detailed spectral characteristics of fluorophores can meet this demand, allowing fluorescence emissions with significant spectral overlap to be distinguished [39-41]. However, detection of multiple spectral signatures generally reduces measurement speed and throughput due to a larger volume of required information and suffers from the added complexity and cost of optics as compared to techniques based on intensity measurements with discrete spectral bands. For example, current state-of-art flow cytometers using as many as 11 fluorescent probe colors have been demonstrated to elucidate complex immune systems [42], but these instruments usually require a large number of filters and detectors and only permit discrete ($\Delta\lambda$ = 40-90 nm) spectral measurement, thus prohibiting color discrimination of fluorescent probes with only slight differences in wavelength characteristics. To address this issue, our group recently develop a highly sensitive dynamic spectroscopy technique, which enables *in-situ* detection of optical emission spectra by incorporating a high-speed strain tunable nanoimprinted grating microdevice [43]. With this technique, we demonstrated the ability to track the optical spectrum of time-varying multi-wavelength signals with 500 μs time resolution, 5nm spectral resolution, and sensitivity for pW optical powers [44]. By extension of our previous study, I propose to integrate this high-speed photospectral detection technique into a microfluidic flow cytometry setting, which aims to enable the flow cytometry instrument to carry out high-speed *continuous* multispectral detection with significantly higher spectral resolution using a smaller, technically simpler optical design with a vastly reduced number of components.

1.4.2 Microfluidic Immunophenotyping Assay (MIPA) Device

Cell-stimulation assays have provided critical means for determining functional immune responsiveness to a variety of stimuli in multiple clinical settings in order to provide diagnostic [24, 45], prognostic [46-53], and therapeutic insight [54, 55] across a broad spectrum of patient cohorts. These assays involve stimulating white blood cells, either isolated or within whole blood, and quantitatively examining the amount of cell-secreted cytokines (*i.e.*, cell-signaling protein molecules). At present, enzyme-linked immunosorbent assay/spot (ELISA/ELISpot) [56, 57] and intracellular cytokine staining (ICCS) assay are the most accepted methods to quantify cellular cytokine production while enabling multiplex, high-sensitivity (~1 pg/mL) analyses [23, 24]. However, these techniques usually require numerous reagent manipulation processes that involve multiple staining, washing and blocking steps, prohibiting their utility in real-time clinical decision making. Further, during these multiple sample processing steps, unpredictable signal variation and unintended analyte dilution are often induced, resulting in a narrow dynamic range, low screen throughput and compromised reproducibility. Even though ELISA is most commonly used for immunophenotyping analyses in a clinical setting, the ELISA-based approach usually needs to transfer cell-secreted cytokine samples from culture petri dishes or centrifuge tubes to multi-well plates for signal reading in a plate reader. These steps can prove challenging, largely because edge effects and uncontrolled evaporation from very small wells can result in poor assay conditions [58]. To overcome these limitations, I propose to develop a microfluidic immunophenotyping assay (MIPA) device with well-confined and miniaturized microenvironment to significantly reduce sample volume and assay time. Moreover, the

proposed device using a no-wash, homogeneous bead-based sandwich immunoassay can eliminate a need for complex instrumental operations, prolonged sample pretreatments, and protein surface immobilizations, which are required by other microfluidic approaches reported in previous studies [25, 59-61].

1.5 Thesis Objectives

Motivated by addressing shortcomings of existing cellular phenotyping assay, this thesis research has two main goals achieved by developing new optofluidic platforms. The first goal is to provide a new approach to multispectral detection enabling high-speed and continuous spectrum measurement for multianalyte studies. We integrate a dynamic *in-situ* spectroscopy unit into a microfluidic flow cytometry setting and build an optical setup for high-speed signal acquisition. Using a continuous spectrum profile, we can obtain more characteristic parameters of the spectral signature of the signal to discriminate multiple cell types. The second goal is to efficiently trap targeted cells and simplify following cellular immunophenotyping assay protocols. Our microfluidic immunophenotyping assay device allows uniform and efficient cell seeding in an on-chip reaction chamber. Once cells are trapped, the platform can simultaneously count the total number of viable cells among those seeded and preserved the viability of these cells for downstream live-cell culture and analysis. This platform is aimed to allow a rapid, convenient, and reagent-saving immunophenotyping assay protocol to measure cytokine secreted from endotoxin-stimulated cells. The prompt testing results will help physicians evaluate patients' immune status, which can be used for developing clinical strategies or drug treatments.

1.6 Thesis Outline

Based on above research objectives, the thesis is comprises four subsequent chapters. The outline is summarized as follows:

Chapter II - Review of Related Studies: This chapter reviews other research related to this project. The review is divided into two parts (1) microfluidic flow cytometry and (2) microfluidic cell capture and analysis device. I briefly introduce current optofluidic devices for cellular phenotyping. The advantages and their limitations are also discussed.

Chapter III - Microfluidic Multispectral Flow Cytometry: In this chapter, we report a high-speed photospectral detection technique integrated with microfluidic flow cytometry setting. It is capable of discriminating subtle variations of spectral signature among fluorescently labeled cells and microspheres flowing in a microfluidic channel. The platform shows high-resolution fluorescent spectral signatures detection based on single-laser excitation and single-detector spectroscopy. It can expand specificity of multicolor flow cytometry with enhancing detection capabilities.

Chapter IV - Microfluidic Immunophenotyping Assay Device: In this chapter, we report a highly integrated microfluidic platform incorporating a no-wash bead-based chemiluminescence immunodetection assay. The microfluidic device allowed us to seed, stimulate cells and monitor their immune response under a well-controlled microenvironment with less sample volume and shorter assay time. Our strategy of monitoring immune cell functions *in situ* using a microfluidic platform could impact future medical treatments of acute infectious diseases and immune disorders by enabling a rapid, sample-efficient cellular immunophenotyping analysis.

Chapter V - Conclusions and Future Works: The final chapter summarizes the impact of the present research and discusses future research directions. The future work of microfluidic multispectral flow cytometry includes integrating the optical components for point-for-care diagnosis, or (2) integrating the nanoimprinted grating to confocal microendoscopy for in-vivo multispectral imaging. For microfluidic immunophenotyping assay device, the future work includes (1) designing the PDMS microfilter membrane to isolate subpopulation of immune cells and monitor their immunophenotyping, and (2) designing the microvalve-controlled microfluidic device for multiplex cytokine detection.

Chapter 2

Review of Related Studies

In this chapter, we will review previous studies related to this thesis research. The studies give insight into the motivations and applications of our research as well as review competing technologies. This chapter is composed of two sections: (1) microfluidic flow cytometry, and (2) microfluidic cell capture and analysis, both for cellular phenotyping. After reviewing these studies, I will summarize limitations of existing microfluidic platforms and describe how to address these problems based on my thesis work.

2.1 Microfluidic Flow Cytometry

We find many studies that focus on developing microfluidic flow cytometers in a simplified, cost-effective, and disposable chip platform for fluorescence detection-based point-of-care (POC) cellular analysis. Frankowski et al. [62] demonstrated a microfluidic flow cytometer to achieve immunological differentiation of leukocyte subpopulations (e.g., lymphocyte, monocyte, and granulocyte) using fluorescently-labeled CD3, CD4, CD14, and C45 surface biomarkers (Figure 2-1). With its carefully designed microfluidic structure, the device permitted two-dimensional sample focusing by only one sheath

flow. In this device, an optical fiber embedded in proximity to a microfluidic channel enabled high-sensitivity detection. The device can potentially be used for immune cell counting for HIV or other disease diagnosis with small sample volume. However, the entire system still required multiple off-chip emission filters, dichoric mirrors, and PMTs to achieve multi-color fluorescence detection. As a result, the whole system remained bulky and its operation would still require tedious manual optical alignment at high precision as the conventional flow cytometry operation does.

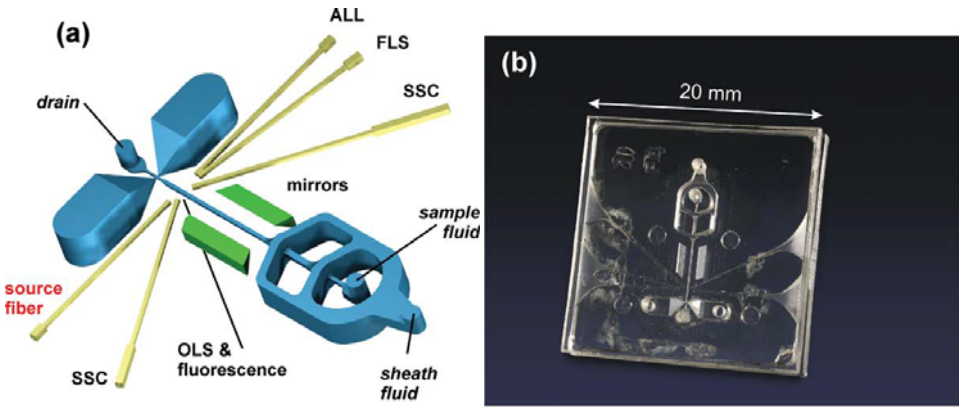

Figure 2-1 (a) Layout of the microfluidic prototype chip with cascaded hydrodynamic focusing. Grooves to insert optical fibers are indicated in yellow and integrated mirrors in green color (b) Photograph of the micro-device shown above. Reprinted from [62] with permission from John Wiley and Sons.

The great ability to manipulate individual cells has been achieved with integrated optics for optofluidic fluorescence detection. For example, Werner et al. [63] demonstrated a microfluidic flow cytometer array integrated with microlens-focused optical tweezers to trap and sort over 200 yeast cells (Figure 2-2). The researchers used this system to investigate a variation in the intercellular pH values of cells exposed to extracellular glucose, which indicate their physiological regulation level. The drawback

of this technique was the spatial non-uniformity of the optical force from cell to cell. This adversely affected the measurement accuracy and throughput.

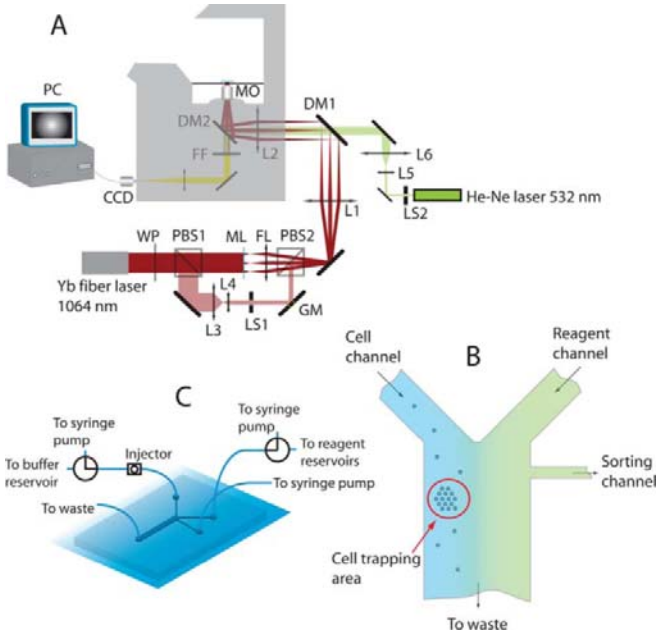

Figure 2-2 Schematic description of (a) the optical setup, (b) the microfluidic chip, and (c) the fluidic circuit. Reprinted from [63] with permission from Royal Society of Chemistry.

Wang et al. [64] used a two-layer microfluidic structure to achieve on-chip single cell fixation for total internal reflection fluorescent (TIRF) measurement (Figure 2-3). In this device, an integrated pneumatic microactuator repeatedly trapped flowing individual cells and fixed them against a channel wall surface emitting the evanescent field. The evanescent excitation locally excited the fluorescent dye of the cell within ~ 100 nm from the substrate surface. The technique probed the cell's protein translocation, which is an important cellular phenotype indicating the therapeutic outcome of cancer and other diseases [65, 66]. The coupling of TIRF with flow cytometry is uniquely enabled by the optofluidic approach. This could be further extended to achieve a rapid and precise observation of the protein translocation of a single cell.

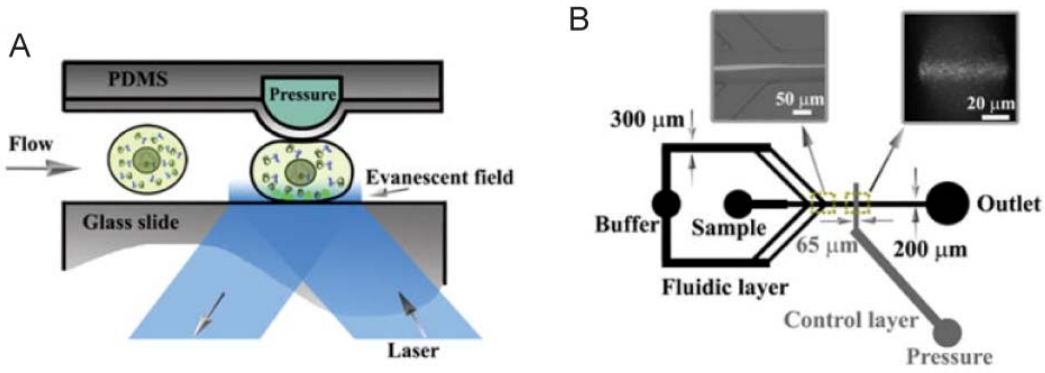

Figure 2-3 (a) Schematic of microfluidic TIRF-FC device integrating an elastomeric valve that forces flowing cells into the evanescent field near the surface of the microfluidic glass channel wall. (b) Top view showing the hydrohynamic focusing and TIRF fluorescence image of cells. Reprinted from [67] with permission from Royal Society of Chemistry.

Significant advances in POC optofluidic cytometry can be found in recent literature. Rosenauer et al. [68] used an adjustable fluidic lens with three dimensional focusing to count the viability of methylene blue-stained yeast cells. Kiesel et al. [69] demonstrated a microfluidic flow cytometer monolithically integrating a photodetector chip, a filter, and a spatially patterned mask (Figure 2-4). The mask modulates the fluorescent emission propagating toward the detector. The resulting time-domain modulation of the detector signal provides information on both the emission intensity and flow speed of single-profile cells. The researchers showed that the two measured parameters and their combination serve as indicators of the sizes of the detected cells. The technique quantitatively obtained the counts of human CD4+ lymphocyte and CD4+ monocyte cells by detecting the fluorescent intensity from labeled CD4 surface biomarkers. They also used a flow speed-intensity mapping plot to new cell-type identification modality for POC flow cytometric measurement.

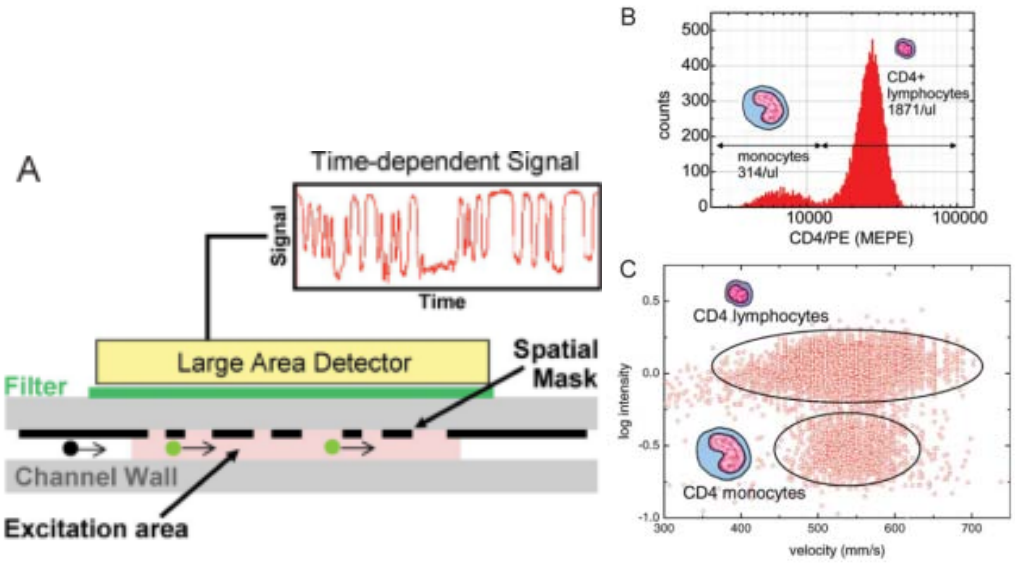

Figure 2-4 (a) Schematic cross-sectional diagram of fluidic channel illustrating the concept of spatially modulated emission. Correlation techniques are applied to determine the position of the particle in real time. (b) Histograms of detected CD4 cells as a function of fluorescent intensity. This illustrates a CD4 count in whole blood. (c) Fluorescence intensity as a function of speed for CD4 cells. Compared to the CD4 lymphocytes, the larger CD4 monocytes show a narrower speed distribution as the flow focusing constrains them to a narrower range in the flow profile. Reprinted from [69] with permission from John Wiley and Sons.

There are more optics-fluid integration examples for POC cytometry. Schelb et al. [70] monolithically integrated a polymer waveguide with a microfluidic channel to excite flowing cells only located on the tip of the waveguide by the evanescent field. The demonstrated ease on handling of waveguide-cell alignment in the microfluidic channel may open a way for advancing the POC technology. Zhu et al. [71] demonstrated a very unique approach to monolithically integrated optofluidic micro-cytometry by developing a cell-phone based fluorescent imaging micro-cytometer (Figure 2-5). They assembled two LED light sources, a lens, and a plastic color filter all together on a cell phone CMOS camera. With the cost-efficient components that require minimum optical alignment, they successfully achieved counting of SYTO16 nucleic-stained white blood cells with a good correlation to commercial hematology analyzer.

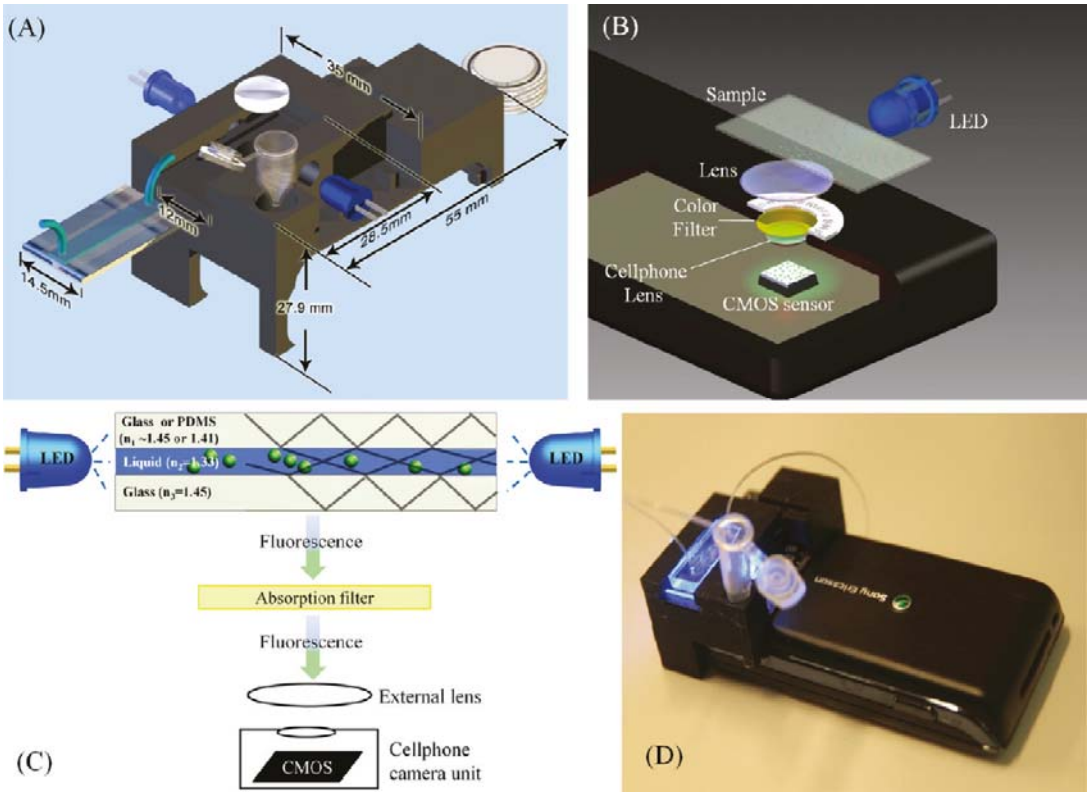

Figure 2-5 (a-c) Various schematic diagrams of the designed optical attachment for optofluidic fluorescent imaging cytometry on a cell phone are illustrated. This lightweight attachment has dimensions of 35 x 55 x 27.9 mm^3. (d) The picture of our optofluidic fluorescent imaging cytometer on a cell phone. Reprinted from [71] with permission from American Chemical Society Publication.

Table 1 lists the type of optical components integrating into a microfluidic platform and summarizes what cellular phenotyping measurements were facilitated by existing microfluidic flow cytometry platforms facilitated.

Table 1 Summary of existing microfluidic flow cytometry devices for cellular phenotyping

Integrated on-chip optical components	Cell type	Phenotype	Clinical/biological relevance	Specificity*	Reference
Embedded fiber, mirror	Leukocytes	Surface biomarkers	HIV	High	Frankowski et al. [62]
Microlens, optical tweezers	Yeast cells	Intracellular pH	Metabolism and cell growth	Medium	Werner et al. [63]
Off-chip optics only	B lymphocytes	Protein translocation	Cancer treatment	N/A	Wang et al. [64]
Focusing lens	Yeast cells	Cellular viability	Cell counting	N/A	Rosenauer et al. [68]
Emission filter	CD4 lymphocytes/ CD4 monocytes	Surface biomarker/ cell size	HIV	Medium	Kiesel et al. [69]
Waveguide	L929 mouse fibroblasts	Cellular morphology	Cell counting/binding kinetic	N/A	Schelb et al. [70]
Light source, focusing lens, filter, camera	White blood cells	Surface biomarker	HIV	High	Zhu et al. [71]

(*Note: "High" – measurement yielding p-value < 0.01 for two cell populations of different phenotypes; "Medium" – measurement permitting qualitative cellular phenotype differentiation from data mapping; "N/A" – no statistical data or histograms available.)

2.2 Microfluidic Cell Capture and Analysis

Microfluidic device provide well-confined microenvironments for spatial and temporal cell growth/response control. The integrated fluidic and optical components can also perform a high-throughput, multiplexed and sample-efficient assay detection. Dimov et al. [25] presented an integrated microfluidic array plate (iMAP) that allows access to gene expression, protein immunoassay, and cytotoxicity information in parallel (Figure 2-6). The device enables cell capturing, drug stimulation, real-time cell imaging. The key feature of iMAP is the interface of the on-board gravity driven flow without any external pressure source. The problem of this device is the limited space for cell growth. Besides, the device is hard to precisely control total cell seeding numbers, which might increase the measurement variability.

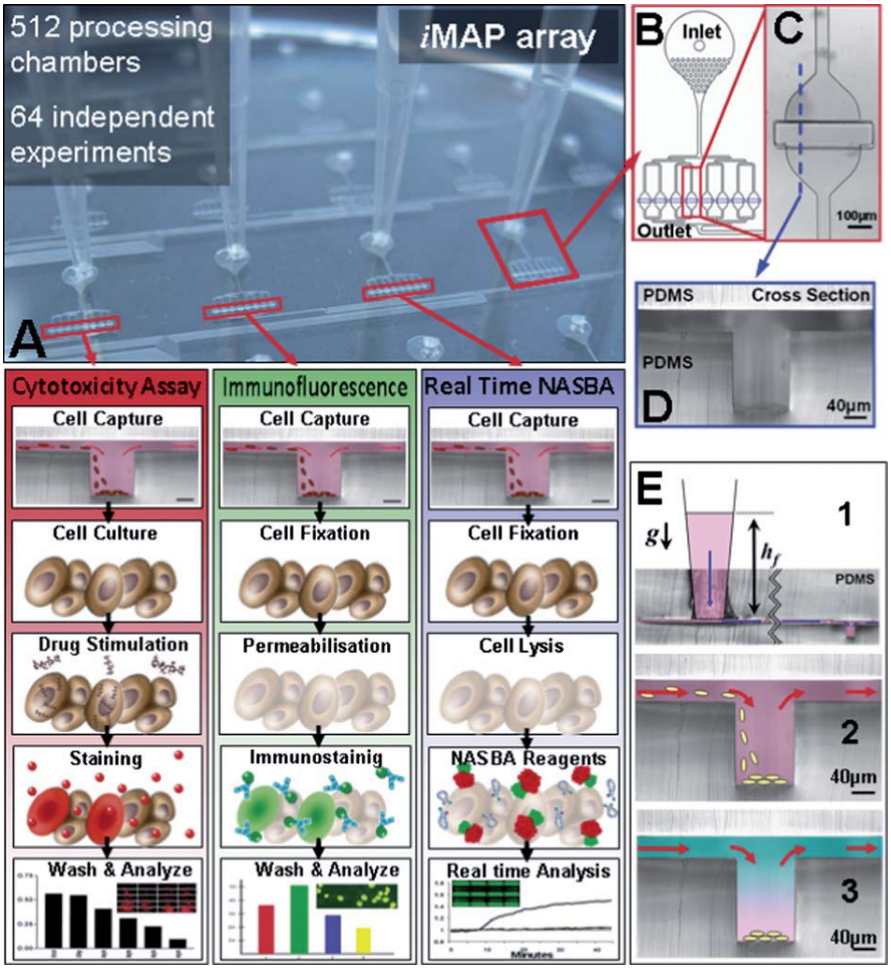

Figure 2-6 iMAP array (a) consists of 64 processing modules (b) that can perform 64 independent simultaneous integrated assays. For statistical replication purposes each module consists of 8 parallel and equally distributed (c) processing chambers that contain a central trench structure (d). Each processing chamber can execute any sequence laboratory unit operations (e), gravity driven flow (e1), cell capture (e2) and reagent loading and mixing (e3). Reprinted from [25] with permission from Royal Society of Chemistry.

Love et al. [60] developed a microengraving method to monitor cell-secreted cytokine at single-cell level (Figure 2-7). They use soft-lithography method to fabricate microwell array. The size of each microwell is 50-100µm in diameter. It confines one to three cells in a small volume (~0.1-1nL). After trapping the cells, the microwell array is flip to the polydimethylsiloxane (PDMS) microarray of immobilized antigens or secondary antibodies to capture the primary antibodies secreted from cells. Compared to ELISA,

the microengraving method can provide a high throughput and multiplexed cellular analysis at single-cell level. However, protein surface immobilization, multiple washing and blocking steps are still required, which makes total assay process quite laborious and time-consuming.

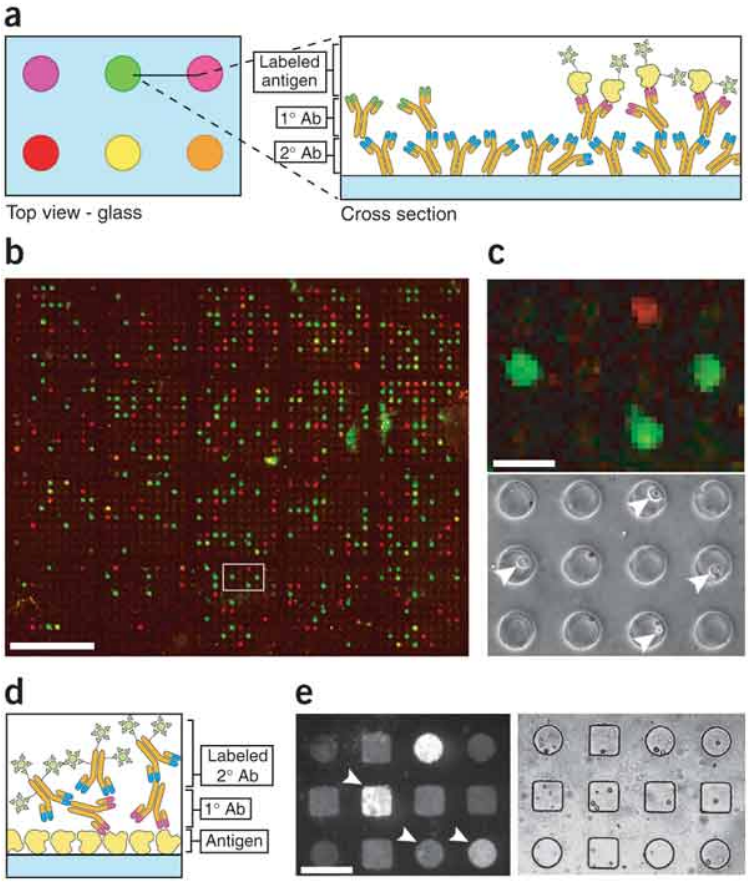

Figure 2-7 Microengraving method for single cell capture. (a) Secondary antibody captures secreted antibody that can then bind labeled antigen. (b-c) Micrograph of a microarray prepared using microwells (50-μm diameter) loaded with a 1:1 mixture of Hyb 099-01 and Y3 cells. (c) Expanded view of the region marked with a white box in (b). The arrowheads indicate the location of cells in the wells. Scale bar, 100 μm. (d) Antigen-coated slides capture secreted antibody that is detected with labeled secondary antibody. (e) Fluorescence micrograph of an array of antibodies (anti-ovalbumin) captured and labeled with goat-anti-mouse Alexa 488 antibodies and the phase contrast image of the corresponding microwells. Reprinted from [60] with permission from Nature Publishing Group.

Zhu et al. [61] developed a microarray with printed poly(ethylene glycol) (PEG) hydrogel spots on glass slide. As shown in Figure 2-8, each spot either coated with anti-CD4 or CD8 antibodies to trap T-cell or various cytokine specific antibodies for cell-

secreted cytokine detection. By using this device, they successfully measure CD4 T-cells secreted IL-2 and IFN-γ cytokine. However, the detection limit is only in ng/mL scale, which may not be sensitive to detect cytokine secreted from small cell number in a short period of time.

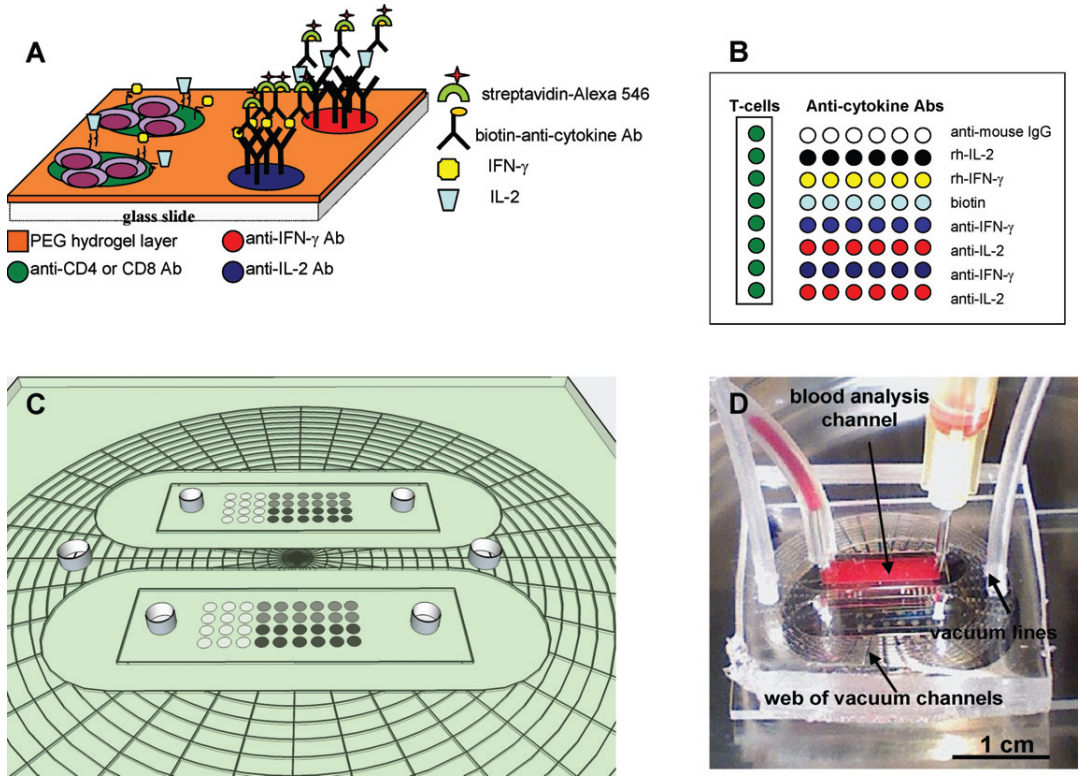

Figure 2-8 (a-b) The conceptual design of microarrays for detection of T-cell-secreted cytokines. (c) Design of a microfluidic platform employed for integration with Ab microarrays. (d) An image of a PDMS microdevice employed for T-cell capture and cytokine detection experiments with one reaction chamber filled with unlysed whole blood. Reprinted from [61] with permission from Royal Society of Chemistry.

A multiplexed cellular phenotyping assay done by Ma et al. [59] showed impressive throughput resulting from the use of a highly integrated microfluidic circuit. They constructed a two-layer PDMS microfluidic network consisting of 1040 nL-microchambers for single cell confinement, each having a top layer with integrated vertical valves and a bottom layer with a microchannel (Figure 2-9). Primary antibodies were immobilized on the chip substrate following a protocol similar to that of ELISpot

assay, which is a common method for quantitative multiplexed analysis of cell-secreted cytokine panels. The platform was used to compare the polycytokine production of healthy CD3+ CD8+ T cells against that of melanoma-associated antigen specified CD3+ T cell. This study successfully demonstrated the advantage of microfluidic technology in acquiring large biological datasets with off-chip optics and spatially mapped fluorescence signals across the chip. This approach has proved very powerful in cellular phenotyping detection, evidenced by the rapidly increasing number of related studies in recent literature [72-76]. Based on these previous studies, we are poised to re-evaluate efforts by the optofluidics research community towards on-chip optics integration targeting POC applications. Through our research, we learned that any advances in optical detection to facilitate laboratory-level assays are also highly valued by the life sciences research community whether they use on-chip or off-chip optics.

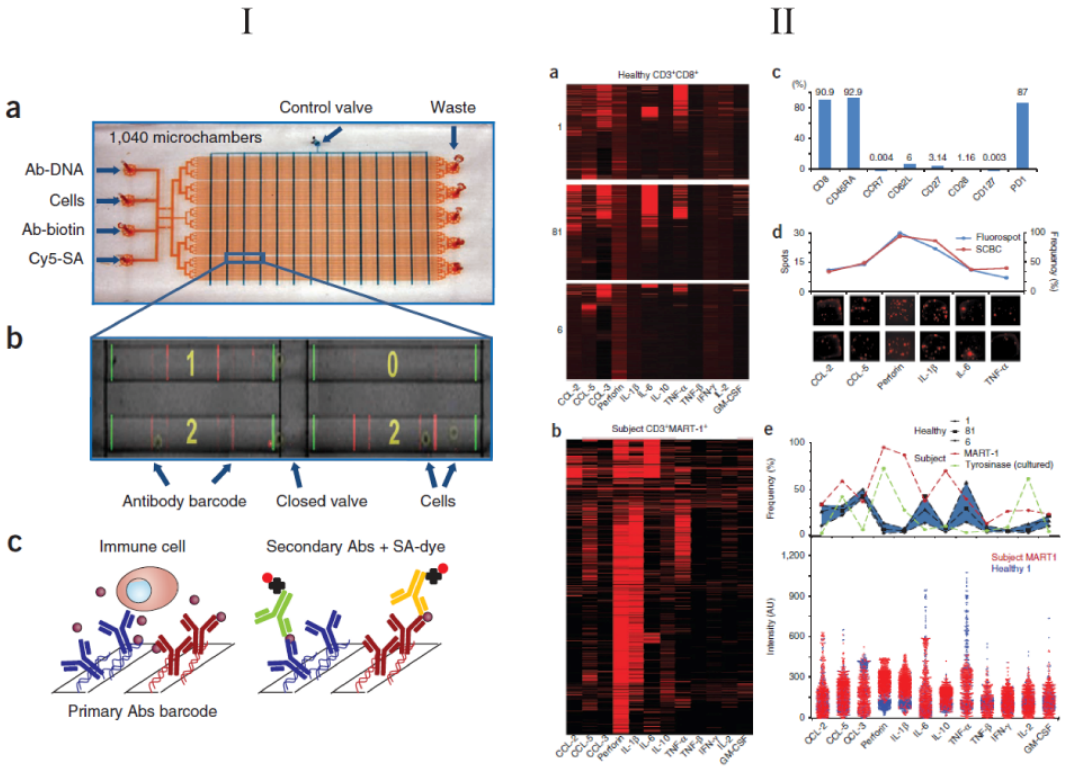

Figure 2-9 (I) Schematic of single-cell barcode chip for cell secreted polycytokine analysis (a) Photograph of two-layer PDMS microfluidic for single cell confinement. (b) The optical micrograph shows the isolated cells in each microchamber and overlaid with fluorescent antibody barcode. (c) Working principle of how cell-secreted antigens attach to primary antibodies and become sandwiched to bind to secondary antibodies conjugated by fluorescent dye for detection. (II) Comparison of polycytokine level between healthy CD3+ CD8+ T cells and melanoma-associated antigen specific CD3+ T cell. Reprinted from [59] with permission from Nature Publishing Group.

The existing microfluidic platforms reviewed here have several limitations for cellular phenotyping. The major problem of current microfluidic flow cytometry settings is the compromised sensing performance resulting from their small system size, such as reduced spectral resolution, a limited number of detectable parameters, and low sample throughput. The major problem of microfluidic cell capture and analysis devices can be characterized by (1) low cell capture efficiency and (2) complicated and time-consuming immunophenotyping assay protocols. These problems prohibit reliable, labor-reduced characterization of cells and limit the devices' applications into real clinical diagnosis.

To address these problems, my thesis work aims to develop two optofluidic platforms to provide an alternative solution. The first platform described in Chapter 3 incorporating a MEMS-based dynamic *in-situ* spectroscopy module provides higher sensing performance in microfluidic flow cytometry setup. The second platform described in Chapter 4 provides higher cell capture efficiency and simplifies immunophenotyping assay protocols with a microfluidic cell analysis setup.

Chapter 3

Microfluidic Multispectral Flow Cytometry

The major content of this chapter is reproduced from our previous publish paper: "Multiplexed Spectral Signature Detection for Microfluidic Color-Coded Bioparticle Flow" in *Analytical Chemistry*, 2010 [77].

3.1 Concept

Suspension microsphere assays, where capture ligands are immobilized on color-coded microspheres, are currently the common antibody-based multiplexed protein immunoassay platforms together with planar microarray technology-based assays [78]. Currently, high-throughput microspheres assay analysis is usually performed by flow cytometry. In a fluorescence flow cytometry setting, fluorescently labeled particles are hydrodynamically injected into a capillary channel to form a single-profile flow, and their emission signals are excited by laser light and quantitatively characterized. Here, selective identification of multiple fluorescent molecular markers is also essential to discriminate diverse analyte species in the original sample mixture.

To achieve continuous multispectral detection capabilities with minimum filters and detectors, we integrate our previous developed strain-tunable nanoimprinted grating

microdevice with a microfluidic flow chamber using simple fiber optics. The established system enables "microfluidic multispectral flow cytometry (MMFC)," which is a flow cytometric measurement technique capable of quantitatively analyzing the spectral signatures of various particles at high speed in a microfluidic system. Our technique enables the multiplexed flow cytometry with a simple optical system only consisting of a *single* excitation laser and a *single* detector. Compared to conventional methods, MMFC can differentiate more subtle parametric variances at high accuracy. Thus, we could add more analytical parameters in flow cytometry with multiple combinations of colors and/or spectral shape variations.

The MMFC is constructed with three units: (1) a fluorescent microscope with an excitation laser (λ= 473 nm); (2) a microfluidic flow chamber; and (3) a spectral detection system consisting of a strain-tunable nanoimprinted grating microdevice and a single photomultiplier tube (PMT) with a slit (Figure 3-1a). The microfluidic channel is placed on the stage of the fluorescent microscope, which provides a convenient platform for focusing light and aligning the microfluidic channel. The sample flow is hydrodynamically focused by two sheath flows of buffer solution. Excitation laser light (λ= 473 nm) is focused on the interrogation zone of the microfluidic channel by the 60X objective (N.A. = 1.4). Emission light from particles flowing in the microfluidic channel is collected at the probe of the embedded optical fiber (orange line). Both objective and embedded optical fiber provide highly focused integration zone, which eliminates the light scattering from the edges of the channel. The collected light is collimated at the end of the optical fiber and dispersed after its transmission through the transparent grating microbridge of the microdevice. The grating diffracts the transmitting light and changes

the diffraction angle with its grating pitch varied by the lateral movement of on-chip actuators (Figure 3-1b). The PMT provides high signal sensitivity and a fast acquisition rate. By adjusting the angular position of the PMT, we can set up the wavelength range to cover the detected emission spectra. A data acquisition system (PCI-6111, National Instruments) and LabVIEW7.0 software (National Instruments) are used to capture the PMT signal and to apply an actuation voltage to the MEMS comb drives.

The grating microdevice used in our study consists of electrostatic microelectromechanical systems (MEMS) actuators and a tunable polymer diffraction grating made from PDMS (Figure 3-1b). The PDMS microbridge containing a grating pattern on the top surface is attached to a suspended silicon shuttle beam containing a series of comb-shaped electrodes while the other end is fixed onto a silicon substrate. Electrical wires are bonded onto on-chip contact pads to connect the device to a power supply generating a sinusoidal voltage signal at 1KHz. The resulting electric fields between the adjacent comb-shaped electrodes generate actuation force driving the oscillatory motion of the shuttle beam. The shuttle beam motion repeatedly stretches and contracts the PDMS grating microbridge in response to the actuation voltage signal. This enables high-speed wavelength tuning capability with the microdevice. The diffraction of light by the grating images a single wavelength or a narrow wavelength band onto a photodetector surface. Fluorescence emission light is collected from a particle flowing in a microfluidic channel and transmitted to the spectroscopy system.

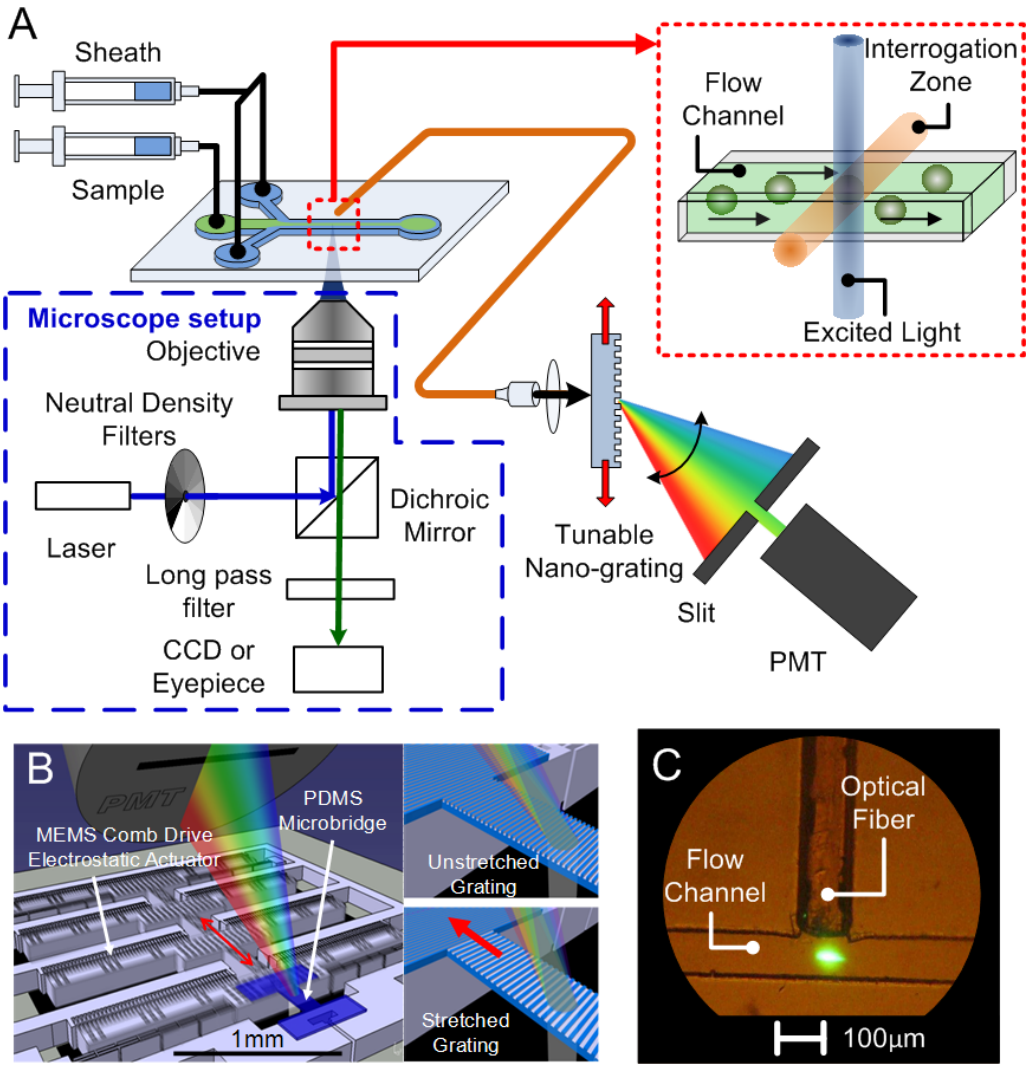

Figure 3-1 (a) Schematic of the microfluidic multispectral flow cytometry (MMFC) setup. The magnified image of the microfluidic channel shows the particle flows (red region). When the particles pass through the interrogation zone, they are optically excited and emit fluorescent signals fed to the embedded optical fiber. (b) 3D schematic drawing of the entire structure of the grating microdevice. The strain-tuning of the grating profile varies the diffraction angle of transmitting light. (c) The optical microscope image of the microfluidic channel shows the snap shot of a hydrodynamically focused particle flow in front of the optical fiber probe.

3.2 Methods and Materials

3.2.1 Construction of Microfluidic Flow Cytometer

The MMFC setup incorporates this device in the spectroscopy system coupled with the optofluidic chamber via an optical fiber waveguide. The optofluidic configuration for the microfluidic flow cytometer was originally proposed in our previous study [28]. The microfluidic chamber is fabricated using PDMS soft lithography with a mold of patterned photoresist. The replicated PDMS structure is then bonded to a 200 μm thick glass slide that forms the bottom layer sealing the chamber. The flow channel cross-sectional area is 100μm x 100μm. The optical fiber with a 100 μm diameter core and numerical aperture (N.A. = 0.22) (F-MCB-T-3 SMA, Newport Corp.) is embedded perpendicular to the microfluidic channel to capture the emission signals from in-flow particles at high efficiency (Figure 3-1c). The integrated fiber serves as an optical waveguide with small signal loss, thus leading to a high signal-to-noise ratio.

3.2.2 Microfabrication and Assembly of Nanoimprinted Grating

To fabricate the strain-tunable nanoimprinted grating microdevice incorporated in the spectroscopy system, we use a fabrication method named the multilevel soft lithographic lift-off and grafting (ML-SLLOG) [79, 80]. The fabrication process involves (i) construction of micrometer-to-millimeter scale silicon comb drives on a silicon-on-insulator (SOI) wafer, (ii) soft-lithographic replica molding and lift-off of a three-dimensional PDMS grating microbridge and (iii) grafting and assembly of the PDMS microbridge onto the silicon comb drives, assisted by surface tension at an air-water

interface. An actuator design with series of 50 μm-thick silicon comb drives is employed as an extension of previous one developed by our group [80]. The design of our previous device is modified to achieve a larger displacement of motion and a stronger actuation force for this study. The PDMS (Dow Corning Corporation. 10:1 base-curing agent ratio) microbridge has a surface feature of 350 grating lines with a nominal period of 700 nm and a height of 350 nm (Figure 3-2). According to the Rayleigh criterion, the wavelength of interest and the number of grating lines determine the spectral resolution. The higher density and quality obtained for the new device design improve the resolving power of the grating. Oxygen plasma treatment for the surfaces of the PDMS grating microbridge bottom and the silicon comb drives is used to promote permanent bonding. Our previous study [80] shows that the PDMS-silicon bonding is strong enough to sustain more than 100 million cycles of operation.

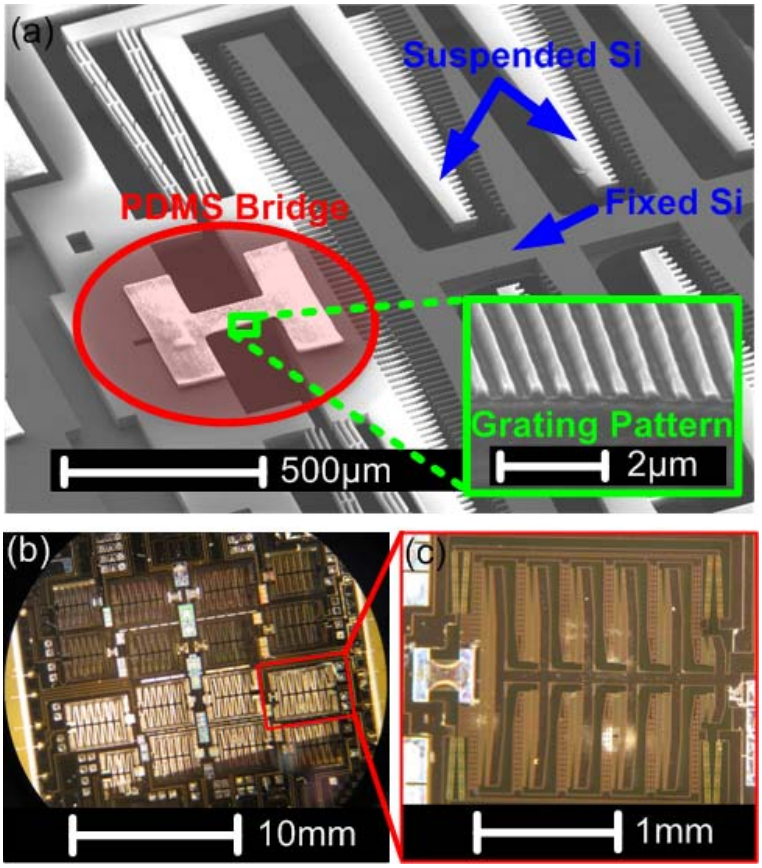

Figure 3-2 (a) SEM image of the entire nanoimprinted grating device and MEMS silicon comb-drive electrostatic actuators. (b) Optical images of 16 nanoimprinted grating device array on a 2 × 2 cm^2 die area (c) Optical image of the whole nanoimprinted grating device unit. The grating microbridge is 300μm in length, 300μm in width, wide, and 20μm in thickness and has a surface pattern with a 700 nm nominal pitch.

3.2.3 Sample Preparation

In this study, we choose two cell types (293T cell and HeyA8 cancer cell) and four color-coded microspheres to validate our system performance. This section describes detailed sample preparation procedures.

293T cells are cultured in a Dulbecco's Modified Esagle Medium (Invitrogen, Carlsbad, CA, USA) with 10% fetal bovine serum, 1% glutamine and 0.1% penicillin/streptomycin. Cells are transiently transfected with CXCR7 fused to GFP or the mcitrine variant of YFP (CXCR7-GFP and CXCR7-YFP) as described previously

[81]. Two days after transfection, cells are mixed at CXCR7-GFP cell-to-CXCR7-YFP cell ratios of: (1) 1:3; (2) 1:1; or (3) 3:1 as enumerated with a hemacytometer. Cells are resuspended in PBS at 2 x 10^6 cells/ml for the experiments.

HeyA8 and HeyA8-GFP ovarian cancer cell lines are cultured and maintained in complete media consisting of DMEM (11995, Gibco) supplemented with 10% (v/v) heat-inactivated fetal bovine serum (FBS, 10082, Gibco) and 1% (v/v) antibiotic-antimycotic (15240, Invitrogen). HeyA8-GFP cells were generated by lentiviral transduction with vector FUGW [82]. HeyA8 and HeyA8-GFP cells are routinely passaged at 70-90% confluence. All cultures are maintained in a humidified incubator at 37^{o}C, 5% CO_2, and 100% humidity. Live staining of HeyA8 cells was performed using the Calcein AM component from the LIVE/DEAD Viability/Cytotoxicity Kit for mammalian cells (L-3224, Invitrogen). Calcein AM diluted in PBS to a final concentration of 1μg/ml was added to HeyA8 cells and incubated for 30 min at 37^{o}C.

Four color polystyrene microspheres with a nominal diameter of 15 μm are used as suspension substrates in 10mL of 0.15M NaCl with 0.05% Tween 20 and 0.02% thimerosal. The suspensions (~0.2% solids) contain 1.0 x 10^6 microspheres per milliliter. In this experiment, each microsphere coded by one of green (F-21010), yellow-green (F-8844), yellow (F-21011), orange (F-8841) fluorescent dyes (FluoSpheres®, Invitrogen Co.). The peak excitation/emission spectra of these microsphere are (450/480), yellow-green (505/515), yellow (515/534) and orange (540/560) (nm).

3.2.4 The Definition of Spectral Signature Profile

In conventional fluorescent microscopy or flow cytometry, the definition of "fluorescence intensity" is total radiant energy emitted by fluorophores over a certain period of time. In practice, it is measured by a photodetector in a specific wavelength band determined by an emission filter. In this case, the "fluorescence intensity" is an integration of the spectrum intensity (i.e., radiant energy emitted at a given wavelength) of fluorophores over the wavelength band. In contrast, our study identifies the "peak intensity" and "peak wavelength" from continuous spectral profile measurements. Here, the "peak intensity" refers to the intensity value of maximum emission, and "peak wavelength" refers to the wavelength value of maximum emission (Figure 3-3a). We first resolve the spectral profiles of different cell groups with a monochromator system consisting of a tunable grating microdevice and a PMT detector (Figure 3-3a). By identifying the intensity and wavelength values of maximum emission, we construct a two-dimensional plot of peak wavelength vs. peak intensity (Figure 3-3b).

To quantitatively identify the spectral characteristics of the emission of different cells or microspheres, we develop a curve fitting scheme based on a MATLAB program. To simplify the analysis process, we use a quadratic function to approximate the shape of a MMFC spectral plot a

$$y = \alpha x^2 + \beta x + \gamma \tag{3.1}$$

where x represents the wavelength, and y represents the spectrum intensity. Here, α, β and γ are called the quadratic coefficient, the linear coefficient, and the constant term,

respectively. The values of α, β and γ mathematically define the spectral shape of the MMFC plot in a given wavelength range.

The graph of a quadratic function forms a parabola, where the positive or negative value of the quadratic coefficient α determines whether the parabola opens upward or downward. The value of α also governs the rate of increase (or decrease) of the quadratic function graph from the vertex; a larger positive value of α makes the function increase faster and the graph appear more closed. The linear coefficient β alone is the declivity of the parabola in a given wavelength range. With a larger value of β, the shape of the spectrum becomes sharper. The constant term γ represents the offset of the spectral curve. To make the comparison clear, the value of γ is adjusted to make each spectrum curve with same peak intensity. The quadratic coefficient α and the linear coefficient β together determine the peak wavelength, which is given by -β/2α. Here, we already have peak wavelength as one of the characteristic parameters. As a result, only one of the values of α and β is additionally needed to uniquely obtain the full mathematical description of the spectral shape since the other value can be uniquely determined from the peak wavelength value.

To give an example of how curve fitting method works, we choose one of HeyA8-Calcein AM spectrum data plot (shown as the dotted line in Figure 3-3) obtained by the MMFC measurement to show how these characteristic parameters are extracted. With the known peak wavelength value (–β/2α), we only vary the value of the linear coefficient. Here, the theoretical curve becomes sharper with the increasing value of β. The least square curve fitting method is applied to obtain the optimal value of β = 51.17, which yields the theoretical curve best fitted to the experimental HeyA8-Calcein AM

spectrum data plot (the dot line in Figure 3-3c). By comparing the linear coefficient of the quadratic function, we can quantitatively differentiate the spectrum difference of fluorescent labeled cells or microspheres with similar spectra.

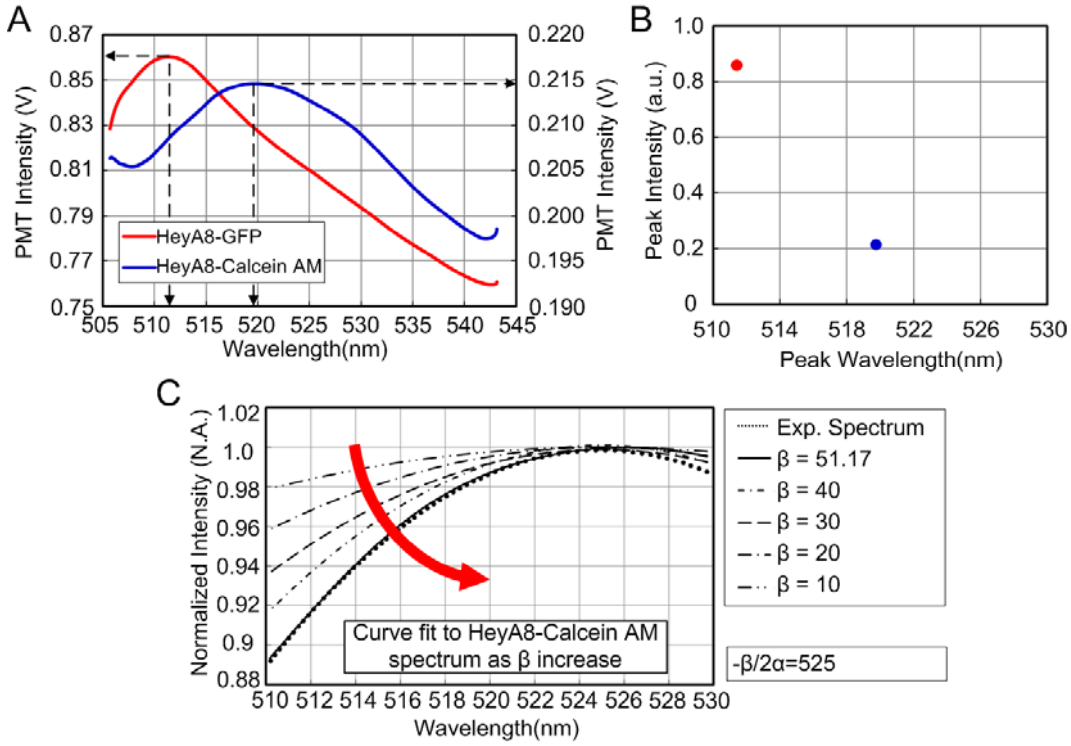

Figure 3-3 Definition of peak wavelength, peak intensity and linear coefficient (a) Spectrum plots of HeyA8-GFP and HeyA8-Calcein AM (b) By finding the intensity and wavelength value of maximum emission, a two-dimensional plot of peak wavelength vs. peak intensity can be generated (c) Effect of the linear coefficient β on the spectrum shape.

3.3 Results and Discussions

3.3.1 Dynamic *In-situ* Spectral Detection Performance

Using the MMFC setup, we first demonstrate dynamic *in-situ* spectral detection for particles in flow. Here, a solution of green colored polystyrene microspheres (the maximum emission at λ =523 nm) with PBS buffer is loaded into the sample syringe.

Both the sample and sheath flow rates are set to be 5μL/min. Data show 30 intensity peaks in a one second time window (Figure 3-4a), each coming from the emission of a green polystyrene microsphere passing. The time evolution of individual PMT signals in response to the actuation voltage signal of the mechanically tunable nanoimprinted grating microdevice is shown in the magnified time scale (Figure 3-4b). A single spectral sweep is completed as either the single stretching or contracting cycle of the grating takes place in 500 μs. A sinusoidal MEMS actuation voltage (140 V peak to peak with 20V DC offset) is set at 1 KHz to perform high-speed spectral sweeping. The PMT signals are obtained at a 1 MHz acquisition rate. With the grating periodicity known for any actuation voltage level, the wavelength of the monochromatic light incident at the angle of the PMT is calculated using the grating equation, which allows us to construct spectrum plots [44, 83]. In this measurement, nearly 5 spectral sweeps within a 5ms time window can be performed for each passage of a single microsphere in front of the optical fiber probe (Figure 3-4c). The PMT signal data are converted to the spectral plots based on a strain-voltage calibration curve and the grating equation [80]. Here, the PMT intensity is given in terms of the output signal voltage. Using a quadratic curve fitting method (Figure 3-3), we can obtain the linear coefficient of this continuous spectrum profile as another characteristic parameter, which provides additional information to help discriminate different sample groups.

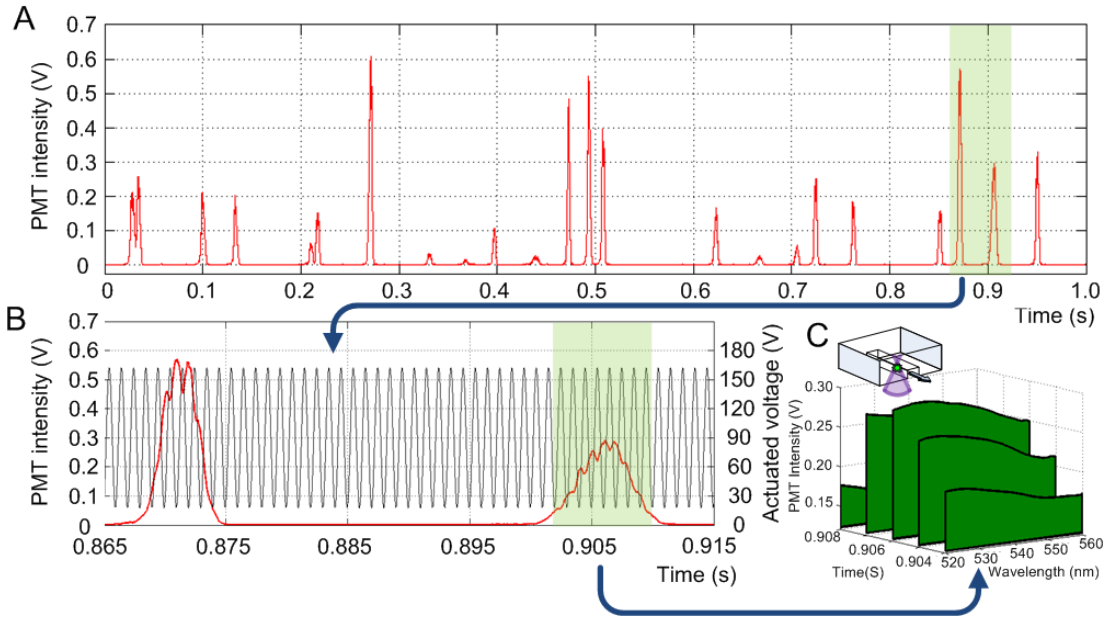

Figure 3-4 Time-domain data resulting from the dynamic *in-situ* spectral detection of in-flow particles. (a) A time-domain plot showing PMT signals. (b) A magnified plot of the PMT signals (red curve) superimposed with the corresponding actuation voltage signal applied to the MEMS comb drive actuators (black curve) in 0.865-0.915 second interval. (c) A plot of the real-time spectral signals from a flowing single green colored polystyrene microspheres.

3.3.2 Green/Yellow Fluorescent Protein Spectrum Discrimination

With the spectral acquisition process established for our optofluidic system, we further demonstrate the ability to discriminate two spectrally similar fluorescent proteins by MMFC. The cell groups consist of human embryonic kidney 293T cells transfected with CXCR7 fused to green fluorescent protein (GFP) or the mCitrine variant of yellow fluorescent protein (YFP). The standard emission spectra of GFP and YFP have a significant spectral overlap (Figure 3-5a) [84]. From the MMFC setup, we can reconstruct these two similar spectra, and the linear coefficient of each spectrum can be resolved in a 510-530nm wavelength range. We prepare samples with three known population fractions of CXCR7-GFP and CXCR7-YFP cells: (i) 1:3; (ii) 1:1; and (iii) 3:1 by hemocytometery prior to the MMFC measurements. The experimental data with N =

125, 199, and 387 for samples (i), (ii), and (iii), respectively, are obtained by a 30-second measurement. Samples flow into the microfluidic channel for MMFC measurements and spectral data for individual cells are obtained for 30 seconds. We analyze the characteristics of the continuous spectral plot for each cell flowing through the interrogation zone that are quantified by peak wavelength (i.e. the wavelength value of maximum emission), peak intensity (i.e. the intensity value of maximum emission) and linear coefficient (Figure 3-3). We count the numbers of cells belonging to the two color groups from the spectral characteristics and plot their ratio for each sample (Figure 3-5c). Here, we take 520 nm and 0 as the cut-off values for the peak wavelength and the linear coefficient, respectively, which are reasonable values judged from the spectra of GFP and YFP (Figure 3-5a-b). For example, the linear coefficient-versus-peak wavelength plot taken for the 1:1 sample shows two statistically distinct groups with a population ratio of nearly 1 (49.59% CXCR7-GFP and 47.11% CXCR7-YFP cells of total cell population flowing by in 30 seconds) (Figure 3-5d). Our data show good agreement between the experimentally measured and predetermined CXCR7-GFP/YFP cell population fractions for all of the samples (Figure 3-5c-d). This validates the numeration accuracy of the MMFC technique proposed here.

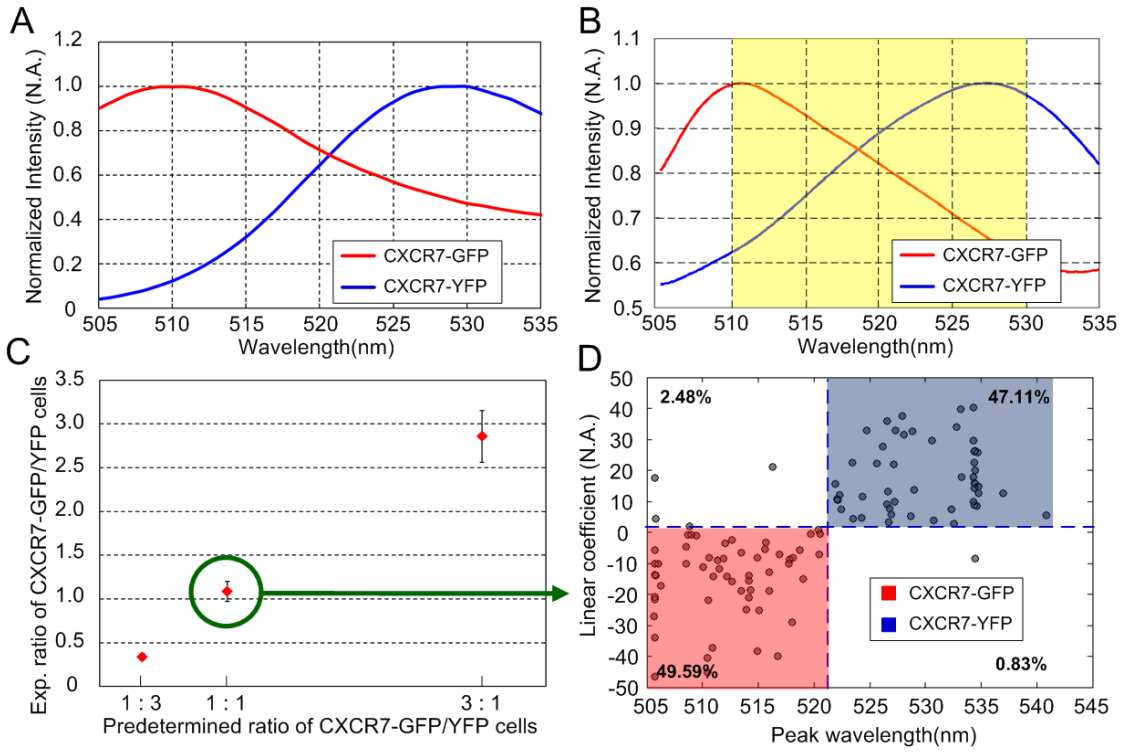

Figure 3-5 Discrimination of fluorescent proteins with similar spectra by MMFC. (a) Standard normalized emission spectrum of GFP and the mCitrine variant of YFP. (b) Normalized emission spectrum of GFP and YFP measured by MMFC setup. The linear coefficient of spectrum is resolved in a 510-530nm wavelength range (yellow region). (c) Comparison of the predetermined and experimentally measured population ratios for mixtures of suspended CXCR7-GFP and CXCR7-YFP cells. (d) The 2D plot maps the peak wavelength and linear coefficient taken for a particular 1:1 cell control mixture (green circle in (c)).

3.3.3 Four-colored Microspheres Spectrum Discrimination

Subsequently, we perform dynamic *in-situ* spectral detection for four types of in-flow polystyrene microspheres (15μm in diameter) with different colors by MMFC. We adjust the tunable grating strain ratio and the PMT angle to achieve a 518-558nm wavelength tuning range, where these microspheres exhibit notable spectral overlaps (Figure 3-6c). Each particle flows through the microfluidic channel (flow rate is 10μL/min) and its spectral signature is captured from the PMT signal. The polystyrene microspheres are named according to their emission colors: (i) green, (ii) yellow-green, (iii) yellow, and (iv) orange. Each sample group consists of N = 100 data points. From the continuous

spectrum measurement, we can map the maximum intensity and wavelength of maximum intensity of each microsphere color type in the 518-558nm wavelength range (Figure 3-6b). The percentage values represent the confidence levels of data discrimination with the dividing lines. The subfigure shows normalized fluorescence emission spectra for the polystyrene microspheres. The histograms (Figure 3-6a and Figure 3-6d) show the particle population distributions for each of these spectral parameters. By using the combination of the two parameters, the four fluorescent color bands of the polystyrene microspheres can be discriminated even in such a narrow wavelength bandwidth as 40nm. Here, we prove that information from the continuous spectral plots provides high multiplicity for MMFC even if the wavelength bandwidth employed for the measurement is limited. It should be noted that the use of the particles coded by spectrally similar colors enables our system to carry out high-speed, multiplexed detection with a *single* excitation source and a *single* photodetector. This represents a capability unique to MMFC that has not been demonstrated with conventional flow cytometry settings.

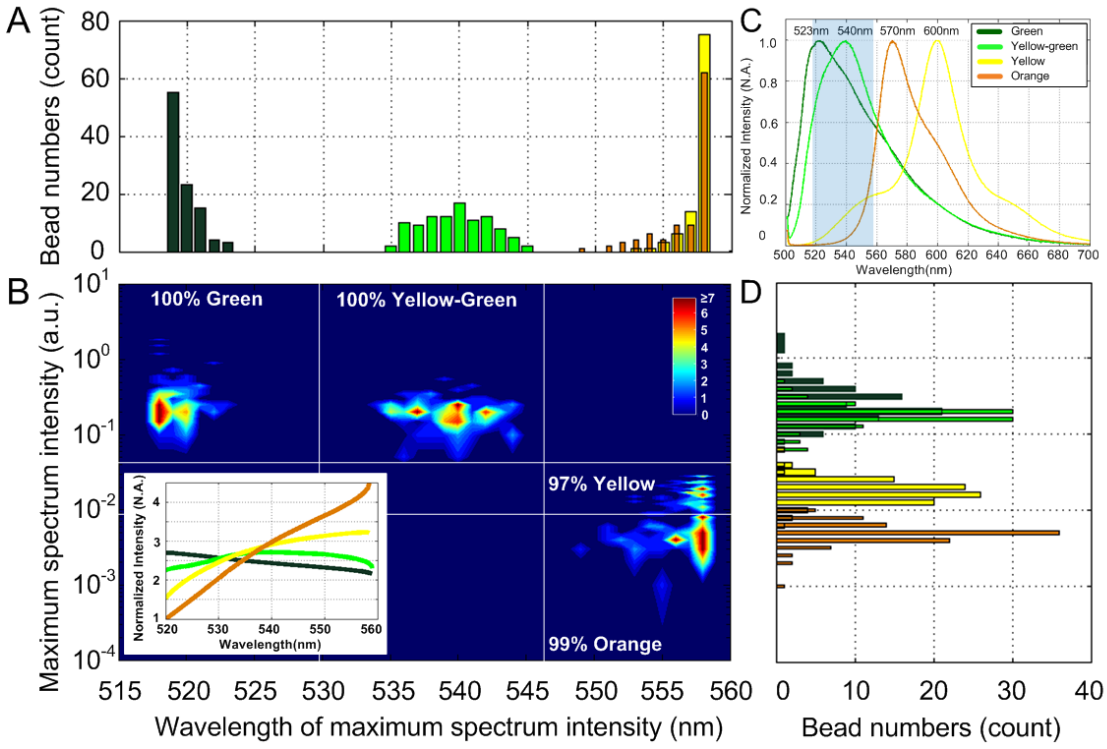

Figure 3-6 Four color discrimination of polystyrene microspheres by MMFC. (a) A univariate histogram of the wavelength of maximum spectrum intensity at λ = 518-558 nm. (b) A population density contour plot for the maximum spectrum intensity and the wavelength of maximum spectrum intensity at λ = 518-558 nm. (c) Spectral data of the microspheres measured by a commercial spectrometer (Ocean Optics, USB4000). (d) A univariate histogram of the maximum spectrum intensity at λ = 518-558 nm.

3.3.4 Two Color-coded Living Cells Spectrum Discrimination

We finally repeat the measurement for two types of color-coded cells whose emission spectra have very similar intensities and profiles. Here, we employ ovarian surface epithelial tumor cell lines, HeyA8, stably transduced with GFP and stained with Calcein AM. To compare our technique with conventional flow cytometry, we flow HeyA8 cell groups with three different labels: (1) HeyA8-GFP cells, (2) HeyA8-Calcein AM cells and (3) unstained HeyA8 cells in a commercial flow cytometer (BD LSR II, BD bioscience). The sample of the unstained HeyA8 cells is used as a control. The system uses blue octagon (488nm) laser excitation and FITC (500nm long pass dichroic mirror

with 530/30nm bandpass filter) and PE (550nm long pass dichroic mirror with 575/26nm bandpass filter) channels. We obtain a univariate histogram of FITC fluorescence (Figure 3-7a), an overlay bivriate histogram of FITC fluorescence versus PE fluorescence (Figure 3-7b) and a univariate histogram of PE fluorescence (Figure 3-7c) for the three sample groups. In Figure 3-7b, 97% of the HeyA8-GFP cell population overlaps with 86% of the HeyA8-Calcein AM cell population. The significant spectral overlap between GFP and Calcein AM prohibits us to statistically distinguish the two sample groups by the two-parameter flow cytometry setup.

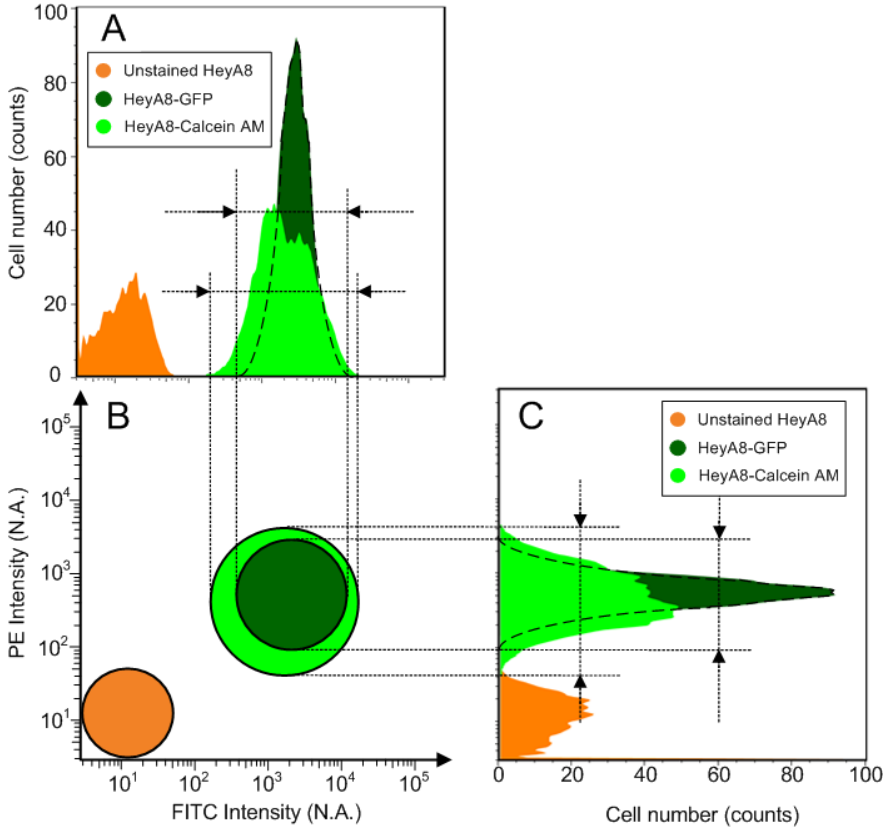

Figure 3-7 HeyA8 cell analysis by the commercial flow cytometry (BD LSR II, BD bioscience). (a) A univariate histogram of FITC fluorescnece. (b) A bivariate histogram of FITC fluorescence versus PE fluorescence. (c) A univariate histogram of PE fluorescence.

Because of their similar fluorescence intensities, i.e. spectrum intensities integrated over the wavelength band of the emission filter, and spectral shapes (Figure 3-8a-f), these fluorescent labels cannot be distinguished by conventional fluorescent microscopy or flow cytometry. In contrast, with the combinations of the three characteristic parameters (e.g., peak wavelength, peak intensity and linear coefficient) of the continuous spectral profiles, the cell groups can be clearly segregated in the three-dimensional (3D) cell population distribution space (Figure 3-8g). The mean value and standard deviation of HeyA8-GFP and HeyA8-Calcein AM cell groups for the three parameters are tabulated (Table 2). However, because the emissions of HeyA8-GFP and HeyA8-Calcein AM strongly depend on the expression level of GFP, the degree of Calcein AM staining strength, and the total number of alive cell population, the "peak intensity" may not be an intrinsic signature indicative to differentiate these two cell groups and will be, therefore, eliminated in our analysis later.

To quantitatively assess our system's discrimination power for these two cell groups, we construct a two-dimensional (2D) cell population contour plot of peak wavelength vs. linear coefficient (Figure 3-8h) from the 3D cell population distribution plot (Figure 3-8g). We first set 10-15 gridlines for each parameter in 2D cell distribution plots, and then count the number of data points that fall in each mesh area. The value of this number is represented by the color of the mesh area. With this information, two regions with a GFP or Calcein AM population density peak are determined for each 2D contour plot. A perpendicular bisector of the line connecting the two population peaks is taken as the dividing line between the two regions. We then calculate the fractions of the GFP-labeled and Calcein AM-labeled cells whose data points fall in the GFP and Calcein AM

regions for the cell distribution plots (Figure 3-8i). Each region includes nearly 85% of the total population of the particular cell group. The data points of the remaining 15% population that fall in the region of the other cell group represent false positives of the measurements.

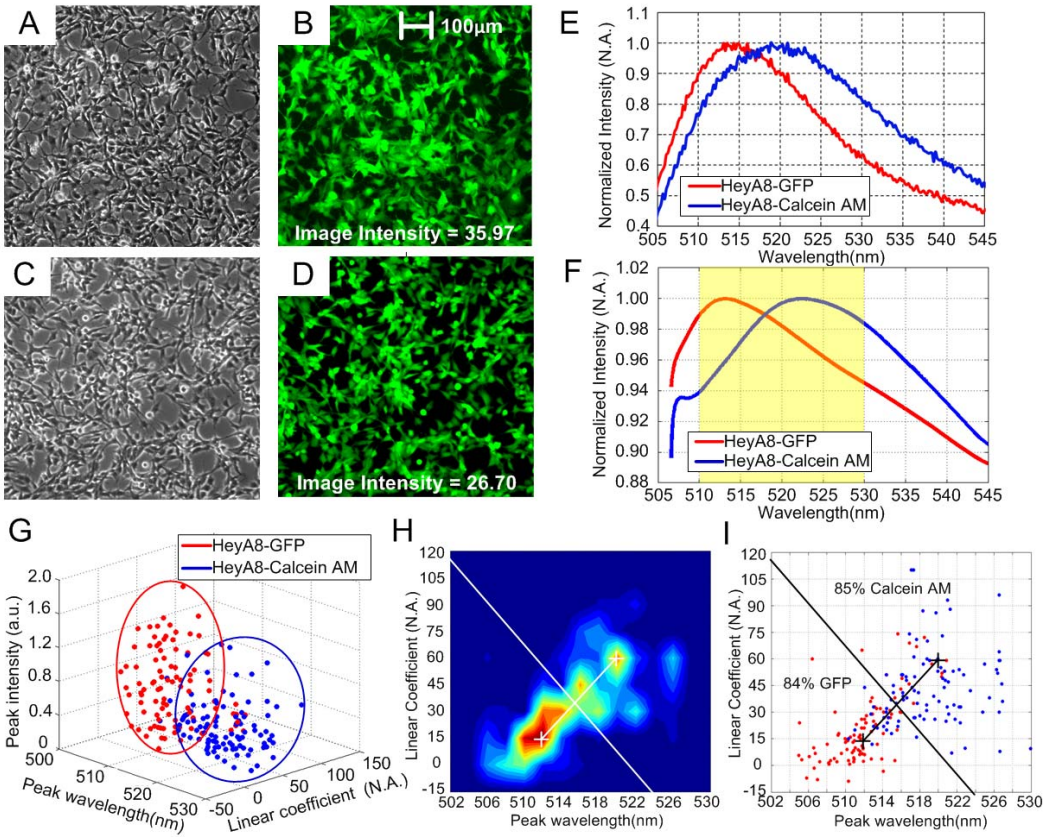

Figure 3-8 MMFC distinguishes fluorophores with nearly identical emission spectra in living cells. (a-d) 10X microscopy images of HeyA8-GFP cells in (a) the brightfield view and (b) the fluorescent imaging mode. 10X microscopy images of HeyA8-Calcein AM cells in (c) the brightfield view and (d) the fluorescent imaging mode. The fluorescent images are taken in the FITC filter band. The numbers in (b) and (d) represent the average fluorescence image intensity in the field of view. Normalized fluorescence emission spectra of HeyA8-GFP and HeyA8-Calcein AM cells measured by (e) a commercial spectrometer (Ocean Optics, USB4000) and (f) MMFC setup. (g) Three-dimensional (3D) plot of the peak wavelength, peak intensity, and linear coefficient of the spectral signatures for both HeyA8-GFP and HeyA8-Calcein AM cells (N=181). (h) Two-dimensional contour plot of peak wavelength vs. linear coefficient obtained from the projection of (g). The perpendicular bisector of the line connecting the two population peaks is taken as the dividing line between the two regions. (i) The ratio of the GFP-labeled and Calcein AM-labeled cells whose data points fall in the GFP and Calcein AM regions are calculated based on the cell distribution plot of peak wavelength vs. linear coefficient, obtained from the projection of (g).

Table 2 Statistical analysis of HeyA8-GFP and HeyA8-Calcein AM groups

		Mean	Standard deviation
Peak wavelength of	GFP	511.98 (nm)	3.44 (nm)
	Calcein AM	519.04 (nm)	4.19 (nm)
Peak intensity of	GFP	0.78 (N.A.)	0.43 (N.A.)
	Calcein AM	0.39 (N.A.)	0.28 (N.A.)
Linear coefficient of	GFP	20.82 (N.A.)	19.29 (N.A.)
	Calcein AM	43.65 (N.A.)	22.30 (N.A.)

Chapter 4

Microfluidic Immunophenotyping Assay Device

The major content of this chapter is reproduced from our previous publish paper: "An integrated microfluidic platform for in situ cellular cytokine secretion immunophenotyping" in *Lab on a Chip*, 2012 [85].

4.1 Concept

The main objective of this study is to perform a rapid, quantitative detection of cell-secreted biomarker proteins assay with low sample volume and shorter incubation time by developing a microfluidic immunophenotyping assay (MIPA) device. Here, we use the human acute monocytic leukemia cell line, THP-1, as a model for mimicking the functional immune responsiveness of human monocytes. Our microfluidic device allow us to capture and stimulate cells with a canonical stimulant, lipopolysaccharide (LPS), to simulate a human immune response that is routinely characterized by cytokine production [86]. The detected cytokine is tumor necrosis factor-α (TNF-α), a pro-inflammatory cytokine and a key biomarker associated with host defense and immunosurveillance [87-89]. TNF-α secretion from LPS-stimulated immune cells has been shown to reflect a functioning innate immune response [48, 49, 90].

The structure of the MIPA device consisted of three different PDMS layers (Figure 4-1a). The top and bottom PDMS layers were the cell culture and immunoassay chambers, respectively, and the middle layer was a PDMS microfiltration membrane (PMM). The top cell culture chamber of the MIPA device was designed for seeding and stimulation of THP-1 cells using LPS. The bottom immunoassay chamber of the MIPA device was designed for loading immunoassay beads and optical detection of AlphaLISA signals. The size of both the cell culture and immunoassay chambers is 3.7mm (L: length) × 3 mm (W: width) × 100 μm (H: height). The inset of Figure 4-1a shows the pre-filter structure (300 μm L × 50 μm W × 100 μm H) to block particles larger than 50μm in diameter (e.g. aggregated cells) and the supporting posts to prevent deformation of the PMM. The supporting post diameter is 50 μm with a center-to-center distance of 200 μm. Embedded between the top and bottom microfluidic layers was the PMM, which was designed (1) for isolation and enrichment of THP-1 cells and (2) for allowing cytokines secreted from LPS-stimulated cells to diffuse rapidly into the bottom immunoassay chamber for quantitative immunosensing. The PMM contained an array of closely packed through holes of 4 μm in diameter and with a center-to-center distance of 10 μm. The PMM had an effective filtration area of 7 mm^2 and a thickness of 10 μm. The cell isolation and cytokine diffusion efficiency is critically dependent on the membrane porosity, which is defined as the ratio between the total pore area to the total membrane area. In this work, we successfully fabricated the PMM with 25% porosity. In comparison, conventional track-etched polycarbonate filters used for blood cell isolation has reported porosity of less than 2% [91, 92]. The other more recently developed Parylene-based micropore membrane has porosity of 7%-15% [93]. Even with this high

porosity of 25% in the PMM, we did not observe any deformation of the PMM during all cell loading experiments (with a flow rate from 1 to 10 μL/min), suggesting the PMM structure has superior mechanical robustness owing to the supporting post structures integrated in both the cell culture and immunoassay chambers.

Figure 4-1b shows the immunophenotyping assay protocol used in this study: First, the PMM isolates and enriches THP-1 cells. Second, LPS is introduced to stimulate cells. Third, AlphaLISA beads are loaded and incubated in the immunoassay chamber. Finally, the customized optics is used to detect AlphaLISA signal.

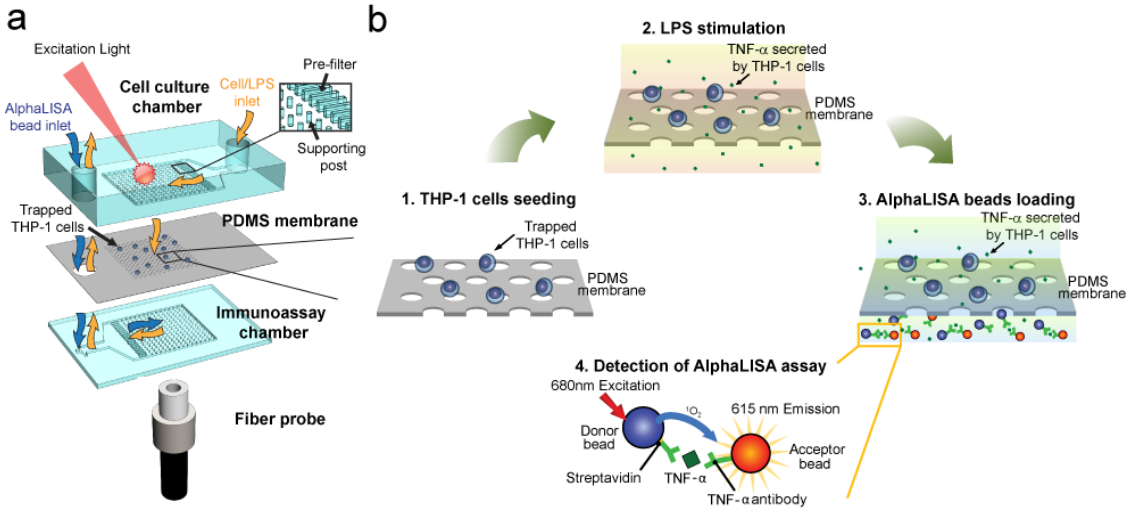

Figure 4-1 Functional immunophenotyping using the MIPA device. (a) Schematic of the multi-layered MIPA device consisting of a cell culture chamber, a PDMS microfiltration membrane (PMM), and an immunoassay chamber. A fiber probe was attached underneath the immunoassay chamber to collect AlphaLISA emission signal. (b) Schematic of the immunophenotyping assay protocol. In this study, TNF-α is detected by the AlphaLISA assay, in which the streptavidin-coated donor (blue) and acceptor beads (orange) are both conjugated with TNF-α antibodies.

4.2 Methods and Materials

4.2.1 Microfabrication and Assembly

The PMM was fabricated using a PDMS surface micromachining technique described previously [94]. Briefly, a silicon wafer was first activated using the O_2 plasma (Plasma Cleaner PDC-001, Harrick Plasma) for 2 min and silanized with (tridecafluoro-1,1,2,2,-tetrahydrooctyl)-1-trichlorosilane vapour (United Chemical Technologies) for 1 hr under vacuum to facilitate subsequent release of patterned PDMS layers. PDMS prepolymer (Sylgard-184, Dow Corning) was prepared by thoroughly mixing the PDMS curing agent with the PDMS base monomer (*wt*:*wt* = 1:10). PDMS prepolymer was then spin-coated on the silanized silicon wafer at a spin speed of 7,000 rpm and completely cured after baking at 110°C for 4 hr. The PDMS surface was activated using the O_2 plasma for 5 min to allow a uniform photoresist coating for photolithography. After the O_2 plasma activation, photoresist (AZ 9260, AZ Electronic Materials) was spin-coated on PDMS, soft-baked at 90°C for 10 min, and then patterned using contact photolithography. The silicon wafer was then processed with reactive ion etching (RIE; LAM 9400, Lam Research) using SF_6 and O_2 gas mixtures to transfer patterns from patterned photoresist to the underlying PDMS layer. During RIE, reactive gas ions will etch exposed PDMS regions anisotropically. Photoresist was then striped using organic solvents, leaving patterned PDMS thin films on the silicon wafer. Scanning electron microscopy (SEM) images were then taken for inspection of the geometrical features of the PMM, in which the PMM was mounted on stubs, sputtered with gold palladium, observed and photographed under a SEM machine (Hitachi SU8000 Ultra-High Resolution SEM).

The cell culture and immunoassay PDMS chambers were fabricated using soft lithography. Briefly, silicon molds were first fabricated using photolithography and deep reactive ion-etching (DRIE) (Deep Silicon Etcher, STS). The silicon molds were then silanized with (tridecafluoro-1,1,2,2,-tetrahydrooctyl)-1-trichlorosilane vapor for 4 hr under vacuum to facilitate subsequent release of PDMS sturcutures from the silicon molds. PDMS prepolymer with a 1:10 *wt* ratio of PDMS curing agent to base monomer was poured onto the silicon molds and cured at 110°C for 4 hr. Fully cured PDMS structures were peeled off from the silicon molds, and excessive PDMS was trimmed using a razor blade. O_2 plasma-assisted PDMS-PDMS bonding process was then used to assemble the cell culture and immunoassay chambers with the PMM to form a completely sealed MIPA device. Assembly of the MIPA device was performed under eye inspection using alignment marks of the cell culture and immunoassay PDMS chambers.

4.2.2 Numerical Simulation of Device

The commercial finite-element method (FEM) software (COMSOL 4.2a Multiphysics) was used to simulate the flow velocity field and cytokine diffusion in the MIPA device (Figure 4-2). The flow velocity field pattern in the MIPA device was calculated using the incompressible *Navier-Stoke*s equations:

$$\begin{aligned} \rho(\mathbf{u} \cdot \nabla)\mathrm{u} &= \nabla \cdot [-\mathrm{pI} + \mu(\nabla \mathbf{u})] \\ \nabla \cdot \rho \mathbf{u} &= 0 \end{aligned} \tag{4.1}$$

where μ denoted the dynamic viscosity (kg/(m·s)), ρ represented the fluid density (kg/m^3), u was the flow velocity (m/s), p denoted the pressure (Pa), I was the inertia force, and F

was the external body force. A velocity boundary condition was set to be u (=0.001m/s) and zero at the inlet and the outlet, respectively. To simplify our simulation, we developed a computational model with an array of 30 × 30 through holes to estimate the *x-y* and *y-z* direction flow pattern in the MIPA device. The hole diameter was 25 μm with the hole center-to-center distance of 100 μm. The total PMM area was 3 mm × 3 mm.

The cytokine diffusion profile was estimated using the transient convection and diffusion mass transfer equation:

$$\frac{\partial c}{\partial t} + \nabla \cdot (-D\nabla c + cu) = 0 \tag{4.2}$$

where c was the concentration (mol/m^3), D denoted the diffusion coefficient (m^2/s), and u was the flow velocity (m/s). In the cytokine diffusion model, LPS-stimulated cells were considered as the cytokine secretion source with the initial concentration of C_0. To simplify our simulation, we assumed 25 single cytokine-secreting cells were uniformly distributed on the PMM.

For the cytokine diffusion model, the size of cytokine secreting cell was set to 25 μm. The time-dependant mass transfer equation was used with the diffusion coefficient (D) of TNF-α of 10^{-10} m^2/s and the initial TNF-α concentration (C_0) of 1.0 nM/mm^2; all values used in our simulation were from our experimental conditions or results reported in literature [95, 96]. In the time-dependant diffusion model, the velocity boundary condition at both the inlet and outlet of the cell culture and immunoassay chambers were set to zero, and secreted cytokines were homogenized over the MIPA device purely through diffusion.

To reduce the computational load in our numerical simulation, we modelled the PMM as a membrane with holes of 25 μm in diameter and their center-to-center distance of 100 μm, which has a coarse distribution of holes than the real PMM design (4 μm hole diameter and 10 μm spacing). The membrane hole dimensions used in this model are expected to yield a worse cell flow condition than the actual design. Our simulation results in Figure 4-2c still showed sufficiently uniform flow distributions in the middle *x*-*y* plane of both the cell culture and immunoassay chambers in the MIPA device. Therefore, we could ensure that the real PMM design, having a finer and more dense hole pattern, would enable us to obtain a flow velocity distribution and an analyte diffusion profile both at high uniformity. Figure 4-2d plotted the spatial distribution of the TNF-α concentration over time. After diffusion for 10 sec, the TNF-α concentration became largely homogeneous within both the cell culture and the immunoassay chambers of the MIPA device. Our simulation result suggested that TNF-α secreted by THP-1 cells in the MIPA device could rapidly become spatially homogeneous owing to the miniaturized microfluidic environment of the MIPA device.

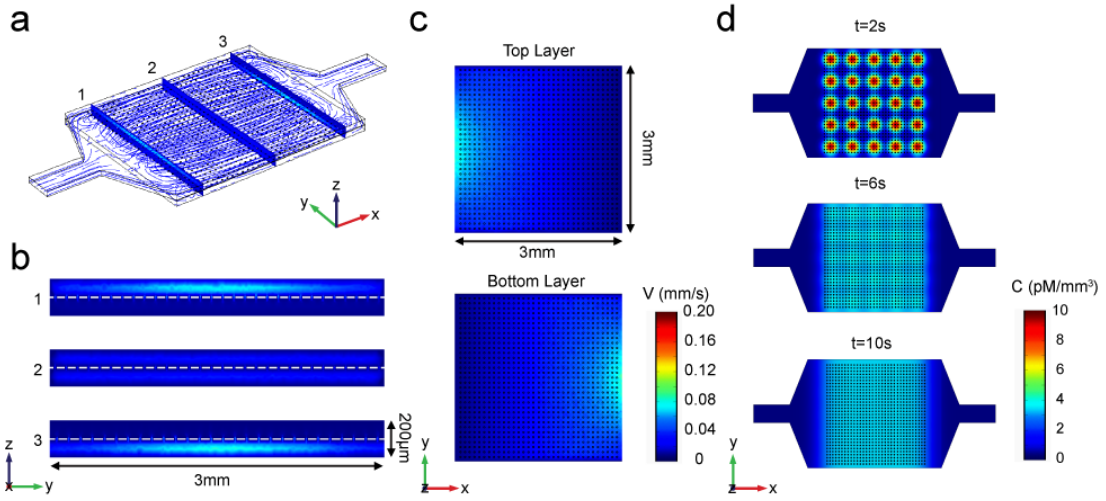

Figure 4-2 Finite element simulation of MIPA device (a) Three dimensional velocity field and flow stream line profile of MIPA device. Slice figures show the detailed velocity field in the (b) *y*-*z* plane and (c) *x*-*y*

plane. The model sets the inlet and outlet velocities to 0.001m/s and zero, respectively. (d) Time lapse of the TNF-α diffused concentration in MIPA device. Diffusion coefficient $D=10^{-10}m^2/s$. Initial THP-1 cell secreted TNF-α concentration $C_0=1.0nM/mm^3$. The model sets the both inlet and outlet velocities to zero.

4.2.3 Cell Culture Conditions

THP-1, the human acute monocytic leukemia cell line, is a commonly used cell type in various researches for immunophenotyping studies [59, 97]. In our work, THP-1 cells were cultured in a complete cell growth medium (RPMI-1640, ATCC) supplemented with 0.05 mM 2-mercaptoethanol (Invitrogen) and 10% (*v*/*v*) heat-inactivated fetal bovine serum (FBS, Gibco). Cells were maintained at 37^{o}C with 5% CO_2 and 100% humidity.

To determine specificity of cellular activation, in some studies, THP-1 cells were "deactivated" or "reprogrammed" to a state of immune paralysis by culturing in the complete growth medium supplemented with 10 ng/mL LPS for 24 hr before loading the cells into the MIPA device for immunophenotyping. This *in vitro* treatment has been commonly employed to induce endotoxin tolerance in THP-1 cells so that they are subsequently unresponsive to LPS [98].

To examine viability of THP-1 cells after LPS stimulation, LIVE/DEAD® Viability/Cytotoxicity Kit for mammalian cell (L-3224, Invitrogen) was used. Specifically, Calcein AM and Ethidium homodimer-1 diluted in PBS to a final concentration of 1 μM and 2 μM, respectively, were added to THP-1 cells captured on the PMM for 30 min before the cells were examined under fluorescence microscopy for quantification of cell viability. A 130 W mercury lamp (Intensilight C-HGFIE, Nikon) was used for fluorescent illumination. Calcein AM was visualized with a FITC filter set

(excitation, 498 nm; emission, 530 nm; Nikon), while ethidium homodimer-1 was visualized with a Texas Red filter set (excitation, 570 nm; emission, 625 nm; Nikon).

4.2.4 AlphaLISA Assay

Our biomarker detection scheme in the MIPA device employed a bead-based chemiluminescence assay, called AlphaLISA (PerkinElmer). AlphaLISA is a no-wash, homogeneous bead-based sandwich immunoassay technique well validated by the standard ELISA technique in previous studies [99, 100]. AlphaLISA eliminates washing and blocking steps required for ELISA that often result in analyte dilution and potential human contaminations. AlphaLISA is based on photo-induced chemiluminescence between pairs of antibody-conjugated donor and acceptor beads (250 - 350 nm in diameter) in close proximity to each other in the presence of a sandwiched analyte molecule (Figure 4-1b, step 4) [97]. When the analyte is captured by sandwich antibodies, both antibody-conjugated donor and acceptor beads are brought into close proximity (< 200 nm) to each other. Upon a laser excitation at 680 nm, donor beads will generate singlet oxygen triggering a cascade of chemical events in the acceptor bead, resulting in a sharp chemiluminescent emission from the acceptor bead peaking at 615 nm. The emission signal from acceptor beads is only generated when the antibodies conjugated on both donor and acceptor beads capture analytes. Thus, AlphaLISA is highly specific and can preserve biological activities of immune cells that can be disrupted by blocking or washing steps required in ELISA.

4.2.5 Optical Detection Setup

The MIPA device was placed on a customized optical setup for detection of the AlphaLISA signal (Figure 4-3a). In this setup, a 500mW 680 nm laser diode (S-67-500C-100-H, Coherent) was used to induce singlet oxygen from AlphaLISA donor beads. An optical fiber (A57-746, Edmund Optics) with a signal collection area of 1,000 μm in diameter and N.A. of 0.22 was placed underneath the MIPA device to collect AlphaLISA emission signal, which was transmitted through the optical fiber and detected by a photomultiplier tube (PMT) (H9306-03, Hamamatsu). A 660 nm shortpass filter (ET660SP, Chroma) and an electronic shutter (DSS1033250A, Unibliz) were placed in front of the PMT to cut off undesired scattering light from the excitation laser. A function generator (Agilent) was used to control timing of triggering the laser pulse for excitation and of opening the shutter in front of PMT for collecting AlphaLISA signal. Both laser pulse and PMT signals were recorded by a multifunctional data acquisition card (NI PCI-6111, National Instruments). Signal analysis software custom-developed using LabVIEW 7.0 (National Instruments) program was used for simultaneous recording of time-sequenced shutter trigger and emission signal detected by the PMT.

To generate the TNF-α standard curve, known amounts of TNF-α were spiked in RPMI media (0-10,000 pg/mL). Then, 10 μg/mL AlphaLISA acceptor beads, 10 nM biotinylated TNF-α antibody and 400 μg/mL streptavidin-coated donor beads were mixed with the TNF-α spiked solution. The AlphaLISA signal was measured using the same customized optical system as a function of the TNF-α concentration and fitted by a sigmoid dose-response curve using GraphPad Prism software.

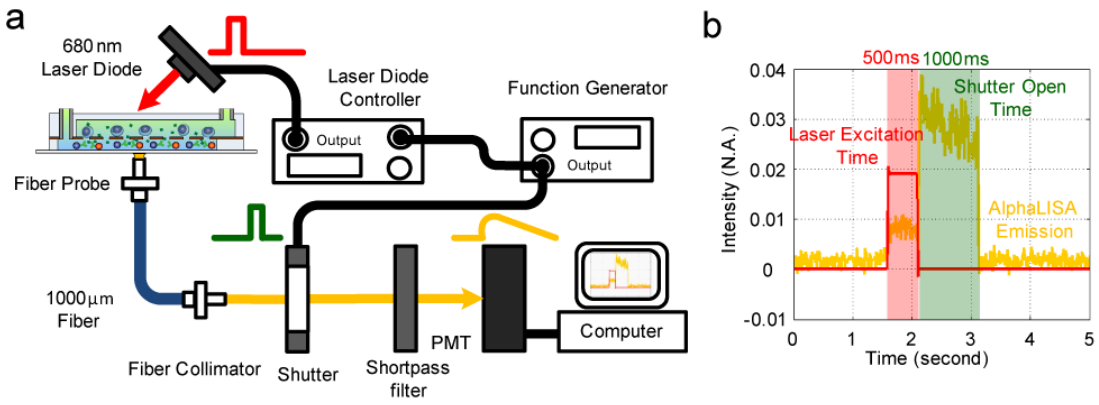

Figure 4-3 Detection of TNF-α secreted from THP-1 cells using the AlphaLISA assay and the MIPA device (a) Schematic of a customized optical setup for the on-chip AlphaLISA signal detection. A laser diode was placed and aligned on the top of the MIPA device for AlphaLISA excitation. A fiber probe was attached under the MIPA device using immersion oil to achieve close to 100% optical coupling. For collection of AlphaLISA emission signal, an electronic shutter and a 660 nm shortpass filter were placed in front of a PMT to cut off unwanted scattering light. (b) Plot of time-sequenced laser excitation (red curve) and shutter opening (green box). A representative emission signal from the AlphaLISA (yellow curve) is also plotted for comparison. Note that laser excitation time was 0.5 sec and shutter opening time was 1 sec. The time gap between laser excitation and shutter opening was 20 msec.

4.2.6 Immunophenotyping Assay Protocol

The overall immunophenotyping assay protocol using the MIPA device is shown in Figure 4-4. First, a 10 µL cell solution with various THP-1 cell concentrations was loaded into the MIPA device by a syringe pump (Figure 4-4a). After the cells were uniformly seeded on the PMM, 2 µL LPS (L5886, Sigma) solutions of different concentrations (10, 50, and 100 ng/mL) were loaded into the MIPA device from the inlet of the cell culture chamber using pipette tips (Figure 4-4b). After LPS loading, two pipette tips were inserted into the inlets of both the cell culture and immunoassay chambers to prevent evaporation and provide a shear stress free microenvironment for cell stimulation. The MIPA device was incubated with the cells stimulated with LPS at 37°C and 5% CO_2 for 2 hr. Then, the pipette tip inserted into the inlet of the immunoassay chamber was replaced by another pipette tip filled with 2 µL AlphaLISA

acceptor beads (10 μg/mL) mixed with 2 μL of 10 nM biotinylated TNF-α antibody. AlphaLISA acceptor beads in the MIPA device were incubated with the cells at 37°C and 5% CO_2 for 1 hr, before another pipette tip filled with 2 μL AlphaLISA streptavidin-coated donor beads (400 μg/mL) was loaded into the inlet of the immunoassay chamber. The whole MIPA setup was incubated at 37°C and 5% CO_2 for another 30 min (Figure 4-4c). During the whole 1.5 hr bead incubation period, TNF-α secreted by LPS-stimulated THP-1 cells would diffuse from the top cell culture chamber through the PMM into the bottom immunoassay chamber to conjugate with antibody-coated donor and acceptor beads. After bead incubation, the MIPA device was placed into the customized optical setup for AlphaLISA signal detection.

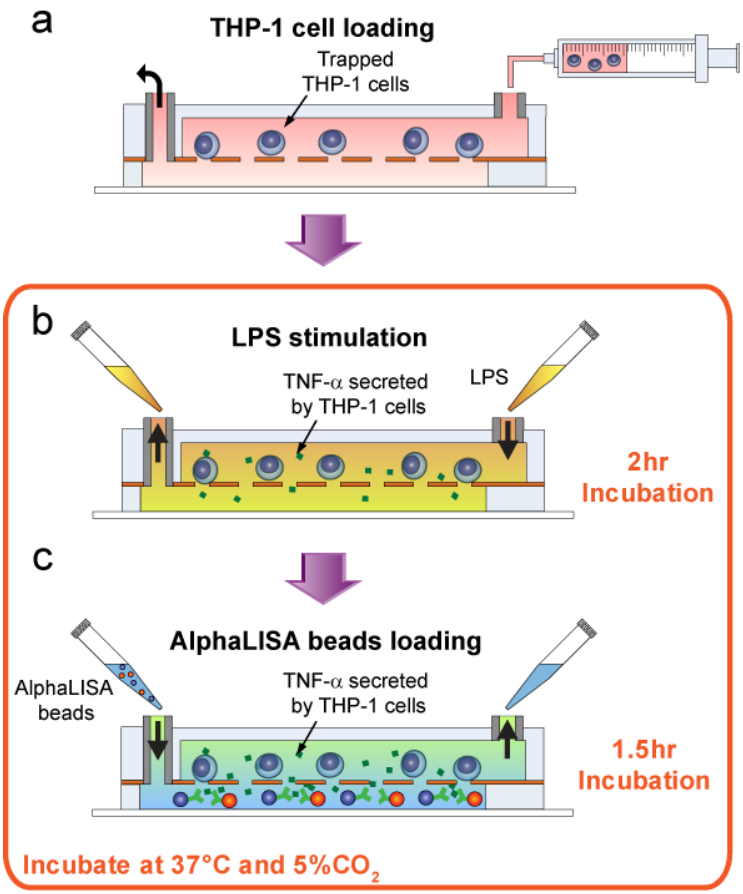

Figure 4-4 Immunophenotyping assay loading protocol. (a) THP-1 cells loading from the inlet of cell culture chamber. (b) Various LPS concentration (100, 50 and 10 ng/mL) loading from the inlet of cell culture chamber. (c) AlphaLISA bead loading from the inlet of immunoassay chamber. The MIPA device was incubated in the incubator at 37°C and 5% CO2 during (b) and (c). Two pipette tips were attached on both inlets to prevent evaporation and provide a shear stress free microenvironment for cell stimulation and analyte diffusion.

4.2.7 Cell Enumeration Analysis

Before seeding cells on the PMM, the MIPA device was filled with 2% (*w*/*w*) Pluronics F127 (P2443-250G, Sigma) in PBS to remove air bubbles trapped in device. The MIPA device was flushed twice with PBS, followed by loading a fresh cell growth medium. THP-1 cells were then seeded into the MIPA device in the complete cell medium using a syringe infusion pump (World Precision Instruments) at a flow rate of 5

μL/min. Cell seeding was monitored under an inverted microscope (Nikon Eclipse Ti-S, Nikon) equipped with an electron multiplying charge-coupled device (EMCCD) camera (Photometrics). Sequential brightfield and fluorescent images were taken using 10× (Ph1 ADL, numerical aperture or N.A. = 0.25, Nikon) and 20× (CFI Plan Fluor ELWD, N.A. = 0.45, Nikon) objectives. A 130 W mercury lamp (Intensilight C-HGFIE, Nikon) was used for fluorescent illumination. To examine cell seeding uniformity, the whole PMM area was scanned on a motorized stage (ProScan III, Prior Scientific). The images obtained from scanning were stitched using microscopic analysis software (NIS-Element BR, Nikon). To count viable and dead cells, recorded FITC-Texas Red fluorescent images were processed using NIS-Element BR software. Specifically, the threshold function was applied to optimize image contrast. Then, the Canny edge detection method was used to identify cell boundary, after which certain measurement criterions including cell area (100 - 500 μm^2) and circularity (0.5 - 1.0) were applied to identify THP-1 cells isolated on PMM and perform cell counting.

4.3 Results and Discussions

4.3.1 Cell Seeding Performance

We characterized the cell seeding performance of the MIPA device for on-chip isolation and enrichment of THP-1 cells. THP-1 cells of 10-30 μm in diameter were loaded into the MIPA device in the complete cell medium at three different concentrations of 1×10^5, 5×10^5, 1×10^6 cells/mL under a flow rate of 5 μL/min. Figure 4-5a&b show a photograph of the MIPA device (The device dimension is 9 mm L

× 7 mm W × 4 mm H.) and a SEM image of the PMM. Figure 4-5c represents a temporal sequence of false-colored brightfield images showing isolation and enrichment of THP-1 cells on the PMM. Using these brightfield images, we quantified the cell seeding density on the PMM as a function of the sample loading volume (Figure 4-5d). Our results in Figure 4-5 demonstrate that we could conveniently control the total number of THP-1 cells trapped on the PMM by modulating the sample injection time, necessary for normalizing the amount of TNF-α secreted by single THP-1 cells.

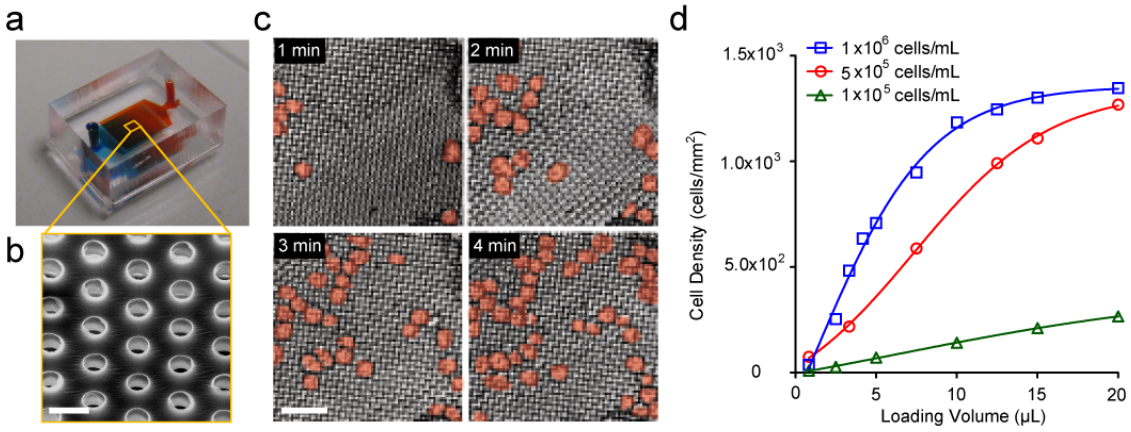

Figure 4-5 Isolation and enrichment of THP-1 cells using the MIPA device (a) A photograph of the MIPA device. The MIPA device was injected with dyed solutions for visualization of the cell culture chamber and the immunoassay chamber. (b) SEM image showing the PMM. Scale bar, 10 µm. (c) Temporal sequence of false-colored brightfield images showing isolation and enrichment of THP-1 cells on the PMM. The cell loading concentration was 5 × 105 cells/mL at 5 µL/min flow rate. Scale bar, 100 µm. (d) Plot of density of trapped cells on the PMM as a function of injection volume, using three different cell loading concentrations as indicated.

Under optical microscopy, the top surface of the PMM as well as the immunoassay chamber could be monitored in real time during cell loading by vertically changing the focal plane of the microscope (Figure 4-6b). During the cell loading process, no cell was observed in the immunoassay chamber as well as at the outlet of the MIPA device, suggesting no cell could pass through the PMM and all the cells were captured and retained on the PMM. We confirmed the cell capture efficiency of the PMM for THP-1

cells by comparing the number of captured cells on the PMM to the number of cells injected into the MIPA device. Our results suggested a nearly 100% capture efficiency of the PMM for THP-1 cells.

We further examined the cell seeding uniformity by taking fluorescence images across the whole PMM area for Calcein AM-labeled THP-1 cells. In this experiment, the MIPA device was loaded with a cell solution with the cell concentration of 5×10^5 cells/mL and the flow rate of 10 µL/min for 3 min. The cell density at three different locations uniformly distributed on the PMM was calculated and compared. Our result showed that the cell density at these different locations on the PMM were in the range of 1.20×10^3 - 1.32×10^3 cells/mm^2 with a variation of 3 - 5% (Figure 4-6c), suggesting a good cell seeding uniformity for THP-1 cells on the PMM in the MIPA device.

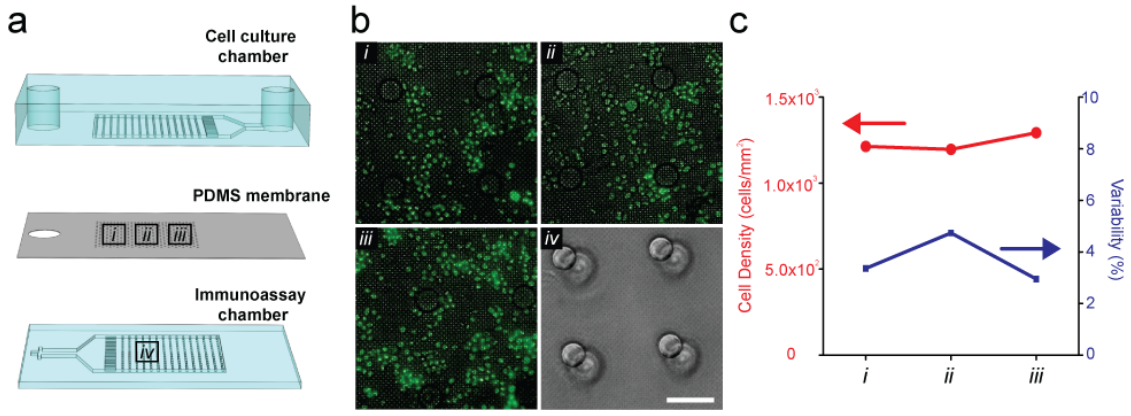

Figure 4-6 Cell seeding and uniformity in the MIPA device (a) The schematic of three layer MIPA device. The dotted area is the focus area of objectives. (b) Optical images of THP-1 cells distribution in four different position of device. The optical images in (1)-(3) were taken above the PMM. The optical image in (4) was taken below the PMM. Scale bars, 100µm. No cells were observed in the bottom layer of device, which means high capture efficiency of PMM. (c) Plot of cell density and variability to the average cell density in three positions of device.

4.3.2 Cell Viability Test

We next verified cell viability of THP-1 cells under various levels of LPS stimulations. We loaded a 10 μL cell solution with the THP-1 cells concentration of 5 × 10^5 cells/mL into the MIPA device. The cells were stimulated and incubated with different concentrations of LPS (10, 50, 100 ng/mL) for 2 hr. THP-1 cells were then stained using the cell LIVE/DEAD® Viability/Cytotoxicity Kit. The cell viability rate after LPS stimulations was as high as 90 - 92%, regardless of the LPS concentration (Figure 4-7b). Compared to 96% viability rate in the control group without LPS stimulation, we concluded that our cell capture procedure using the PMM and the subsequent LPS stimulation had a minimum effect on viability of THP-1 cells.

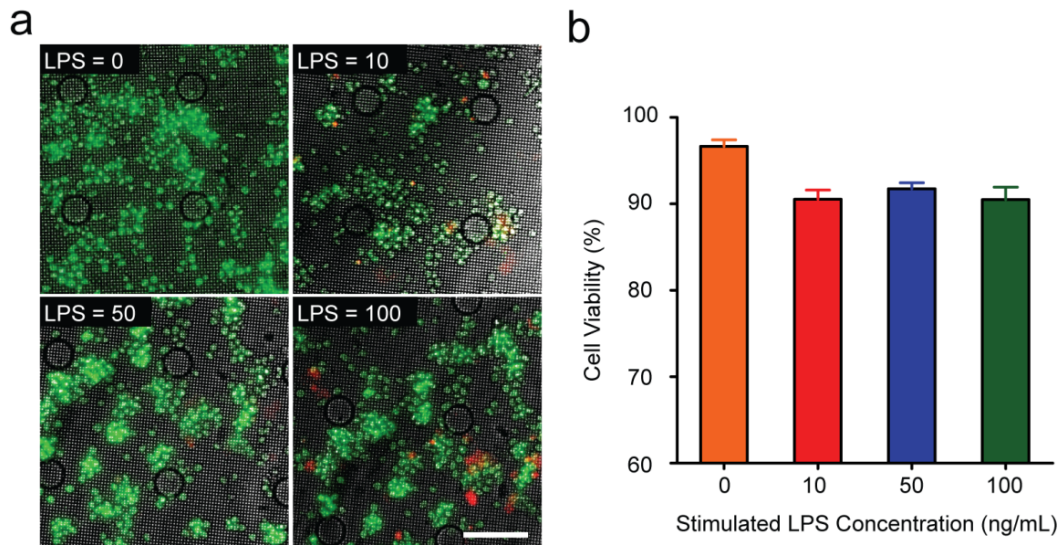

Figure 4-7 Cell viability (a) Optical images of THP-1 cells distribution and corresponded live/dead cell image on PMM after 2 hr 0, 10, 50, 100ng/mL LPS stimulation. The picture is merged from brightfield, FITC and TexasRed image by the microscopic analysis software (Nikon NIS-Element BR, Nikon). Scale bars, 100μm. (b) Plot of the cell viability under different LPS concentration stimulation.

4.3.3 Effect of Cell Population and LPS Concentration on Cytokine Secretion

After validating the minimal cytotoxic effect of our immunophenotyping protocol on THP-1 cell viability, we systematically quantified the levels of TNF-α secreted by THP-1 cells as a function of the total cell population trapped on the PMM (n = 1,000, 5,000, and 20,000 cells) and the LPS concentration (10, 50, 100 ng/mL). The AlphaLISA signal detected using the optical system was converted to the TNF-α concentration using a TNF-α standard curve (Figure 4-8a) generated using AlphaLISA with samples spiked with known concentrations of TNF-α. This TNF-α standard curve provided a correlation between the TNF-α concentration in the MIPA device and the corresponding AlphaLISA signal intensity. We further compared this result with the TNF-α standard curve by ELISA using a commercial plate reader (SpectraMax M2e, Molecular Devices). The two curves showed comparable results (Figure 4-8a), suggesting AlphaLISA indeed suitable for detection of TNF-α secreted from stimulated immune cells. The limit of detection (LOD), which is defined as 3 times the standard deviation of the blank (without spiked analyte condition) was 75 pg/mL and 10 pg/mL with our AlphaLISA method and the ELISA method, respectively, which are on the same order of magnitude.

We also used two commercial plate readers to compare, side by side, the ELISA (done by SpectraMax M2e, Molecular Devices) and AlphaLISA (done by PHERAstar MicroPlate Reader, BMG) signals from 20,000 THP-1 cells stimulated at various LPS concentrations (Figure 4-8b). The result also showed a highly linear correlation (R^2 = 0.9889) between ELISA and AlphaLISA technique.

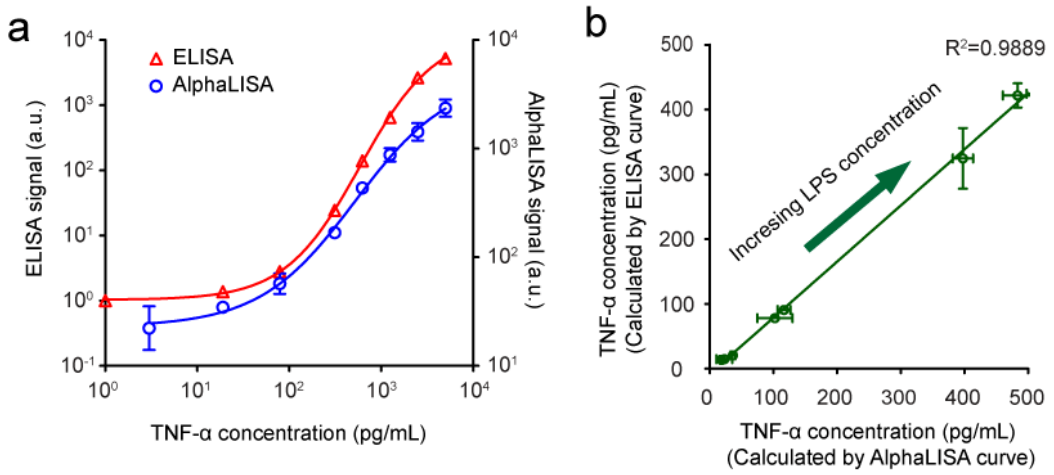

Figure 4-8 Comparison between AlphaLISA and ELISA signals (a) Standard curves for TNF-α detection by AlphaLISA and ELISA. A TNF-α solution at a known concentration (0 – 5,000 pg/mL) was first spiked into a complete cell growth medium. Subsequently, TNF-α in the cell growth medium was detected by AlphaLISA using our customized optical setup and by ELISA using a commercial plate reader (SpectraMax M2e, Molecular Devices). (b) Correlation plot of ELISA and AlphaLISA signals for TNF-α secreted by 20,000 THP-1 cells as a function of LPS concentration (0-100ng/mL).

Figure 4-9b plotted the TNF-α concentration secreted by THP-1 cells as a function of the total cell population and the LPS concentration. Our result demonstrated that as expected, the concentration of TNF-α secreted by THP-1 cells increased according to both the cell number and the LPS concentration. When the LPS concentration increased from 10 to 100 ng/mL, the TNF-α concentration secreted by 1,000, 5,000 and 20,000 THP-1 cells increased from 53 to 80 pg/mL, 67 to 123 pg/mL and 150 to 528 pg/mL, respectively. With the LPS concentration of 100 ng/mL, the AlphaLISA signal-to-noise ratio was 6.97, 10.85 and 46.41 with 1,000, 5,000 and 20,000 THP-1 cells, respectively. For 1,000 THP-1 cells treated with 10 ng/mL LPS, the AlphaLISA signal was detected to be 2-fold greater than that for control samples generated by loading 10 ng/mL LPS in the MIPA without any THP-1 cells trapped on the PMM. The sensitive optical signal detection used in our study was susceptible to external noise likely coming from the

environmental background noise or the electronic noise of the PMT detector (e.g. dark current), which set up the lower limit for the detection sensitivity of our measurements.

Figure 4-9c&d plotted the average amount of TNF-α secreted by single THP-1 cells as a function of LPS concentrations (Figure 4-9c) or the amount of LPS molecules available to single THP-1 cells (Figure 4-9d). As shown in Fig. 4c, the amount of TNF-α secreted by single THP-1 cells appeared to increase as the cell number decreased. More interestingly, as shown in Fig. 4d, the amount of TNF-α secreted by single THP-1 cells for different cell densities (n = 1,000, 5,000, and 20,000) collapsed and followed a single linear positive trend with the amount of LPS molecules available to single THP-1 cells, suggesting that TNF-α secretion process by single THP-1 cells might be dictated by the available LPS molecules independent of the cell population size.

Finally, we compared the levels of TNF-α secretion between normal and deactivated THP-1 cells that were both stimulated with LPS. Identifying deactivation of monoctyes (also termed as immunoparalysis) can provide an effective means to predict health risks such as development of infectious complications [45, 47, 48, 50]. It is believed that real-time phenotypic identification of patients with immunoparalysis could be used to guide alternative care strategies, such as immune stimulation [48]. To examine whether the MIPA device could distinguish normal THP-1 cells vs. immunoparalyzed immune cells, THP-1 cells were first treated with the complete cell growth medium supplemented with 10 ng/mL LPS for 24 hr to deactivate them and attenuate the secretion of cytokines, including TNF-α, in response to a second stimulation with LPS [101]. Deactivated THP-1 cells were then loaded into the MIPA device for TNF-α secretion measurements. Figure 4-9e compared TNF-α concentrations secreted by normal and deactivated THP-1

cells trapped on the PMM for n = 20,000 cells. Consistent with prior in vitro models, TNF-α secretion by deactivated THP-1 cells was 2-4 times less than those of normal THP-1 cells, especially when LPS concentration was greater than 50 ng/mL. More interestingly, deactivated THP-1 cells appeared to be not sensitive to changes of LPS concentration as compared to normal THP-1 cells, as concentrations of the TNF-α secreted by deactivated THP-1 cells remained roughly constant (105 ± 12 pg/mL) as the LPS concentration increased from 10 to 100 ng/mL. In distinct contrast, concentrations of TNF-α secreted by normal THP-1 cells increased from 150 to 528 pg/mL with the LPS concentration increasing from 10 to 100 ng/mL.

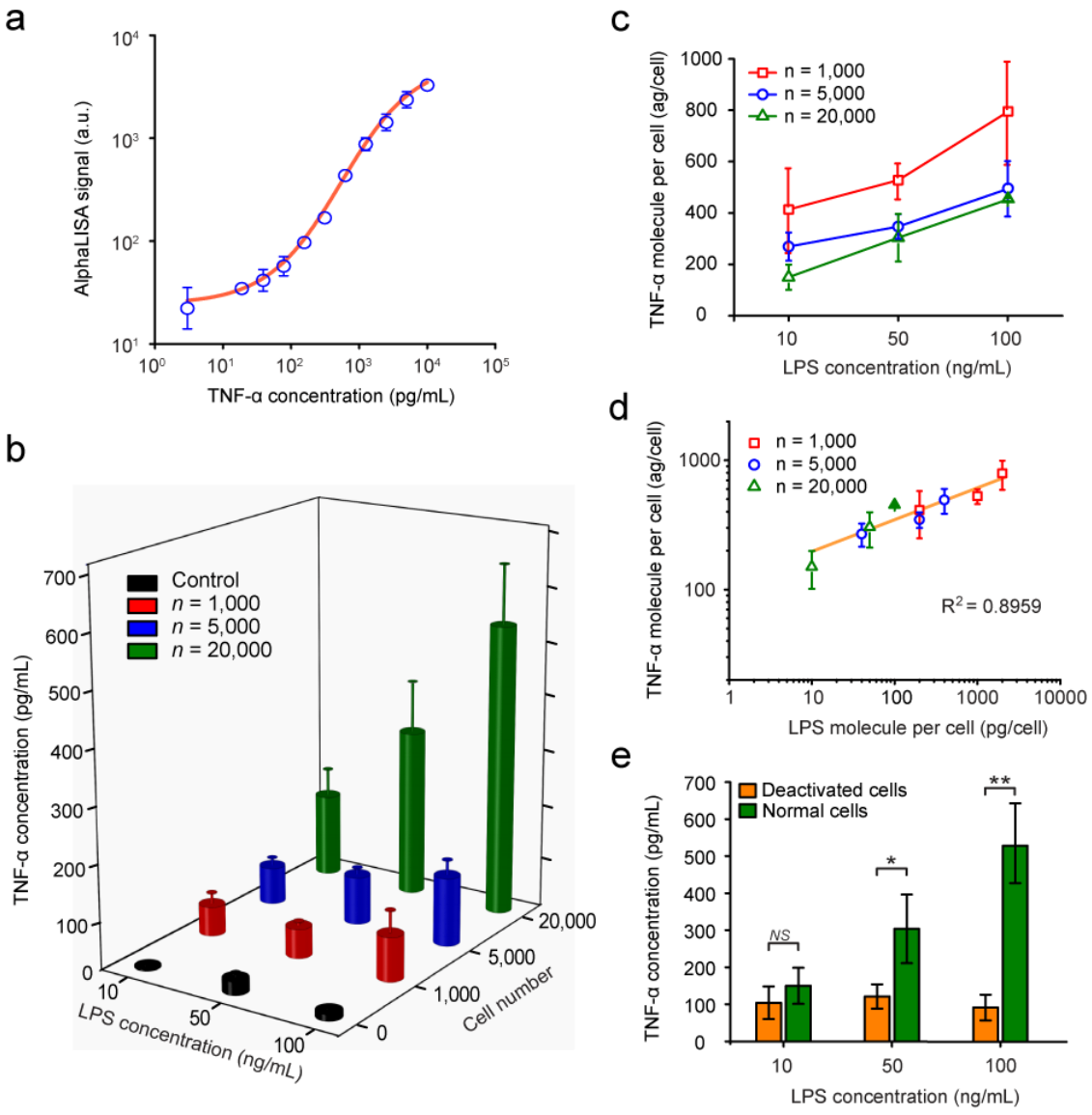

Figure 4-9 Detection of TNF-α secreted from LPS-stimulated THP-1 cells using the MIPA device (a) Standard curve for TNF-α detection. TNF-α with a known concentration (0 – 10,000 pg/mL) was spiked in the complete cell growth medium and detected using AlphaLISA and the customized optical setup. (b) Plot of TNF-α concentration secreted by LPS-stimulated THP-1 cells as a function of cell number and LPS concentration. (c&d) Plots of average TNF-α concentration secreted by individual cells as a function of LPS concentration (c) or LPS concentration per cell (d). (e) Plot of TNF-α concentration secreted by normal and LPS-deactivated THP-1 cells trapped on the PMM (n = 20,000 cells). P-values calculated using the paired student's t-test are indicated for significant differences ($P < 0.05$ (*) and $P < 0.005$ (**)). *NS*, statistically not significant.

Chapter 5

Conclusions and Future Work

5.1 Summary of Thesis

This thesis work successfully developed two optofluidic platforms and demonstrated their unique advantages in cellular phenotyping. In our microfluidic multispectral flow cytometry study, we achieved high-speed discrimination of multiple cell types based on the spectrum profiles of fluorescent proteins or surface biomarkers at the single cell level with a microfluidic flow cytometer device. In our microfluidic immunophenotyping assay device study, we demonstrated the identification of cellular immune functions using an optofluidic device that enables on-chip cell trapping, cell stimulation and *in-situ* cellular cytokine secretion measurement with shorter incubation time and less sample volume. A summary of all the presented achievements are given in the following sections.

5.1.1 Microfluidic Multispectral Flow Cytometry

The microfluidic multispectral flow cytometry (MMFC) represents a unique class of optofluidic system incorporating a MEMS-based tunable nanoimprinted grating

microdevice, a single excitation laser, and a single PMT detector. The system enables us to achieve *in-situ* continuous spectral profile detection for bioparticles flowing in a microfluidic channel with high specificity and high speed. Integrating our optofluidic system with other microfluidic components, we can develop a lab-on-a-chip system that enables multiplexed signal detection together with sample preparation/loading, agent mixing/reaction, cell culture, or programmable chemical stimulation on a single chip. Furthermore, systems identical with ours could be integrated with an array of microfluidic channels to perform massively parallel cell analysis with higher throughput and multiplicity on a single chip. The use of microspheres as platforms for surface binding assays and analyses in microfluidic channels results in a large surface-to-volume ratio, leading to the capacity to bind greater analyte molecules in a small volume [102-105]. Therefore, microsphere-based MMFC promises high assay sensitivity.

Of particular note is that our study demonstrates *in-situ* detection and discrimination of in-flow emission sources only with a 5nm peak-to-peak spectral difference and a significant intensity overlap at a confidence level as high as 85%. This capability is unique to our system and cannot be achieved by the optics of conventional flow cytometers, which only detect emission intensities with discrete wavelength bands. To further increase the signal-to-noise ratio for weak emission bioparticle detection, we can use the electronic shutter or chopper to modulate the excitation laser at 50-100 KHz. By applying the lock-in amplifier technique, the emission signal with fixed frequency can be sorted out from background noise. Our dynamic *in-situ* spectroscopy technique has potential to allow highly accurate quantification of protein binding, intracellular Ca2+ concentration, pH, and temperature in a flow cytometry setting based on subtle variations

in the emission spectral profiles of probe fluorophores as well as from their intensity variations [106-108]. Particularly for fluorescent proteins, our system could substantially improve the ability to discriminate among cell populations with different protein combinations, such as CFP/GFP and GFP/YFP that cannot be separated by standard flow cytometry. This will, for example, allow researchers to combine and identify more cell types in genetically engineered mice. Our system could also provide new means to analyze structural and functional heterogeneities of cells to obtain information useful for disease diagnosis/prediction and drug discovery in microfluidic environments.

5.1.2 Microfluidic Immunophenotyping Assay Device

The microfluidic immunophenotyping assay (MIPA) device developed in this study demonstrated four important features for cellular phenotyping. First, the PMM integrated in the MIPA device enabled high-efficiency and uniform cell trapping/seeding with a cell population accurately adjustable by modulating the sample injection volume. Second, the MIPA device required a significantly reduced amount of sample volume (or cell population) as compared to conventional whole blood assays. The miniaturized microfluidic environment of the MIPA device permitted a spatial confinement of stimulated cells and their secreted cytokines, yielding significantly improved detection sensitivity with a much smaller cell population. More specifically, our assay using the MIPA device allowed reliable signal measurements with a signal-to-noise ratio of 2.2 for only 1,000 THP-1 cells while conventional cell-stimulation assay typically requires 2×10^4 cells with whole human blood of 50μL containing monocyte cells at a concentration of 4×10^5 cells/mL [109]. Thus, immunophenotyping of human monocytes using the

MIPA device would only require whole blood of ~2.5 μL with the 20-fold cell number reduction. The detection sensitivity of the MIPA device could be further heightened by using smaller cell culture and immunoassay chambers.

Third, the MIPA device coupled with the optical detection system permitted cell stimulation assays and quantifications of cytokine secretions operated in the same microfluidic platform. Cytokine secretion from LPS-stimulated THP-1 cells could be quantified without any cell flushing, analyte dilution, cellular condition alterations, or potential human contaminations. Most importantly, stimulated THP-1 cells could remain alive after immunophenotyping with the MIPA device, permitting downstream cellular analysis that would require live cells. Such analysis includes, for example, identification and enumeration of subpopulations of immune cells captured on the PMM by labeling with a specific biomarker (e.g. CD14 for monocytes).

Fourth, by reducing the reagent diffusion distance and eliminating the need for multiple reagents loading, blocking, and washing steps, our immunophenotyping method could limit the LPS stimulation time to 2 hr and the total assay time to 3.5 hr. In contrast, conventional ELISA-based cell-stimulation assay would require a much longer assay time of > 8 – 24 hr. Previous studies [110, 111] based on microfluidics-based cellular immunophenotyping devices usually used heterogeneous immunoassay techniques (*e.g.*, ELISA/ELISpot) and thus required a substantially longer assay time due to multiple surface immobilization processes and washing steps. For patients exhibiting acute immune responses, a rapid and accurate evaluation of their immune status is highly critical. Our cellular immunophenotyping assay with the MIPA device holds significant promise to open ways for rapid immune status determination in real clinical settings.

5.2 Future Research and Applications

The continuous work on optofluidic platforms for cellular phenotyping will have a prominent impact on several research fields. The future work of microfluidic multispectral flow cytometry includes integrating the excitation component and the nanoimprinted grating with microfluidic channel for minimum optical alignment and optical signal loss. This compact device could be potentially used for POC diagnosis. Another direction is to integrate the nanoimprinted grating with confocal microendoscopy for in-vivo multispectral imaging. For microfluidic immunophenotyping assay device, the future work will move towards (1) optimizing the PMM to isolate immune cell subpopulations and monitoring their immunofunctions, and (2) designing microvalves embedded microfluidic device for multiplex cytokine detection in collaboration with Fu lab at the University of Michigan. The controlled microenvironment incorporating microvalves will accurately quantify the cell secreted cytokine concentration, precisely control assay volume, and potentially perform single cell trapping and phenotyping. The detailed future work is described in the following sections.

5.2.1 Point-of-Care HIV/AIDS Diagnosis

Human immunodeficiency virus (HIV) infection / acquired immumunodeficiency syndrome (AIDS) is a human immune disease cause by human immunodeficiency virus. It is one of the most destructive pandemics in the world, causing more than 1.8 million deaths per year. Currently, the major HIV diagnosis method is called the “antibody test.” In this test, HIV antigens are used to capture HIV antibodies in the person’s serum.

However, most HIV patients will not develop a detectable antibody level until 30 days after infection. Another simpler yet less accurate diagnosis method is WBC count test, specifically counting the CD4+ T-cell number. CD4+ T-cell is the major leukocyte attacked by HIV, and its cell number typically drops below 200 cells/μL when the HIV infection occurs. Despite the above well-established diagnosis methods, performing either antibody test or WBC count by flow cytometry usually requires sophisticated, expensive instruments and highly skilled operators. However, most patients who suffer from HIV usually live in developing countries with limited resources. Therefore, I propose to further develop a microfluidic multispectral flow cytometry with fully integrated optics to make the POC HIV diagnosis more accessible. The full integration will eliminate laborious optical alignment and achieve great ease at which the device is operated.

The proposed sample preparation protocol of isolating CD4+ and CD8+ T-cells in the whole blood is shown in Figure 5-1a. Two-color fluorescent beads conjugated CD4 and CD8 surface biomarkers will be mixed with patient blood sample. Once CD4+/CD8+ T-cells are captured by the beads, blood sample will be introduced into the microfluidic channel for *in-situ* T-cell counting. As shown in Figure 5-1b, the microfluidic flow cytometry will integrate (1) an embedded optical fiber to connect excitation light source (e.g. LED or laser diode), and (2) focusing lens and nanoimprinted grating to collect emission signal. The embedded optical fiber, lens and nanoimprinted grating together enable fluorescence excitation and detection with a highly focused interrogation zone (Figure 5-1c) with minimum optical alignment. Besides, this fully eliminates light scattering from the edges of the channel, thereby significantly improving

the signal-to-noise ratio of the measurement. Compared to the existing HIV diagnosis microfluidic system by single-color CCD imaging-based CD4+ T-cell counting [112], this system with multispectral detection capability allows for simultaneous counting of two-color labeled CD4+ and CD8+ T-cells, which can improve the diagnosis accuracy. In the future, the system can also implement the cell sorting function by attaching a micro-electromagnetic module to separate two-color bead-conjugated CD4+ and CD8+ T-cells for downstream analysis.

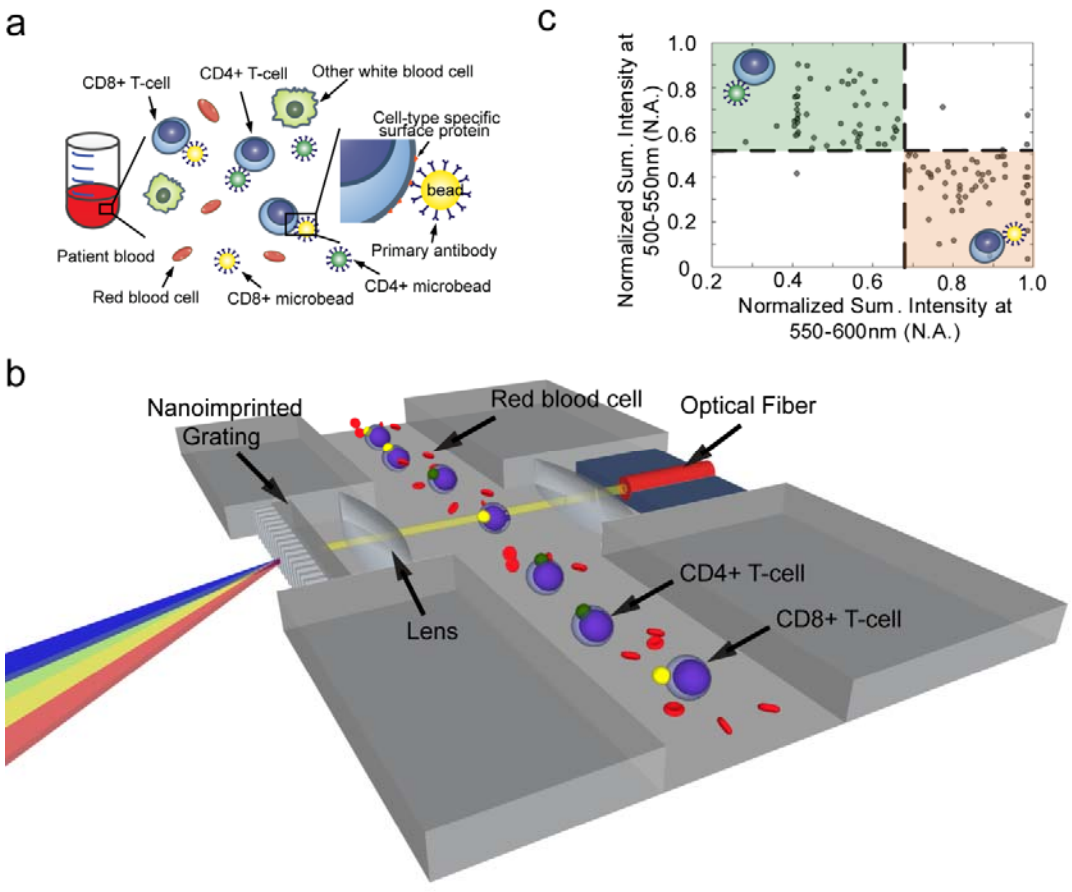

Figure 5-1 Schematic of integrated optofluidic flow cytometry. (a) The sample preparation protocol. (b) The detailed optical components integrating into microfluidic flow cytometry. The CD4+/CD8+ bead-conjugated T-cells flow in the channel. (d) The 2D plot map of CD4+ and CD8+ cell along the normalized integrated intensity in two wavelength bands.

5.2.2 Multispectral Confocal Microendoscope

In this thesis, we developed a microfluidic multispectral flow cytometry platform to demonstrate the unique performance of MEMS-actuated nanoimprinted grating. Another potential application of the grating component is to integrate it with MEMS-based confocal microendoscopy for in-vivo multispectral imaging. The multispectral detection can simultaneously locate multiple biomarkers in the same scanning area or provide detailed information of cellular-molecular interactions, which are also very important for cancer diagnosis. Figure 5-2 shows a proposed optical setup of nanoimprinted grating implemented with a confocal microendoscopy. In confocal microendoscopy setting, multiple biomolecules in the tissue are excited by single photon and emit fluorescent signals of various spectra. To achieve rapid multispectral imaging with three dimensional scanning, it is important to have a high-speed optical tunable filter to collect a spectral profile in various focal planes. Besides, the miniaturized size of the nanoimprinted grating is ideal to collect the emission signal from the small core diameter of a single mode fiber. The single mode fiber is the key component to reject out-of-focal plane scatter light in the confocal microendoscopy setting.

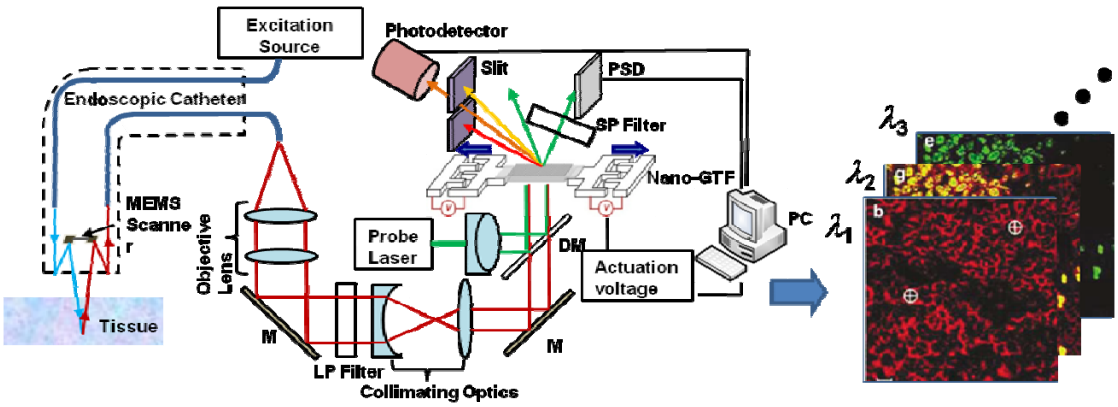

Figure 5-2 Schematic of a multispectral confocal microendoscopy system. An endoscope collects light from live tissue and directs the light towards the nanoimprinted grating, which can separate wavelength signals for spectral imaging.

5.2.3 Isolation and Immunophenotyping Subpopulation of Immune Cells

Although functional cellular immunity test is a promising method to establish the diagnosis of immune dysfunctions, the conventional functional cellular immunity test involves measurements of the capacity of *peripheral blood mononuclear cells* to produce pro-inflammatory cytokines when stimulated *ex vivo*. However, this 'bulk' assay measures the overall reactivity of a population of lymphocytes and monocytes, making it difficult to pinpoint the phenotype or real identity of the reactive immune cells involved. In order to get more accurate immunophenotyping information from subpopulation of immune cells in human blood, we can mix antibody-conjugated microbeads with patient sample. Immune cell subpopulations will be first captured by microbeads functionalized with capture antibodies against specific cell surface antigens and enlarge the total size. We can then optimize the through holes diameter of the PMM to be smaller than the size of the microbeads but larger than normal leukocytes. Owing to the increased size of cell-microbead conjugates, the desired subpopulation of immune cells will be isolated and retained on the PMM upon loading a blood sample, while other blood cells including undesired immune cells will be eluded through the PMM. On-chip functional immunophenotyping will then be performed to examine the capacity of these immune cells to produce inflammatory cytokines following stimulation.

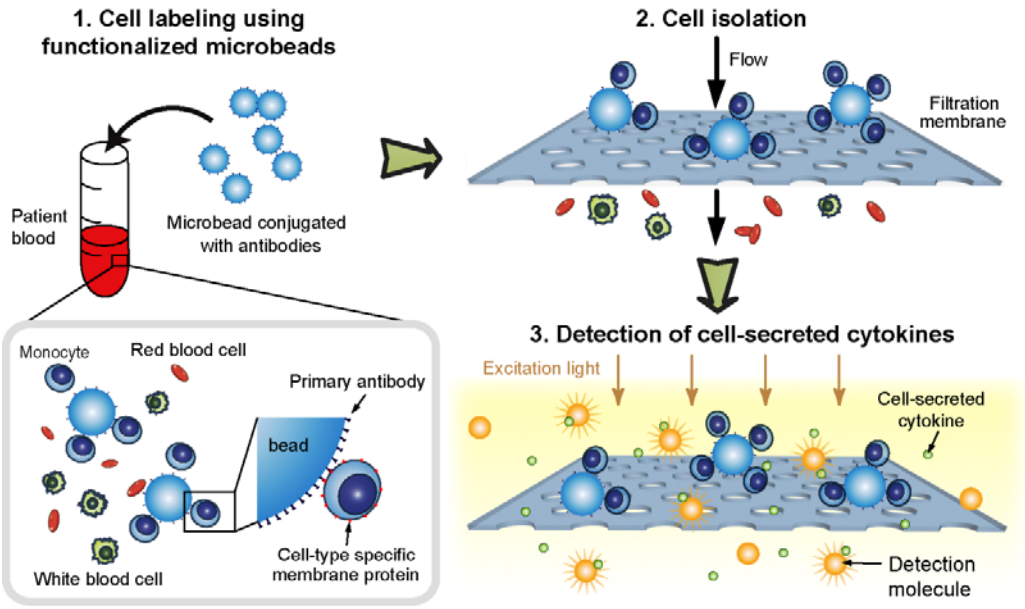

Figure 5-3 Schematic of isolation and immunophenotyping of immune cell subpopulations from human blood specimens.

5.2.4 Multiplex Cell-secreted Cytokine Detection

Another important direction of cellular immunophenotyping is to achieve multiplex cell-secreted cytokine detection. Continued progress in many fields ranging from fundamental biological to patient care critically hinges on the availability of specific, reliable assay systems capable of multiplex detection from a single sample [113-115]. Modern clinical treatments require techniques that can screen multiple protein biomarkers in order to accurately diagnose patients' diseased conditions. For example, some T-cells are polyfunctional, i.e., they secrete multiple cytokines, such as tumor necrosis factor-α (TNF- α) interferon-γ (IFN- γ), interleukin(IL)-6, IL-10, in response to extracellular stimulation and signaling. These cytokines are known to correlate with positive or negative disease outcomes [59]. Therefore, the quality of a polyfunctional T cell response is known to be a good indicator of clinical outcome [116, 117]. However,

quantitatively characterizing the highly heterogeneous, functional diversity of a single polyfunctional T-cell is very challenging due to the limitations of the standard ELISA or flow cytometry technique despite its promise to drastically advance clinical knowledge of many diseases. Yet, development of a reliable, multiplex biosensing technique permitting simultaneous detection of these cytokines is crucial to provide discriminating power for diagnostic methods based on immune cell function analysis.

To precisely introduce and confine the reagent volume for multiplexed cell-based cytokine detection, I propose to integrate a series of pneumatic-actuated microvalve into the microfluidic immunophenotyping assay (MIPA) device. Figure 5-4 shows the concept design of microvalve-controlled MIPA device. By selecting microbeads conjugated with different antibodies, we can monitor the immunophenotyping of individual immune cell subset (Figure 5-4a). Figure 5-4b shows the detailed device structure with a modified MIPA design. This new device will consist of two cell filtration chambers containing two PMMs with a large surface area and high porosity, where blood leukocytes or PBMCs will be isolated, enriched, enumerated, stimulated with LPS, and incubated. The device will have 4 microfluidic interconnect channels, each of them fluidically connecting to the main cell filtration chamber. For each microfluidic interconnect channels, there are three individual reaction chambers connected to the acceptor bead/antibody inlet channel and the donor bead inlet channel for detecting a particular cytokine species, which allow us to do either triplicate measurements at a single time point or single-sample measurement at various time points. After LPS stimulation and incubation, cytokines secreted by PBMCs will be delivered along each of the interconnect channels using microvalves integrated in the MIPA device.

The reagent loading (e.g. AlphaLISA beads), mixing, and conjugation will be accomplished sequentially by modulating the on/off states of integrated microvalves. The microvalves will be actuated using an external air pneumatic actuation controller connected to a LabVIEW software-installed personal computer. To sum up, the proposed microvalve-controlled MIPA device allows four technological advancements. First, the microvalve can precisely confine the reagent volume, which can minimize potential human dispensed assay volume variation. Second, the highly-automated liquid handling operation can also simplify sample loading process. Third, a series of reaction chambers in one single microfluidic device allows multi-parallel and high-throughput detection. Fourth, because the detection area can be extremely minimized, the analyte and assay beads can be further concentrated. It can shorten the assay incubation time and enhance the signal-to-noise ratio.

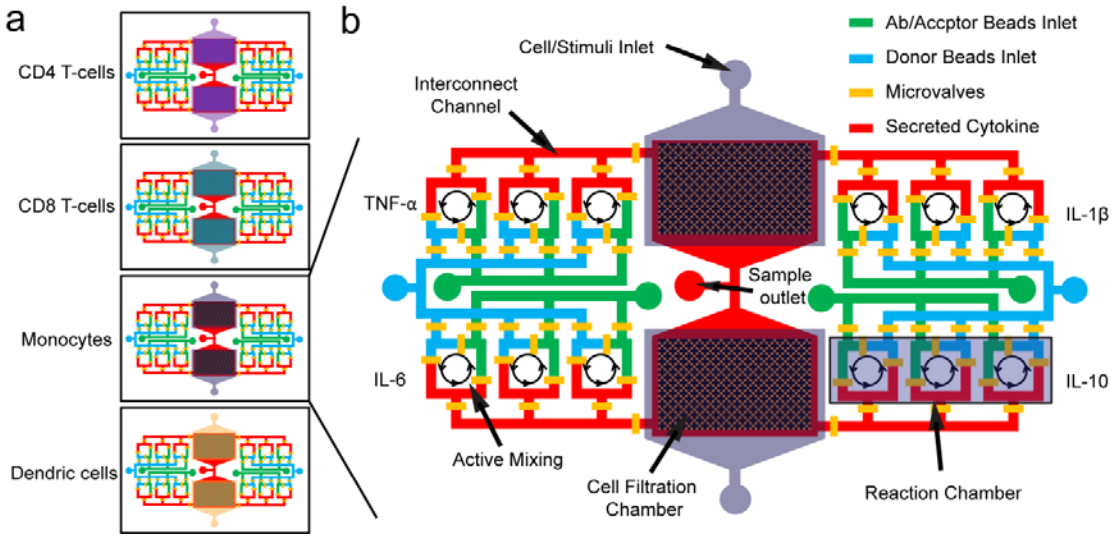

Figure 5-4 Schematic of microvalve-controlled microfluidic immunophenotyping assay (MIPA) device for multiplex cytokine detection. (a) Each microfluidic device unit is used for one subpopulation of immune cells. (b) The detailed device structure.

5.3 Outlooks

Over the last 20 years, the field of genomics – a discipline to determine and map the entire DNA sequences of living organisms – has seen explosive advances [118-122]. Scientists have obtained some insight into the mechanism of life through genomics. Modern life sciences still see further challenges towards translating the discoveries in genomics into a full understanding of genetically and environmentally affected human traits and disease developments. Statistical noise in genomic data often makes it difficult to elucidate the cause of underscore biological effects [11, 12]. Modern biology has come to recognize that heterogeneity in non-genetic cellular phenotypes is one of the key factors governing core processes that occur at the cellular level, including proliferation, stimulus response, carcinogenesis, and drug resistance. Many diseases, including cancer, originate in a single or a few cells showing abnormal phenotypes. Early detection of the onset of a cellular phenotype abnormality permits establishment of better disease diagnosis and treatment. Optofluidics is surely an exciting research field particularly during the current translational period of biological research. Optofluidics technology holds great promise to serve as a powerful tool to enable single cell-level phenotype characterization. We strongly believe that the importance of this field will be more pronounced than ever as cellular phenotyping research manifests its need for advanced optical detection tools.

Optofluidic systems realize efficient, fast, skill-free on-chip operations in manipulation and handling of individual cells and assay reagent loading while securing optical access to on-chip samples. Here, we propose to extend the definition of "optofluidics" to broader systems capable of advancing microfluidics with optics. Future

research can focus on advancing microfluidic cellular phenotyping techniques to the point that they become equipped with unprecedented levels of throughput [59, 72-76, 123]. Coupled with a massively parallel microfluidic single-cell manipulation platform, optical technologies leading to higher sensitivity, accuracy, and signal handling capability would generate a huge number of phenotype datasets and provide a higher degree of information. In the context of enabling cellular phenotyping assays, the effort to achieve monolithic optics-fluid integration unlikely finds a great value. Here, an emphasis should be placed in performing sophisticated fluidic actuation for sample loading, transporting, and sorting with highly sensitive, selective optical detection done by using off-chip optical instruments. Along with this direction, researchers also need to note that optofluidic technology has the great potential to integrate multiple optical detection modalities (e.g., fluorescence + SERS, fluorescence + SPR, fluorescence + interferometry) in a common microfluidic platform. Such a multi-modality detection approach may synergistically enable multi-parametric analyses with high sensitivity and specificity. Multi-parametric analysis devices are "must-have" tools for data-intensive genotype-phenotype mapping assays.

Of course, the research community can be directed towards another important direction, which focuses on developing fully integrated standalone micro-analytical devices for POC applications. We find a majority of the reviewed studies still requires the use of large, expensive, and sophisticated off-chip lasers, detectors, and spectrometers. As seen in semiconductor and microelectromechanical systems (MEMS) industry, system integration and packaging are a critically important research area to enable future mass production and commercialization. We expect to see this research

field evolving to provide innovative monolithic optics-fluid integration schemes. We expect that growth towards this research direction, evidenced by the recent demonstration of fluidic channel-on-a CCD detector chip [124-126], spectrometer-on-a-fluidic chip [127], and flow cytometer-on-a-cell phone [71] devices, will open ways for development of standalone cellular phenotyping microchips for global health care.

Appendix A

Microfluidic Flow Cytometer Fabrication

A.1 Microfluidic Channel Mold Fabrication

1. Silicon Wafer Clean
    Piranha Clean (H_2SO_4 : H_2O_2 = 1 : 1): 10 min
    BHF Dip: 1 min
    DI Water Rinse: 10 min
    Spin Rinse Dry
2. Dehydration Bake
    Bake on Hotplate: 120°C, 5 min
3. Photoresist Patterning – Microfluidic Cytometry Mask
    Photoresist: SU-8 2050, ~70 μm
    Spin: 500 rpm, 10 s + 2000 rpm, 30 s
    Soft Bake on Hotplate: 65°C, 3 min + 95°C, 9 min
    Cool Down in Ambient: >10 min
    Exposure (MA6 Mask Aligner): 20 s
    Post Exposure Bake on Hotplate: 65°C, 2 min + 95°C, 7 min
    Cool Down in Ambient: >10 min
    Development (SU-8 Developer): 7 min
    Visual Inspection, Develop Further if Needed
    IPA Rinse: 1 min
    Hard Bake on Hotplate: 65°C to 160°C + 160°C, 10 min + 160°C to 65°C

A.2 PDMS Channel Fabrication

1. PDMS Precursor Preparation
    PDMS Precursor Mixing: Sylgard 184 (Base : Curing Agent = 10 : 1)
    Degas in Desiccator: 30 min
2. PDMS Soft Lithography
    Place Wafer Containing Microfluidic Channel Mold in Petri Dish
    Pour PDMS Over Mold, ~4 mm thick
    Degas in Desiccator: 30 min
    Cure PDMS on Hotplate: 150°C, 10 min
    Cool Down in Ambient: >20 min
    Peel PDMS from Si Wafer and Mold
3. Inlets/Outlet Fabrication
    Cut Holes through PDMS Using Biopsy Punch, 1.5 mm

A.3 Microfluidic Channel Assembly

1. Pyrex Glass Wafer Clean (200 μm thick)
    Piranha Clean (H_2SO_4 : H_2O_2 = 1 : 1): 10 min
    DI Water Rinse: 10 min
    Spin Rinse Dry
2. Wafer Dicing
    Dicing with MA 1006 Dicing Saw: Blade 777
3. Channel Assembly from PDMS Mold and Glass Die
    Oxygen Plasma Surface Treatment in March Asher: O_2, 80W, 250 mT, 45 s
    Place PDMS Mold onto Glass Die with Channel Facing Down
    Apply Weight (~1 kg) to Assist Bonding: 30 min
    Remove Weight
    Spin: 500 rpm, 4 s + 4000 rpm, 30 s

Appendix B

Microfluidic Immunophenotyping Assay Device Fabrication

B.1 Microfluidic Channel Mold Fabrication

1. Silicon Wafer Clean

   Piranha Clean (H_2SO_4: H_2O_2 = 1: 1): 10 min

   BHF Dip: 1 min

   DI Water Rinse: 10 min

   Spin Rinse Dry

2. Dehydration Bake

   Bake on Hotplate: 120°C, 5 min

3. Photoresist Patterning – Microfluidic Immunophenotyping (top and bottom chamber)

   Mask Photoresist: SPR 220, ~3 μm using ACS 200 cluster tool

   Exposure (MA6 Mask Aligner): 30 s

   Post Exposure

   Development (SPR 220 Developer) using ACS 200 cluster tool

4. Etching of the chamber pattern

   Pattern of the mold for the chamber is etched using the deep reactive ion-etching (DRIE) (Deep Silicon Etcher, STS) (recipe- Pegasus 1; Etch rate- 5μm/min).

B.2 PDMS Microfilter Membrane Fabrication

1. Silicon Wafer Clean

    Piranha Clean (H_2SO_4: H_2O_2 = 1: 1): 10 min

    BHF Dip: 1 min

    DI Water Rinse: 10 min

    Spin Rinse Dry

2. Dehydration Bake

    Bake on Hotplate: 120°C, 5 min

3. Silanize the Silicon surface

    Silanize the Silicon surface using 500µm of Silane (tridecafluoro- 1, 1, 2, 2,-tetrahydrooctyl)-1-trichlorosilane vapour (United Chemical Technologies) for 1 hour under vacuum

4. PDMS Precursor Preparation

    PDMS Precursor Mixing: Sylgard 184 (Base: Curing Agent = 10: 1)

    Degas in Desiccator: 30 min

5. Spin coating of the PDMS layer

    Spin: 500 rpm, 10 s + 7000 rpm, 30 s

    Soft Bake on Hotplate: 90°C, 10 min

    Cool Down in Ambient: >10 min

    Bake in a furnace: Overnight, 60ºC

6. Photoresist Patterning – Microfluidic Immunophenotyping (membrane) Mask

    Oxygen Plasma Surface Treatment of PDMS layer in Plasma Cleaner PDC-001, Harrick Plasma: O_2, 80W, 250 mT, 5min

    Spin coat AZ 9260 (AZ Electronic Materials, Branchburg, NJ)

    Spin: 500 rpm, 10 s + 2000 rpm, 30 s

    Soft Bake on Hotplate: 90°C, 10 min

    Cool Down in Ambient: >10 min

    Exposure (MA6 Mask Aligner): 50 s

    Development (AZ 400K Developer): 2 min (Ratio of Developer: Water = 1:4)

    Visual Inspection, Develop Further if Needed

Hard Bake on Hotplate: 135°C for 5 min

7. Etching of PDMS

Silicon wafer is then processed with reactive ion etching (RIE; LAM 9400, Lam Research) using SF_6 and O_2 gas mixtures to transfer patterns from patterned photoresist to the underlying PDMS layer

B.3 Device Assembly

1. PDMS Precursor Preparation

PDMS Precursor Mixing: Sylgard 184 (Base: Curing Agent = 10: 1)

Degas in Desiccator: 30 min

2. PDMS Soft Lithography

Place Wafer Containing Microfluidic Channel Mold in Petri Dish

Pour PDMS over Mold, ~2 mm thick (bottom chamber) ~4 mm thick (top chamber)

Degas in Desiccator: 30 min

Cure PDMS in a furnace: 60°C, overnight

Cool Down in Ambient: >20 min

Peel PDMS from Si Wafer and Mold

3. Inlets Fabrication

Dice and separate the individual PDMS devices

Cut Holes through the top chamber PDMS Using Biopsy Punch, 0.75 mm

4. Bonding of the membrane

Oxygen Plasma Surface Treatment of PDMS layer (membrane and PDMS chamber (top) with microchannel facing upwards) in Plasma Cleaner PDC-001, Harrick Plasma: O_2, 80W, 250 mT, 2 min

Bonding: Bond the membrane and the top chamber (microchannels facing down) by gently applying some weight (~1 kg)

Remove weight

Keep in an oven at 110ºC for 5min

Cut the membrane boundaries using a scalpel and separate this assembly from the silicon wafer

5. Outlets Fabrication

In a symmetrically opposite end of the inlet, punch an outlet hole through PDMS Using Biopsy Punch, 0.75 mm

6. Bonding of the PDMS and glass slide

Oxygen Plasma Surface Treatment of PDMS layer (membrane and PDMS chamber (bottom) with microchannel facing upwards) in Plasma Cleaner PDC-001, Harrick Plasma: O_2, 80W, 250 mT, 45sec

Place PDMS Mold onto Glass Die with Channel Facing Up and apply some weight to assist bonding (~1 kg)

Remove weight

Keep in an oven at 110ºC for 5min

Appendix C

AlphaLISA Protocol

The protocol described below is for human TNF-α analyte standard curve in 384 well plate format (OptiPlate-384, PerkinElmer).

C.1 Analyte Standard Dilution

1. Preparation of 1X AlphaLISA Immunoassay Buffer:

   Add 2.5 mL of 10X AlphaLISA Immunoassay Buffer to 22.5 mL H_2O.

2. Preparation of human TNF-α analyte standard dilutions:

   Reconstitute lyophilized human TNF (0.1 μg) in 100 μL H_2O. The analyte is series diluted from 10,000 - 1 pg/mL

C.2 Assay Loading Protocol

1. Preparation of 2.5X AlphaLISA Anti-TNF Acceptor beads + Biotinylated Antibody Anti-TNF MIX (25 μg/mL /2.5 nM):

Add 50 µL of 5 mg/mL AlphaLISA Anti-TNF Acceptor beads and 50 µL of 500 nM Biotinylated Antibody Anti-TNF to 9,900 µL of 1X AlphaLISA Immunoassay Buffer. (Prepare just before use)

2. Preparation of 2X Streptavidin (SA) Donor beads (80 µg/mL):

   Keep the beads under subdued laboratory lighting. Add 200 µL of 5 mg/mL SA-Donor beads to 12,300 µL of 1X AlphaLISA Immunoassay Buffer.

3. Samples:

   If applicable, dilute samples to be tested in diluent (e.g. 1X AlphaLISA Immunoassay Buffer or cell culture medium)

4. In a 384-well microplate (total assay volume is 20 µL):
   1. Add 2 µL of each analyte standard dilution or 2 µL of sample
   2. Add 8 µL of a 2.5X MIX (freshly prepared): AlphaLISA Anti-Analyte Acceptor beads (10 µg/mL final) and Biotinylated Antibody Anti-Analyte (1 nM final). Incubate 60 minutes at 23˚C
   3. Add 10 µL of 2X SA-Donor beads (40 µg/mL final). Incubate 30 minutes at 23˚C in the dark
   4. Read using PHERAstar MicroPlate Reader (BMG)

Appendix D

ELISA Protocol

The general ELISA protocol can be divided into two parts:

D.1 Plate and Sample Preparation:

D.1.1 Primary Antibody Immobilization

To prepare the ELISA plate, we first prepare 100μL capture antibody, then immediately coat it on the 96-well microplate. We then seal the plate and incubate it overnight at 4°C.

D.1.2 Sample Pretreatment

For LPS-stimulated cell sample solution, we first dispense 500μL THP-1 cell solution of 2 x 10^5 cells/mL into the 48-well microplate. Then, we stimulate the THP-1 cell with 50μL LPS (10-100ng/mL) solution and incubate for 4 hours at 37°C.

D.1.3 Antibody Blocking

During the cell incubation, we take out the 96-well microplate to room temperature for 30min, then aspirate capture antibody solution and wash with wash buffer (0.05% Tween 20 in DPBS, pH 7.4). The process is repeated two times for a total of three washes. Complete removal of liquid at each step is essential for good performance. For last wash, we sit the wash buffer in wells for 1 minute. After the last wash, we remove any remaining wash buffer by aspirating or by inverting the plate and blotting it against clean paper towels. After that, we block plates by adding 300μL reagent diluent (1% BSA in PBS) to each well and incubate at room temperature on shaker for 1 hour. After the blocking step, we repeat the aspiration/wash steps for three times and incubate for 5 minutes for last wash. The plates are now ready for assay loading.

D.2 Assay Loading Protocol

D.2.1 Sample Loading

We first add 100μL LPS-stimulated THP-1 cell solution or standard TNF-α analyte (1-10000pg/mL, as a calibration curve) into the antibody-coated 96-well microplate. Then, we cover the plate with an adhesive strip and incubate 2 hours at room temperature on shaker, following by aspiration/wash steps for three times.

D.2.2 Detection Antibody Loading

We then add 100μL detection antibody to each well incubating 2 hours at room temperature on shaker, following by aspiration/wash steps for three times.

D.2.3 HRP/Substrate/Stop Solution Loading

In step 3, we add 100μL streptavidin-HRP to each well for 20 minutes incubation at room temperature. Then, we empty wells and wash five times with 200μL wash buffer. In step 4, we add 100μL substrate solution to each well and incubate for 20 minutes at room temperature. The reaction takes 8-10 minutes at room temperature. After that, we add 50μL stop solution (sulfuric or phosphoric acid) to each well and gently tap the plate to ensure thorough mixing. Because the substrate and stop solution are both light sensitive, the plate should avoid directly placing under the light.

D.2.4 ELISA Signal Reading

Finally, we use a microplate reader (SpectraMax M2e, Molecular Device) to determine the optical density (OD) of each sample well. The reading wavelength range is set at 450-570 nm. The final OD is the subtracted readings at 540 nm or 570 nm from the readings at 450 nm. This subtraction will correct optical imperfections of the 96-well microplate.

Appendix E

High-speed tuning of visible laser wavelength using a nanoimprinted grating

In this thesis work, we use a strain-tunable nanoimprinted elastomeric grating as the key components of high-speed spectroscopy to achieve continuous multispectral detection capabilities in the microfluidic flow cytometry setting. Based on the high-speed wavelength tuning capability, the nanoimprinted grating can also be used as a optical wavelength tunable filter of multiple excitation light sources. In this section, we report a microelectromechanical systems (MEMS) tunable optical filter incorporating strain-tunable nanoimprinted elastomeric grating with a pitch varied by 18%. This device enables tuning of optical fiber-guided laser wavelength between λ = 473 and 532 nm within 0.5 ms by mechanically modulating the pitch with a silicon micro actuator. We also demonstrate the use of the device for obtaining two-color images of live/dead-stained and green/red fluorescent protein expressing cells with the color intensity ratio varied by the actuator voltage applied. The small structure of the device integrated on a silicon chip may be used in portable systems for optical switching and spectroscopy.

The major content of this chapter is reproduced from our previous publish paper: "High-speed tuning of visible laser wavelength using a nanoimprinted grating optical tunable filter" in *Applied Physics Letter*, 2009 [128].

E.1 Concept

Laser wavelength tuning is an important operation for many optical instruments. It finds a wide variety of applications in fiber optical communication [129, 130], spectroscopy [131, 132] and photochemistry [133]. With recent advancements of multi-color fluorescence labeling techniques for biological studies [134, 135], a demand for the ability to tune laser wavelength in the visible band grows ever stronger. In fluorescence spectroscopy and imaging, laser wavelength tuning is often achieved using tunable optical filters, such as acousto-optical tunable filters (AOTFs) and liquid crystal tunable filters (LCTFs) [136]. However, the relatively large-volume structures of these filters make them undesirable for the use in optofluidic lab-on-a-chip settings and point-of-care (POC) portable module systems.

Several miniaturized silicon MEMS-based tunable gratings have been developed and demonstrated for high-speed wavelength tuning in the infrared band or in the visible band at reduced spectral resolution [137-139]. Towards the goal of MEMS-based high-resolution visible wavelength tuning, our previous study [43] developed a nanoimprinted polydimethylsiloxane (PDMS) elastic pitch-variable grating mechanically tuned by on-chip silicon comb drive electrostatic actuators. But the device's small pitch variation range of 2.5% resulting in narrow bandwidth tuning (15 nm at λ = 558 nm) limits its

practical use for biofluorescent applications that involve significant spectral shifts of light.

In this section, we demonstrate high-speed two-color laser switching using a polymer-on-silicon MEMS grating optical tunable filter (GOTF) device with a much larger pitch variation range. The GOTF device is fabricated using a method named the "multi-level soft lithographic lift-off and grafting (ML-SLLOG) [79, 80, 140]. The ML-SLLOG process involves (1) fabrication of comb drives on a silicon-on-insulator (SOI) wafer, (2) soft lithography and lift-off of a three-dimensional PDMS microstructure, and (3) grafting of the PDMS microstructure onto the SOI patterns based on micro-assembly assisted by surface tension at an air-water interface [80]. The surfaces of the PDMS and silicon structures are both activated by oxygen plasma treatment to promote their permanent bonding in step (3).

E.2 Methods and Materials

The tunable optical filter developed here is a PDMS-on-silicon hybrid MEMS device constructed using the design concept and fabrication technique in our previous study [44, 80]. Figure E-1a shows the optical image of a single grating device. The device consists of an optically transparent PDMS microbridge of 250 μm in length and 150 μm in width with a nanoimprinted grating surface feature of 700 nm in period. The detailed grating surface profile is shown in a SEM image (Figure E-1b). The PDMS microbridge is bonded to a suspended silicon shuttle mass with a series of comb electrodes while its one end is fixed onto a substrate. To achieve wavelength tuning operation, the laser is aligned to pass through the grating bridge, as shown in Figure E-1c. The device is designed to

yield a ~45um displacement to vary the diffraction angle of light at an optical wavelength bandwidth of 80nm. Our previous work [80] shows the plasma-treated PDMS-silicon bonding is strong enough to sustain a 40% strain ratio and can operate over 100 million stretch cycles. The comb-drive is designed to have a tilted folded-beam silicon springs and a series of tapered arrangements of electrode finger. This design can minimize the nonlinear effects on the springs and electrostatic instability coming along with large comb-drive motions. Figure E-1d shows a batch-fabricated array of 16 tunable grating optical filter devices on a 20mm × 20mm chip. The whole device is mounted on a carrier board by wire bonding, which would enable massively-parallel voltage-controlled wavelength tuning.

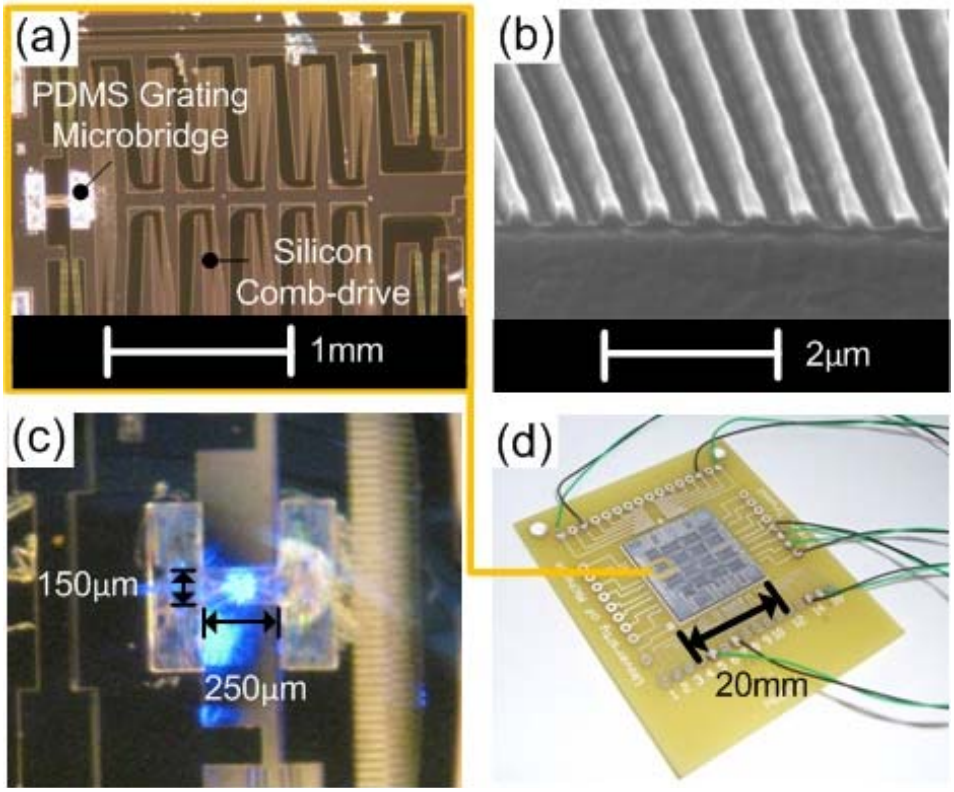

Figure E-1 Images of nanoimprinted grating optical tunable filter. (a) Optical image of single grating unit. (b) SEM image of 15 μm-thick PDMS microbridge with 700 nm nominal pitch. (c) Blue laser (λ = 473nm) passing through 250 μm × 150 μm grating bridge. (d) Whole 16 device array chip (20mm × 20mm) mounted to carrier board with wires.

Figure E-2a shows the working principle of the grating device. The wavelength tuning is performed by varying the PDMS grating pitch a with the silicon comb-drive actuated by a voltage signal. The incident light along with the z-direction is passing through the optical transparent grating in the x-y plane. The gating equation can be written as:

$$\lambda = a\,(sin\theta_1) \tag{E.1}$$

where λ is one incident light wavelength, a is the initial grating period and θ_1 is the first order diffraction angle of λ. When introducing a mechanical strain to elongate the spatial period of the grating to a', the wavelength of the first order diffraction at the same angle θ_1 will shift from λ to λ'. The corresponding mechanical strain ε can be defined as:

$$\varepsilon = \frac{a\prime - a}{a} = \frac{\lambda\prime - \lambda}{\lambda} \tag{E.2}$$

The relation between the wavelength shift $\lambda' - \lambda$ and the mechanical strain can be given by $\lambda' - \lambda = a\varepsilon \sin\theta_1 = \lambda\varepsilon$. From this relation, the wavelength shift of the first order diffraction at the angle θ_1 is linearly proportional to the mechanical strain introduced to the grating structure. At an actuation voltage of 180V, the grating strain level can increase up to 18%, which corresponds to a wavelength tuning range of 80nm in the visible wavelength band (Figure E-2b). Due to a stress-softening phenomenon in the elastic material, the grating strain increases rapidly in higher actuation voltage. The wavelength tuning is performed by varying the initial PDMS grating pitch a with the silicon comb drives driven by the actuation voltage V, (Figure E-2a). Here, the optical filtering is achieved by spatially blocking light other than the one diffracted to a targeted optical path. To demonstrate the wavelength tuning speed, spectral resolution and wavelength speed of the GOTF device, we implemented the device into an experimental

setup shown in Figure E-2c, where blue (λ=473nm) and green (λ=532nm) color laser lights (BWB-475-4E, B&W TEK and BWB-532-10E, B&W TEK, respectively) pass through the GOTF.

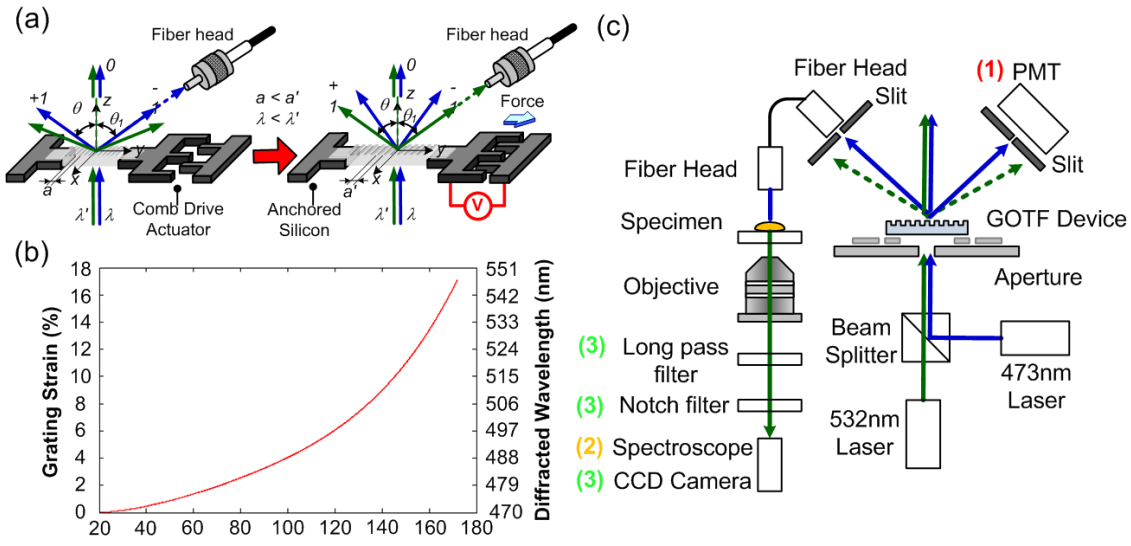

Figure E-2 Working principle of the grating device. (a) Device operation principle. The actuator is stretched by an actuation voltage. (b) Relationship between the comb-drive actuation voltage and the grating strain/diffracted wavelength. (c) The experimental setups incorporating the GOTF for (1) dynamic optical switching bandwidth measurement, (2) excitation spectrum measurement, and (3) live/dead PC3 cell two-color imaging.

E.3 Results

E.3.1 High-speed Wavelength Tuning Performance

To demonstrate high speed wavelength tuning capability of GOTF device, we apply a sinusoidal actuation voltage of 20-180V at 1kHz to the GOTF comb drives (Figure E-3a). A photomultiplier tube (PMT) (H8249-12, Hamamatsu Photonics) selectively captures a laser signal switched by the sinusoidal actuation voltage (Setup 1 in Figure E-2c). Figure E-3b shows strain introduced to the grating by the sinusoidal actuation voltage. It is

derived from the change in the first order diffraction angle θ measured for monochromatic incident light at λ = 532 nm using a position sensitive diode (C4674, Hamamatsu Photonics).

Figure E-3c shows a PMT signal with two peaks corresponding to the two-color laser light inputs at a wavelength tuning range of 460-540 nm. We obtain the spectral resolution of $\Delta\lambda$ = 4nm at 473nm and $\Delta\lambda$ = 8nm at 532nm from the full width half maximum (FWHM) of the signal. The result demonstrates the device's high-speed (1kHz) passband wavelength tuning capability.

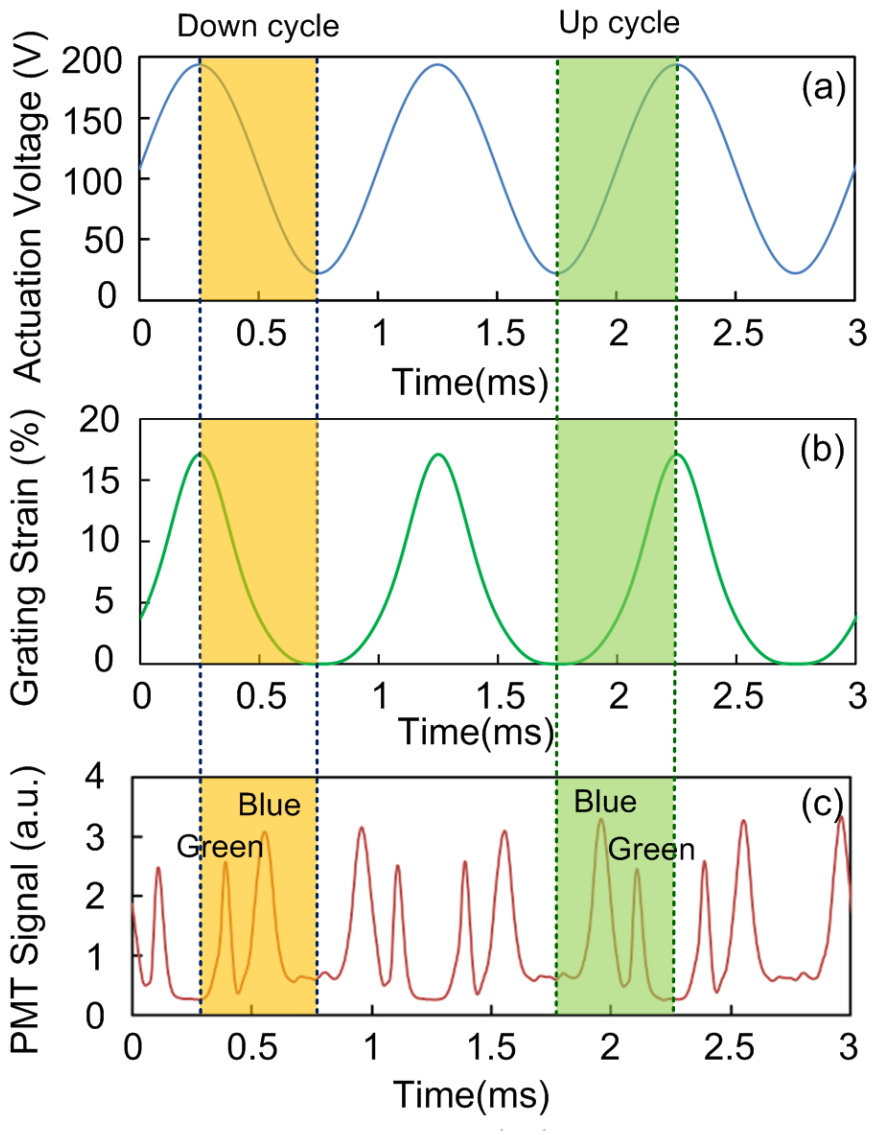

Figure E-3 Results for high-speed alternating laser excitation using the GOTF device. (a) Sinusoidal actuation voltage applied to the comb drives of the GOTF device. (b) Grating strain. (c) PMT signal.

E.3.2 Voltage Actuated Excitation Spectrum

Subsequently, we show that the GOTF can be operated in a fluorescent microscope (Nikon Eclipse TS100, Nikon Inc.) setting (Setup 2 in Figure E-2c). Here, an aperture of 1mm diameter is placed in front of the device before light beam reaches the grating to

eliminate excessive light and to reduce optical noise. A fiber with a 1000μm diameter core and NA = 0.22 (A57-746, Edmund Optics.) is used to capture the excitation light diffracted by the grating. Figure E-4a shows the excitation spectrum as a function of V, measured by the optical spectrometer (USB4000, Ocean Optics) coupled with a 10X objective lens (Setup 2 in Figure E-2c). At V = 20V, only the blue excitation is guided onto the specimen stage while green excitation is blocked. With V increased to 120V, the blue excitation intensity significantly drops more than 3 orders of magnitude after reaching the maximum value at V = 40V. At V = 150V, the green excitation intensity increased rapidly with the increasing voltage. At V = 175V, green excitation intensity reaches the maximum value with a signal-to-noise ratio nearly 4×10^3. Tuning the actuation voltage allows us to adjust the ratio between the blue and green excitation laser intensities in a programmable manner, which would be useful for dual-excitation ratiometric dye detection [141].

E.3.3 Two Color Fluorescent Imaging

Finally we demonstrate voltage-controlled modulation of the intensity ratio of two-color fluorescent emissions from a biological sample with the GOTF (Setup 3 in Figure E-2c). A 500nm long pass filter (S-003767, Chroma) and a 532nm notch filter (NF01-532U-25, Semrock) are used to eliminate the excitation lasers. Here, we use PC-3 prostate cancer cells maintained in complete media consisting of RPMI-1640 (61870; Gibco) supplemented with 10% (v/v) fetal bovine serum (FBS, 10082, Gibco), and 1% (v/v) antibiotic-antimycotic (15240, Invitrogen). The cells are stained by LIVE/DEAD Viability/Cytotoxicity Kit for mammalian cells (L-3224, Invitrogen). Calcein AM and

Ethidium homodimer-1 diluted in PBS to a final concentration of 1μM and 2μM, respectively, are added to the PC-3 cells and incubated for 30 min at 37^{o}C.

Figure E-4b-g constitute an image sequence that shows adjustable excitation of the stained cell by varying applied voltage *V*. Using ImageJ software (National Institute of Health), the intensity of a single cell with the live (green emission) or dead (red emission) stain is obtained. At *V* = 40V, the green/red intensity ratio is 6.08, indicating dominance of the emission of the live stain cells excited by the blue laser. At *V* between 120V and 150V, a green/red ratio drop (alternatively, a red/green ratio increase) is observed in response to the switching of the excitation color. At *V* = 165V, the green/red ratio is 0.26, which shows most dead stain cells are excited by the green laser excitation. At *V* = 175V, the green/red ratio slightly increases because of the bleedthrough, where both the live/dead stains are excited by the green laser due to the overlap of their excitation spectra in the wavelength band. With this voltage-controlled wavelength tuning method, we can adjust the wavelength of an excitation light source *in situ* during detection of multi-color fluorescent labels.

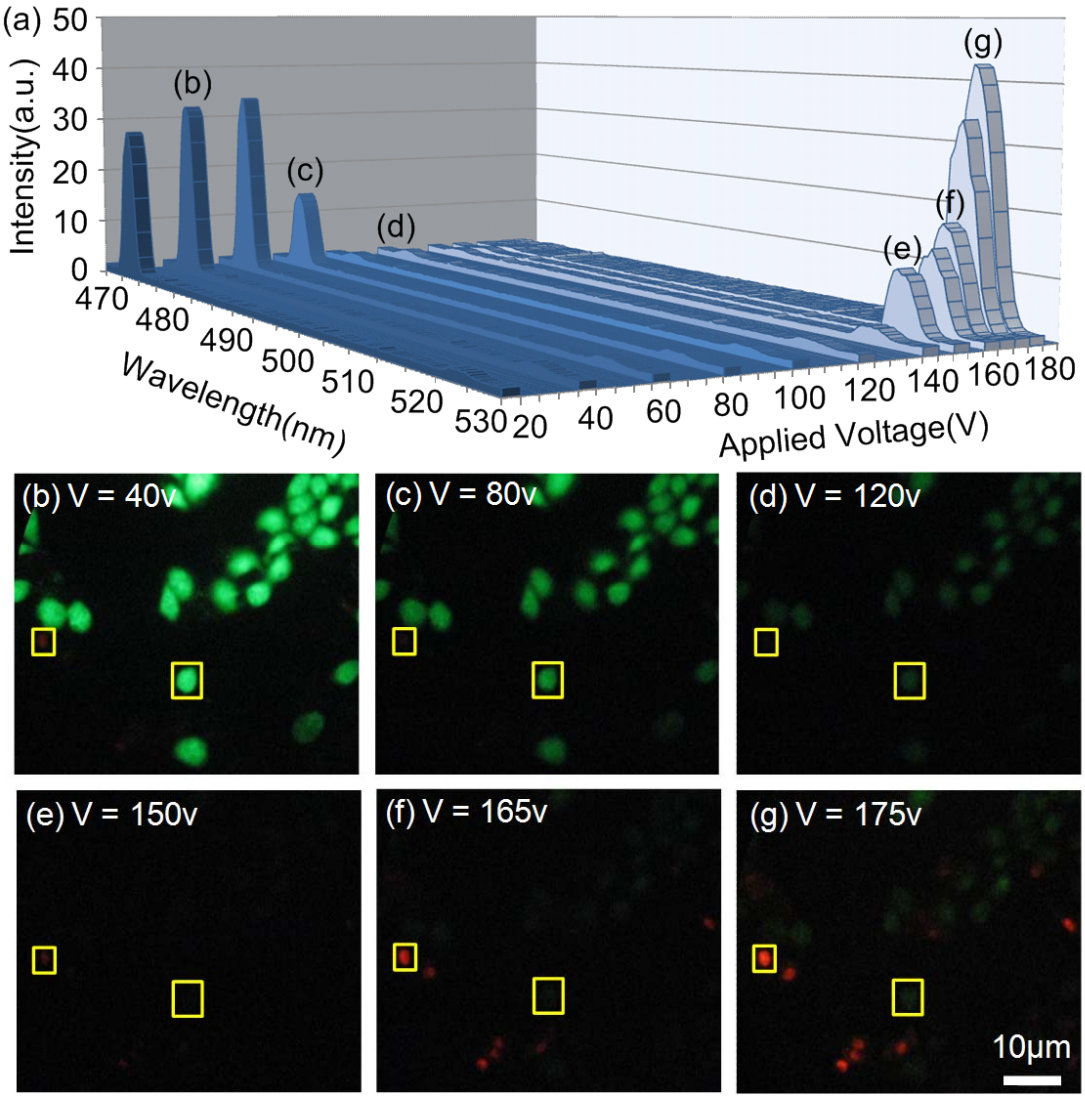

Figure E-4 Results for two-color live/dead PC3 cell imaging. (a) Excitation spectrum as a function of the actuation voltage applied to the GOTF device. (b)-(g) Sequence of images corresponding to the excitation spectrum in (a).

Another two color fluorescent image experiment performed by GOTF was a mixed population of green and red fluorescent protein (GFP/RFP)-expressing PC-3 prostate cancer cells. Here, PC-3 cells maintained in complete media consisting of RPMI-1640 (61870, Gibco) supplemented with 10% (v/v) fetal bovine serum (FBS, 10082, Gibco), and 1% (v/v) antibiotic-antimycotic (15240, Invitrogen). Figure E-5a-f constitute an image sequence of cell mixture excited at different intensity ratios of two laser

wavelengths (473nm and 532nm) controlled by the actuation voltage. Using ImageJ software, the GFP/RFP emission intensity ratio was obtained for a single cell, as shown in Figure E-5g. At the actuation voltage V= 30V, the green/red ratio is 1.77. As the actuation voltage increases from 60 to 120V, the green/red ratio drops (alternatively, a red/green ratio increases). It represents the device's ability to continuously tune the excitation light color ratio. At V = 150V, the red/green ratio is 16.45, which shows that most of the RFP-expressing cells are excited by green laser. The lower green/red intensity ratio at V = 30V is attributed to the broader excitation band of RFP at the shorter wavelength region. The 473nm laser still partially excites the RFP-expressing cells. Figure E-5h shows the excitation and emission spectra of GFP and RFP. Our imaging system is limited by the CCD camera's speed of 30Hz. Therefore, although the device can be actuated at >1kHz, it was operated at a low actuation frequency (~1Hz) during the imaging of the fluorescently labeled cells in this study. For fast multispectral cell image capture, we can replace current camera to a high-speed CCD camera or a multiple-anode photomultiplier tube (PMT).

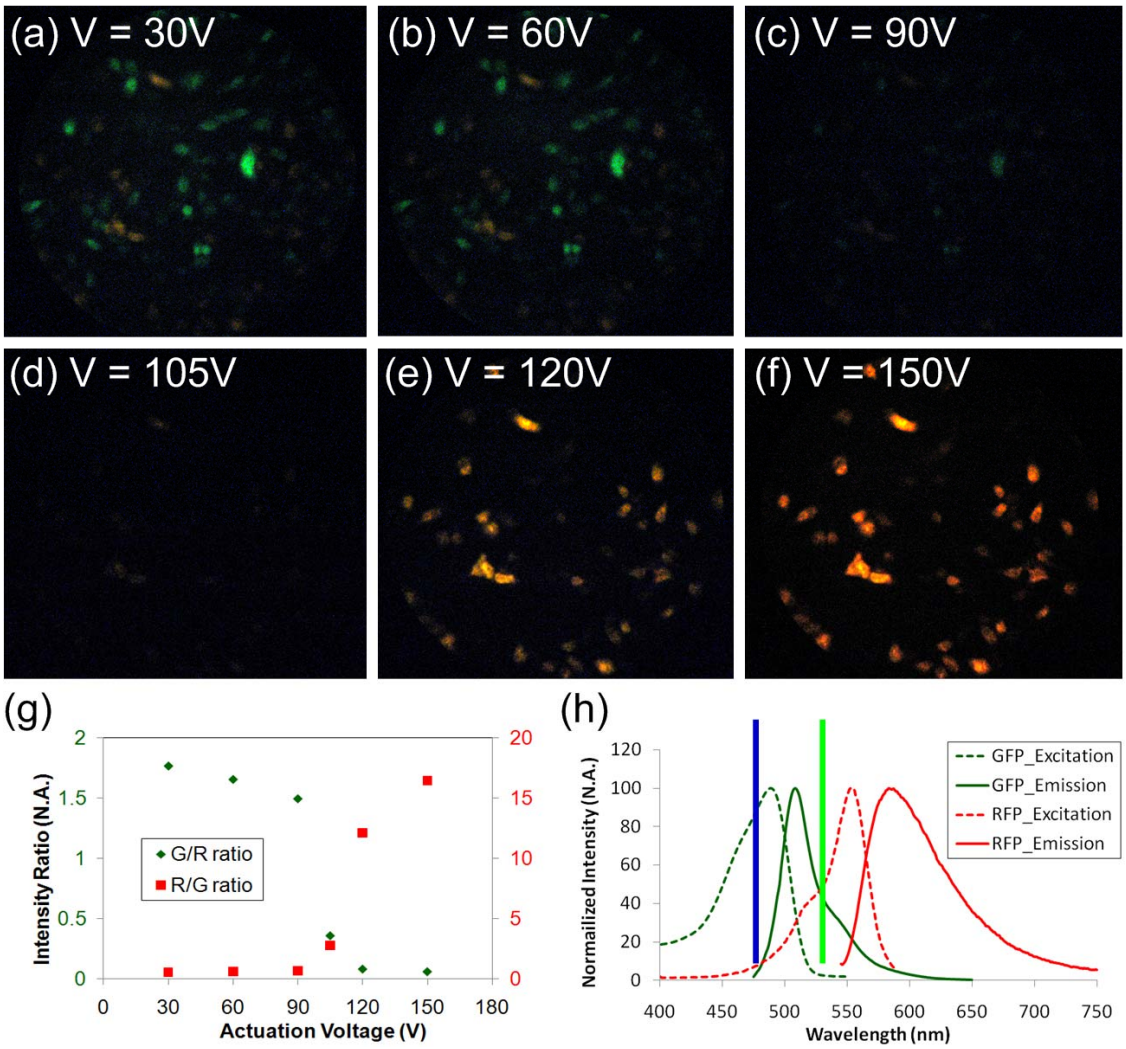

Figure E-5 Tunable photoexcitation of mixed population of GFP/RFP-expressing PC-3 prostate cancer cells our MEMS grating optical filter device. (a)-(f) Sequential images of two-color emissions at increasing voltage (g) Fluorescent intensity ratio as a function of the actuation voltage applied to the grating device. (h) Excitation and emission spectra of GFP and RFP. The blue (green) line represents the 473nm (532nm) laser spectral peak.

E.4 Summary

In summary, we have demonstrated two-color laser wavelength tuning by an optical filtering device incorporating a pitch-variable elastic grating integrated on a silicon chip. This grating device can achieve wavelength tuning to alternate fiber-guided laser

wavelength between λ = 473 and 532 nm at 1 kHz dynamic bandwidth. Our work integrates this device and the lasers into a fluorescent microscope to modulate the two-color emission intensity ratio of an image of live/dead stained and GFP/RFP expressing PC3 prostate cancer cells by a factor of 30 with the device's grating pitch varied by 18%. Like other conventional tunable optical filter devices, this device may also find its utility in alternating laser excitation (ALEX) or spectroscopy for capturing dynamic biological interactions [142, 143]. Using lithography-based batch fabrication, we can construct 16 GOTF device arrays in a 2 × 2 cm^2 die area. Coupled with multiple optical fiber channels, the device arrays could enable massively parallel ALEX and spectroscopic measurements for lab-on-a-chip systems.

References

[1] J. Lamb*, et al.*, "The connectivity map: Using gene-expression signatures to connect small molecules, genes, and disease," *Science,* vol. 313, pp. 1929-1935, Sep 2006.

[2] L. A. Loeb, "Human cancers express mutator phenotypes: origin, consequences and targeting," *Nat Rev Cancer,* vol. 11, pp. 450-457, Jun 2011.

[3] A. S. Rodrigues*, et al.*, "Genomics and Cancer Drug Resistance," *Current Pharmaceutical Biotechnology,* vol. 13, pp. 651-673, Apr 2012.

[4] M. Martinez-Rivera and Z. H. Siddik, "Resistance and gain-of-resistance phenotypes in cancers harboring wild-type p53," *Biochemical Pharmacology,* vol. 83, pp. 1049-1062, Apr 2012.

[5] A. K. Abbas*, et al.*, "Functional diversity of helper T lymphocytes," *Nature,* vol. 383, pp. 787-793, Oct 1996.

[6] K. C. Wood and D. N. Granger, "Sickle cell disease: Role of reactive oxygen and nitrogen metabolites," *Clinical and Experimental Pharmacology and Physiology,* vol. 34, pp. 926-932, Sep 2007.

[7] F. Patella and G. Rainaldi, "MicroRNAs mediate metabolic stresses and angiogenesis," *Cellular and Molecular Life Sciences,* vol. 69, pp. 1049-1065, Apr 2012.

[8] H. Clevers, "Stem cells, asymmetric division and cancer," *Nat Genetics,* vol. 37, pp. 1027-1028, Oct 2005.

[9] P. L. Gourley, "Biocavity laser for high-spped cell and tumor biology," *Journal of Physics D: Applied Physics,* vol. 36, pp. 228-239, 2003.

[10] X. J. Liang*, et al.*, "Determining refractive index of single living cell using an integrated microchip," *Sensors and Actuators A,* vol. 133, pp. 349-354, 2007.

[11] B. R. Bochner, "New technologies to assess genotype-phenotype relationships," *Nat Rev Genetics,* vol. 4, pp. 309-314, Apr 2003.

[12] E. T. Dermitzakis, "Cellular genomics for complex traits," *Nat Rev Genetics,* vol. 13, pp. 215-220, Mar 2012.

[13] D. Psaltis*, et al.*, "Developing optofluidic technology through the fusion of microfluidics and optics," *Nature,* vol. 442, pp. 381-386, 2006.

[14] H. Schmidt and A. R. Hawkins, "The photonic integration of non-solid media using optofluidics," *Nat Photonics,* vol. 5, pp. 598-604, 2011.

[15] F. B. Myers and L. P. Lee, "Innovations in optical microfluidic technologies for point-of-care diagnostics," *Lab Chip,* vol. 8, pp. 2015-2031, 2008.

[16] X. D. Fan and I. M. White, "Optofluidic microsystems for chemical and biological analysis," *Nat Photonics,* vol. 5, pp. 591-597, Oct 2011.

[17] Y. C. Tung*, et al.*, "Optofluidic detection for cellular phenotyping," *Lab Chip,* vol. 12, pp. 3552-65, 2012.

[18] M.-A. Mycek and B. W. Pogue, *Handbook of Biomedical Fluorescence*. New York: Marcel Dekker, Inc, 2003.

[19] B. M. Sauer*, et al.*, "Handbook of Fluorescence Spectroscopy and Imaging: From Ensemble to Single Molecules," ed. Weinheim: Wiley-VCH, 2011.

[20] A. Piruska, *et al.*, "The autofluorescence of plastic materials and chips measured under laser irradiation," *Lab Chip,* vol. 5, pp. 1348-54, 2005.
[21] J. Lippincott-Schwartz and G. H. Patterson, "Development and Use of Fluorescent Protein Markers in Living Cells," *Science,* vol. 300, pp. 87-91, 2003.
[22] B. Zhu, *et al.*, "Engineering a subcellular targetable, red-emitting, and ratiometric fluorescent probe for Ca2+ and its bioimaging applications," *Anal Bioanal Chem,* vol. 397, pp. 1245-50, Jun 2010.
[23] R. A. Seder, *et al.*, "T-cell quality in memory and protection: implications for vaccine design," *Nat Rev Immunol,* vol. 8, pp. 247-58, Apr 2008.
[24] J. S. Boomer, *et al.*, "Immunosuppression in patients who die of sepsis and multiple organ failure," *JAMA,* vol. 306, pp. 2594-605, Dec 21 2011.
[25] I. K. Dimov, *et al.*, "Integrated microfluidic array plate (iMAP) for cellular and molecular analysis," *Lab Chip,* vol. 11, pp. 2701-10, Aug 21 2011.
[26] J. Shen, *et al.*, "An integrated chip for immunofluorescence and its application to analyze lysosomal storage disorders," *Lab Chip,* vol. 12, pp. 317-24, Jan 21 2012.
[27] S. Balslev, *et al.*, "Lab-on-a-chip with integrated optical transducers," *Lab Chip,* vol. 6, pp. 213-7, 2006.
[28] Y.-C. Tung, *et al.*, "PDMS-based opto-fluidic micro flow cytometer with two-color, multi-angle fluorescence detection capability using PIN photodiodes," *Sensors and Actuators B: Chemical,* vol. 98, pp. 356-367, 2004.
[29] J. Seo and L. P. Lee, "Disposable integrated microfluidics with self-aligned planar microlenses," *Sensors and Actuators B: Chemical,* vol. 99, pp. 615-622, 2004.
[30] J. A. Chediak, *et al.*, "Heterogeneous integration of CdS filters with GaN LEDs for fluorescence detection microsystems," *Sensors and Actuators A: Physical,* vol. 111, pp. 1-7, 2004.
[31] O. Schmidt, *et al.*, "Fluorescence spectrometer-on-a-fluidic-chip," *Lab Chip,* vol. 7, pp. 626-9, 2007.
[32] S. Perfetto, *et al.*, "Seventeen-colour flow cytometry: unravelling the immune system," *Nat Rev Immunol,* vol. 4, pp. 648-654, 2004.
[33] T. C. George, *et al.*, "Quantitative measurement of nuclear translocation events using similarity analysis of multispectral cellular images obtained in flow," *Journal of Immunological Methods,* vol. 311, pp. 117-129, 2006.
[34] K. M. Obrien, *et al.*, "ASTRAL, a hyperspectral imaging DNA sequencer," *Review of Scientific Instruments,* vol. 69, pp. 2141-2146, 1998.
[35] J. A. Timlin, "Scanning Microarrays: Current Methods and Future Directions," in *Methods in Enzymology*. vol. Volume 411, K. Alan and O. Brian, Eds., ed: Academic Press, 2006, pp. 79-98.
[36] N. F. Neumann and F. Galvez, "DNA microarrays and toxicogenomics: applications for ecotoxicology?," *Biotechnology Advances,* vol. 20, pp. 391-419, 2002.
[37] Y. Hiraoka, *et al.*, "Multispectral Imaging Fluorescence Microscopy for Living Cells," *Cell Structure and Function,* vol. 27, pp. 367-374, 2002.
[38] L. A. S. John P. Nolan, "Suspension array technology: evolution of the flat-array paradigm " *Trends in Biotechnology,* vol. 20, pp. 9-12, 2002.
[39] D. T. Dicker, *et al.*, "Hyperspectral Image Analysis of Live Cells in Various Cell Cycle Stages," *Cell Cycle,* vol. 6, pp. 2563-2570, 2007.

[40] R. M. Levenson and J. R. Mansfield, "Multispectral imaging in biology and medicine: Slices of life," *Cytometry, Part A,* vol. 69, p. 748, 2006.
[41] T. Haraguchi*, et al.*, "Spectral imaging fluorescence microscopy," *Genes Cells,* vol. 7, p. 881, 2002.
[42] S. C. De Rosa*, et al.*, "11-color, 13-parameter flow cytometry: Identification of human naive T cells by phenotype, function, and T-cell receptor diversity," *Nat Med,* vol. 7, pp. 245-248, 2001.
[43] Y.-C. Tung and K. Kurabayashi, "Nanoimprinted strain-controlled elastomeric gratings for optical wavelength tuning," *Applied Physics Letters,* vol. 86, pp. 161113-3, 2005.
[44] S. Truxal*, et al.*, "High-speed deformation of soft lithographic nanograting patterns for ultrasensitive optical spectroscopy," *Applied Physics Letters,* vol. 92, p. 051116, 2008.
[45] T. T. Cornell*, et al.*, "Clinical implications and molecular mechanisms of immunoparalysis after cardiopulmonary bypass," *J Thorac Cardiovasc Surg,* vol. 143, pp. 1160-1166 e1, May 2012.
[46] M. Azizia*, et al.*, "Immune Status in Very Preterm Neonates," *Pediatrics,* vol. 129, pp. 967-974, 2012.
[47] N. Lee*, et al.*, "Cytokine Response Patterns in Severe Pandemic 2009 H1N1 and Seasonal Influenza among Hospitalized Adults," *PLoS ONE,* vol. 6, p. e26050, 2011.
[48] M. W. Hall*, et al.*, "Immunoparalysis and nosocomial infection in children with multiple organ dysfunction syndrome," *Intensive Care Med,* vol. 37, pp. 525-32, Mar 2011.
[49] W. J. Frazier and M. W. Hall, "Immunoparalysis and Adverse Outcomes from Critical Illness," *Pediatric Clinics of North America,* vol. 55, pp. 647-668, 2008.
[50] P. M. Myrianthefs*, et al.*, "Immune status evaluation of patients with chronic heart failure," *Cytokine,* vol. 37, pp. 150-4, Feb 2007.
[51] W. Heagy*, et al.*, "Lower levels of whole blood LPS-stimulated cytokine release are associated with poorer clinical outcomes in surgical ICU patients," *Surg Infect,* vol. 4, pp. 171-80, 2003.
[52] K. Kayakabe*, et al.*, "Interleukin-1beta measurement in stimulated whole blood cultures is useful to predict response to anti-TNF therapies in rheumatoid arthritis," *Rheumatology,* vol. 51, pp. 1639-43, 2012.
[53] A. V. Araya*, et al.*, "Ex vivo lipopolysaccharide (LPS)-induced TNF-alpha, IL-1beta, IL-6 and PGE2 secretion in whole blood from Type 1 diabetes mellitus patients with or without aggressive periodontitis," *Eur Cytokine Netw,* vol. 14, pp. 128-33, 2003.
[54] R. S. Hotchkiss and S. Opal, "Immunotherapy for sepsis--a new approach against an ancient foe," *N Engl J Med,* vol. 363, pp. 87-9, Jul 1 2010.
[55] G. R. Bernard*, et al.*, "Efficacy and safety of recombinant human activated protein C for severe sepsis," *N Engl J Med,* vol. 344, pp. 699-709, Mar 8 2001.
[56] J. H. Cox*, et al.*, "Measurement of cytokine release at the single cell level using the ELISPOT assay," *Methods,* vol. 38, pp. 274-82, Apr 2006.

[57] R. E. Guerkov, *et al.*, "Detection of low-frequency antigen-specific IL-10-producing CD4(+) T cells via ELISPOT in PBMC: cognate vs. nonspecific production of the cytokine," *J Immunol Methods,* vol. 279, pp. 111-21, Aug 2003.
[58] J. El-Ali, *et al.*, "Cells on chips," *Nature,* vol. 442, pp. 403-11, Jul 27 2006.
[59] C. Ma, *et al.*, "A clinical microchip for evaluation of single immune cells reveals high functional heterogeneity in phenotypically similar T cells," *Nature medicine,* vol. 17, pp. 738-781, 2011.
[60] J. C. Love, *et al.*, "A microengraving method for rapid selection of single cells producing antigen-specific antibodies," *Nat Biotechnol,* vol. 24, pp. 703-7, Jun 2006.
[61] H. Zhu, *et al.*, "A microdevice for multiplexed detection of T-cell-secreted cytokines," *Lab Chip,* vol. 8, pp. 2197-2205, 2008.
[62] M. Frankowski, *et al.*, "A microflow cytometer exploited for the immunological differentiation of leukocytes," *Cytometry A,* vol. 79, pp. 613-24, Aug 2011.
[63] M. Werner, *et al.*, "Microfluidic array cytometer based on refractive optical tweezers for parallel trapping, imaging and sorting of individual cells," *Lab Chip,* vol. 11, pp. 2432-9, Jul 21 2011.
[64] J. Wang, *et al.*, "Quantitative analysis of protein translocations by microfluidic total internal reflection fluorescence flow cytometry," *Lab Chip,* vol. 10, pp. 2673-9, Oct 21 2010.
[65] T. R. Kau, *et al.*, "Nuclear transport and cancer: from mechanism to intervention," *Nat Rev Cancer,* vol. 4, pp. 106-117, 2004.
[66] J. Davis, *et al.*, "Controlling Protein Compartmentalization to Overcome Disease," *Pharmaceutical Research,* vol. 24, pp. 17-27, 2007.
[67] J. Wang, *et al.*, "Quantitative analysis of protein translocations by microfluidic total internal reflection fluorescence flow cytometry," *Lab Chip,* vol. 10, pp. 2673-2679, 2010.
[68] M. Rosenauer and M. J. Vellekoop, "Characterization of a microflow cytometer with an integrated three-dimensional optofluidic lens system," *Biomicrofluidics,* vol. 4, p. 43005, 2010.
[69] P. Kiesel, *et al.*, "Monitoring CD4 in whole blood with an opto-fluidic detector based on spatially modulated fluorescence emission," *Cytometry A,* vol. 79, pp. 317-24, Apr 2011.
[70] M. Schelb, *et al.*, "Fluorescence excitation on monolithically integrated all-polymer chips," *J Biomed Opt,* vol. 15, p. 041517, 2010.
[71] H. Y. Zhu, *et al.*, "Optofluidic Fluorescent Imaging Cytometry on a Cell Phone," *Analytical Chemistry,* vol. 83, pp. 6641-6647, Sep 2011.
[72] V. Lecault, *et al.*, "High-throughput analysis of single hematopoietic stem cell proliferation in microfluidic cell culture arrays," *Nat Methods,* vol. 8, pp. 581-U93, Jul 2011.
[73] S. S. Lee, *et al.*, "Whole lifespan microscopic observation of budding yeast aging through a microfluidic dissection platform," *Proc. Natl. Acad. Sci. USA* vol. 109, pp. 4916-4920, Mar 2012.
[74] P. Skafte-Pedersen, *et al.*, "A self-contained, programmable microfluidic cell culture system with real-time microscopy access," *Biomedical Microdevices,* vol. 14, pp. 385-399, Apr 2012.

[75] M. C. Park, *et al.*, "High-throughput single-cell quantification using simple microwell-based cell docking and programmable time-course live-cell imaging," *Lab Chip,* vol. 11, pp. 79-86, 2011.
[76] D. Falconnet, *et al.*, "High-throughput tracking of single yeast cells in a microfluidic imaging matrix," *Lab Chip,* vol. 11, pp. 466-473, 2011.
[77] N.-T. Huang, *et al.*, "Multiplexed Spectral Signature Detection for Microfluidic Color-Coded Bioparticle Flow," *Analytical Chemistry,* vol. 82, pp. 9506-9512, 2010.
[78] A. A. Ellington, *et al.*, "Antibody-based protein multiplex platforms: technical and operational challenges," *Clin Chem,* vol. 56, pp. 186-93, 2010.
[79] Y.-C. Tung and K. Kurabayashi, "A single-layer PDMS-on-silicon hybrid microactuator with multi-axis out-of-plane motion capabilities-part II: fabrication and characterization," *J. Microelectromech. Syst.,* vol. 14, pp. 558-566, 2005.
[80] S. C. Truxal, *et al.*, "A Flexible Nanograting Integrated Onto Silicon Micromachines by Soft Lithographic Replica Molding and Assembly," *J. Microelectromech. Syst.,* vol. 17, pp. 393-401, 2008.
[81] K. E. Luker, *et al.*, "Imaging ligand-dependent activation of CXCR7," *Neoplasia,* vol. 11, pp. 1022-35, 2009.
[82] C. Lois, *et al.*, "Germline transmission and tissue-specific expression of transgenes delivered by lentiviral vectors," *Science,* vol. 295, pp. 868-72, 2002.
[83] S. C. Truxal, *et al.*, "Design of a MEMS Tunable Polymer Grating for Single Detector Spectroscopy," *International Journal of Optomechatronics,* vol. 2, pp. 75-87, 2008.
[84] N. C. Shaner, *et al.*, "A guide to choosing fluorescent proteins," *Nat Methods,* vol. 2, pp. 905-9, Dec 2005.
[85] N.-T. Huang, *et al.*, "An integrated microfluidic platform for in situ cellular cytokine secretion immunophenotyping," *Lab Chip,* vol. 12, pp. 4093-4101, 2012.
[86] E. Louis, *et al.*, "Tumour necrosis factor (TNF) gene polymorphism influences TNF-alpha production in lipopolysaccharide (LPS)-stimulated whole blood cell culture in healthy humans," *Clin Exp Immunol,* vol. 113, pp. 401-6, Sep 1998.
[87] W. Shurety, *et al.*, "Localization and post-Golgi trafficking of tumor necrosis factor-alpha in macrophages," *J Interferon Cytokine Res,* vol. 20, pp. 427-38, Apr 2000.
[88] D. Aderka, "The potential biological and clinical significance of the soluble tumor necrosis factor receptors," *Cytokine Growth Factor Rev,* vol. 7, pp. 231-40, Oct 1996.
[89] B. B. Aggarwal and K. Natarajan, "Tumor necrosis factors: developments during the last decade," *Eur Cytokine Netw,* vol. 7, pp. 93-124, Apr-Jun 1996.
[90] C. W. Thurm and J. F. Halsey, "Measurement of Cytokine Production Using Whole Blood," in *Current Protocols in Immunology*, ed: John Wiley & Sons, Inc., 2001.
[91] V. J. Hofman, *et al.*, "Cytopathologic detection of circulating tumor cells using the isolation by size of epithelial tumor cell method: promises and pitfalls," *Am J Clin Pathol,* vol. 135, pp. 146-56, Jan 2011.

[92] G. Vona*, et al.*, "Isolation by size of epithelial tumor cells : a new method for the immunomorphological and molecular characterization of circulatingtumor cells," *Am J Pathol,* vol. 156, pp. 57-63, Jan 2000.
[93] S. Zheng*, et al.*, "3D microfilter device for viable circulating tumor cell (CTC) enrichment from blood," *Biomed Microdevices,* vol. 13, pp. 203-13, Feb 2011.
[94] W. Chen*, et al.*, "Photolithographic surface micromachining of polydimethylsiloxane (PDMS)," *Lab Chip,* vol. 12, pp. 391-5, 2012.
[95] Q. Han*, et al.*, "Multidimensional analysis of the frequencies and rates of cytokine secretion from single cells by quantitative microengraving," *Lab Chip,* vol. 10, pp. 1391-400, Jun 7 2010.
[96] M. Fiala*, et al.*, "Amyloid-beta induces chemokine secretion and monocyte migration across a human blood--brain barrier model," *Mol Med,* vol. 4, pp. 480-9, Jul 1998.
[97] K. P. Leister*, et al.*, "Two High Throughput Screen Assays for Measurement of TNF-alpha in THP-1 Cells," *Curr Chem Genomics,* vol. 5, pp. 21-9, 2011.
[98] M. Nimah*, et al.*, "Contribution of MKP-1 regulation of p38 to endotoxin tolerance," *Shock,* vol. 23, pp. 80-7, Jan 2005.
[99] M. Bielefeld-Sevigny, "AlphaLISA immunoassay platform- the "no-wash" high-throughput alternative to ELISA," *Assay Drug Dev Technol,* vol. 7, pp. 90-2, Feb 2009.
[100] F. Poulsen and K. B. Jensen, "A luminescent oxygen channeling immunoassay for the determination of insulin in human plasma," *J Biomol Screen,* vol. 12, pp. 240-7, Mar 2007.
[101] J. M. Cavaillon and M. Adib-Conquy, "Bench-to-bedside review: endotoxin tolerance as a model of leukocyte reprogramming in sepsis," *Crit Care,* vol. 10, p. 233, 2006.
[102] K. L. Kellar and M. A. Iannone, "Multiplexed microsphere-based flow cytometric assays " *Experimental Hematology,* vol. 30, pp. 1227-1237, 2002.
[103] E. Verpoorte, "Beads and chips: new recipes for analysis " *Lab on a chip,* vol. 3, pp. 60N-68N, 2003.
[104] A. P. Alivisatos, "The use of nanocrystals in biological detection " *Nature Biotechnology,* vol. 22, pp. 47-52, 2004.
[105] K. L. Kellar and K. G. Oliver, "Multiplexed microsphere assays for protein and DNA binding reactions " *Methods in Cell Biology,* vol. 75 pp. 409-429, 2004.
[106] J. H. Zhu B, Zhang X,Chen Y, Liu H, Tan W, "Engineering a subcellular targetable, red-emitting, and ratiometric fluorescent probe for Ca2+ and its bioimaging applications," *Anal Bioanal Chem,* vol. 397, pp. 1245-1250, 2010.
[107] M. Palmgren, "Acridine orange as a probe for measuring pH gradients across membranes: Mechanism and limitations," *Anal Biochem,* vol. 192, pp. 316-321, 1990.
[108] G. E. Krasnowska EK, Parasassi T, "Prodan as a Membrane Surface Fluorescence Probe: Partitioning between Water and Phospholipid Phases," *Biophys. J.,* vol. 74, pp. 1984-1993, 1998.
[109] B. Alberts, *Molecular biology of the cell*. New York: Garland Science, 2008.

[110] C. Ma, *et al.*, "A clinical microchip for evaluation of single immune cells reveals high functional heterogeneity in phenotypically similar T cells," *Nat Med,* vol. 17, pp. 738-43, Jun 2011.
[111] H. Zhu, *et al.*, "A microdevice for multiplexed detection of T-cell-secreted cytokines," *Lab Chip,* vol. 8, pp. 2197-205, Dec 2008.
[112] X. Cheng, *et al.*, "A microfluidic device for practical label-free CD4(+) T cell counting of HIV-infected subjects," *Lab Chip,* vol. 7, pp. 170-8, Feb 2007.
[113] W. N. Vreeland, *et al.*, "Multiplexed, high-throughput genotyping by single-base extension and end-labeled free-solution electrophoresis," *Analytical Chemistry,* vol. 74, pp. 4328-4333, Sep 2002.
[114] S. C. Johnson, *et al.*, "Multiplexed genetic analysis using an expanded genetic alphabet," *Clinical Chemistry,* vol. 50, pp. 2019-2027, Nov 2004.
[115] D. C. Pregibon, *et al.*, "Multifunctional encoded particles for high-throughput biomolecule analysis," *Science,* vol. 315, pp. 1393-1396, Mar 2007.
[116] P. A. Darrah, *et al.*, "Multifunctional TH1 cells define a correlate of vaccine-mediated protection against Leishmania major," *Nat Med,* vol. 13, pp. 843-50, Jul 2007.
[117] G. Pantaleo and R. A. Koup, "Correlates of immune protection in HIV-1 infection: what we know, what we don't know, what we should know," *Nat Med,* vol. 10, pp. 806-10, Aug 2004.
[118] F. R. Blattner, *et al.*, "The complete genome sequence of Escherichia coli K-12," *Science,* vol. 277, pp. 1453-1474, Sep 1997.
[119] M. D. Adams, *et al.*, "The genome sequence of Drosophila melanogaster," *Science,* vol. 287, pp. 2185-2195, Mar 2000.
[120] S. Kaul, *et al.*, "Analysis of the genome sequence of the flowering plant Arabidopsis thaliana," *Nature,* vol. 408, pp. 796-815, Dec 2000.
[121] E. S. Lander, *et al.*, "Initial sequencing and analysis of the human genome," *Nature,* vol. 409, pp. 860-921, Feb 2001.
[122] J. C. Venter, *et al.*, "The sequence of the human genome," *Science,* vol. 291, pp. 1304-+, Feb 2001.
[123] R. J. Taylor, *et al.*, "Dynamic analysis of MAPK signaling using a high-throughput microfluidic single-cell imaging platform," *Proc. Natl. Acad. Sci. USA* vol. 106, pp. 3758-3763, Mar 2009.
[124] X. Heng, *et al.*, "Optofluidic microscopy - a method for implementing a high resolution optical microscope on a chip," *Lab Chip,* vol. 6, pp. 1274-1276, Oct 2006.
[125] X. Q. Cui, *et al.*, "Lensless high-resolution on-chip optofluidic microscopes for Caenorhabditis elegans and cell imaging," *Proc. Natl. Acad. Sci. USA* vol. 105, pp. 10670-10675, Aug 2008.
[126] W. Bishara, *et al.*, "Lensfree Optofluidic Microscopy and Tomography," *Annals of Biomedical Engineering,* vol. 40, pp. 251-262, Feb 2012.
[127] O. Schmidt, *et al.*, "Fluorescence spectrometer-on-a-fluidic-chip," *Lab on a Chip,* vol. 7, pp. 626-629, 2007.
[128] N.-T. Huang, *et al.*, "High-speed tuning of visible laser wavelength using a nanoimprinted grating optical tunable filter," *Applied Physics Letters,* vol. 95, pp. 211106-3, 2009.

[129] A. Banerjee, *et al.*, "Wavelength-division-multiplexed passive optical network (WDM-PON) technologies for broadband access: a review," *J. Opt. Netw.,* vol. 4, pp. 737-758, 2005.
[130] J. A. Alvarez-Chavez, *et al.*, "Wide wavelength-tuning of a double-clad Yb3+-doped fiber laser based on a fiber Bragg grating array," *Laser Physics Letters,* vol. 4, pp. 880-883, 2007.
[131] G. Lammel, *et al.*, "Tunable optical filter of porous silicon as key component for a MEMS spectrometer," *Microelectromechanical Systems, Journal of,* vol. 11, pp. 815-828, 2002.
[132] H. Sato, *et al.*, "Fluorescence Backgroundless Ti: Sapphire Laser Using Acousto-Optical Tunable Filter for Raman Spectroscopic Measurements," *Applied Spectroscopy,* vol. 56, pp. 1303-1307, 2002.
[133] M. L. Gostkowski, *et al.*, "Multiphoton-Excited Serotonin Photochemistry," *Biophysical Journal,* vol. 86, pp. 3223-3229, 2004.
[134] Y. Santoso, *et al.*, "Red light, green light: probing single molecules using alternating-laser excitation," *Biochem Soc Trans,* vol. 36, pp. 738-44, 2008.
[135] J. Ross, *et al.*, "Multicolor Single-Molecule Spectroscopy with Alternating Laser Excitation for the Investigation of Interactions and Dynamics," *The Journal of Physical Chemistry B,* vol. 111, pp. 321-326, 2006.
[136] N. Gat, "Imaging spectroscopy using tunable filters: a review," pp. 50-64, 2000.
[137] H. Sagberg, *et al.*, "Micromechanical gratings for visible and near-infrared spectroscopy," *IEEE Journal of Selected Topics in Quantum Electronics,* vol. 10, pp. 604-613, 2004.
[138] X. Li, *et al.*, "Tunable blazed gratings," *J. Microelectromech. Syst.,* vol. 15, pp. 597-604, 2006.
[139] Y. Wang, *et al.*, "Design and fabrication of freestanding pitch-variable blazed gratings on a silicon-on-insulator wafer," *J. Micromech. Microeng.,* vol. 19, p. 025019, 2009.
[140] Y.-C. Tung and K. Kurabayashi, "A nanoimprinted strain-induced reconfigurable polymer micro-optical grating," in *Micro Electro Mechanical Systems, 2005. MEMS 2005. 18th IEEE International Conference on*, 2005, pp. 243-246.
[141] T. Fukano, *et al.*, "Fast dual-excitation ratiometry with light-emitting diodes and high-speed liquid crystal shutters," *Biochemical and Biophysical Research Communications,* vol. 340, pp. 250-255, 2006.
[142] A. N. Kapanidis, *et al.*, "Fluorescence-aided molecule sorting: Analysis of structure and interactions by alternating-laser excitation of single molecules," *Proc. Natl. Acad. Sci. USA* vol. 101, pp. 8936-8941, 2004.
[143] C. Hesch, *et al.*, "Implementation of alternating excitation schemes in a biochip-reader for quasi-simultaneous multi-color single-molecule detection," *Biosensors & Bioelectronics,* vol. 23, pp. 1891-1895, 2008.